Low Temperature Scanning Probe Microscope for Imaging Nanometer Scale Electronic Devices

A dissertation presented

by

Halvar Joseph Trodahl

to

The Department of Physics

in partial fulfillment of the requirements
for the degree of
Doctor of Philosophy
in the subject of
Physics

Harvard University
Cambridge, Massachusetts

September 2011

©2011 - Halvar Joseph Trodahl

All rights reserved.

Thesis advisor | Author

Robert M. Westervelt | **Halvar Joseph Trodahl**

Low Temperature Scanning Probe Microscope for Imaging Nanometer Scale Electronic Devices

Abstract

Low temperature scanning probe microscopy is a powerful tool for the investigation and manipulation of electrons on the nanometer scale. A capacitively coupled scanning probe microscope tip can be used to study electron motion and charging effects in semiconductor nanostructures at liquid helium temperatures. This technique, known as scanning gate microscopy, provides detailed information on the spatial variation of the underlying electronic properties of these systems.

In this thesis, we present details of the design and construction of the third generation low temperature scanning probe microscope (LT-SPM) built in the Westervelt lab. In addition to standard tip-sample scanning, the implemented design draws on the experiences of the first two generations to incorporate what are assessed to be the most valuable features of each. This design incorporates an extended evacuated cold space for sample and microscope, the ability to apply a 7 T magnetic field to the sample during SPM operation, and a novel low temperature coarse positioning mechanism, all at liquid helium temperatures.

We demonstrate the ability of the LT-SPM to capacitively couple to a nanometer scale patterned gold electrode. Electrostatic force microscopy (EFM) is used to measure forces on the SPM cantilever on the order of 10 nN and rates of change in

capacitive coupling per unit length of 0.1 aF/nm. EFM is used to locate the position of a 200 nm isolated electrode and a 30 nm gap between two electrodes at the same potential.

We propose a method to tune the charge state and polarization of a series double quantum dot in a semiconductor nanowire using the LT-SPM tip as a local, moveable, electrostatic gate. The tip-dot interaction is mediated via capacitive coupling, and can thus be controlled with tip position and voltage. Simulations indicate that the LT-SPM has sufficiently high spatial resolution to independently tune the charge of each dot in these systems.

Contents

Title Page i
Abstract iii
Table of Contents v
List of Figures ix
Acknowledgments xi

1 Introduction 1
1.1 Scanning Probe Microscopy Techniques 2
1.2 Design Specifications of LT-SPM 5
1.3 Outline of Thesis 6

2 Microscope Assembly 8
2.1 Introduction 8
2.2 Overall Construction Considerations 9
2.3 Chip Carrier 11
2.4 Piezotube 13
2.5 Cage Base and Cage 15
2.6 Tip and Cantilever 17
2.7 Head Assembly 20
2.7.1 Head 20
2.7.2 Cold Temperature Coarse Positioning Mechanism 20
2.7.3 Cantilever Chip Carrier 23
2.7.4 Head Assembly and Warm Temperature Alignment 26
2.8 Attachment of Head to Cage 28
2.9 Coarse Positioning Feedthrough Bores 30

3 Liquid Helium Cooled Cryostat 31
3.1 Introduction 31
3.2 Coldplates 33
3.2.1 Helium-4 Coldplate 33
3.2.2 Helium-3 Coldplate 35

3.2.3 Attachment of Microscope to Coldplates 36
3.3 Cryogen Reservoirs and Radiation Shields 36
3.3.1 Helium Reservoir and Radiation Shield 38
3.3.2 Nitrogen Reservoir and Radiation Shield 38
3.3.3 Room Temperature Jacket 39
3.4 Access to the Coldspace 39
3.4.1 Operational Access to the Coldspace 39
3.4.2 Full Physical Access to the Coldspace 40
3.5 Magnet Support 43
3.5.1 Copper Baffles 43
3.5.2 Helium Level Monitoring 43
3.5.3 Magnet Leads 46
3.6 Evaluation of Static Cryostat Heat Leak 46
3.6.1 Conductive Heat Leak 46
3.6.2 Radiative Heat Leak 48
3.6.3 Convective Heat Leak 50
3.6.4 Total Heat Leak and Expected Hold Time 50
3.7 Alternative Sample Insert Use 51

4 Feedthroughs and Connections External to the Cryostat 53
4.1 Introduction 53
4.2 Feedthroughs 54
4.2.1 Rotating Feedthroughs 54
4.2.2 Electrical Feedthroughs 57
4.2.3 Assessment of Heat Leak 59
4.3 Connections External to Cryostat 60
4.3.1 SPM Controller 60
4.3.2 Sample Lead Breakout 60
4.3.3 Cable Connections 61
4.3.4 Vacuum Valves 61
4.3.5 Pressure Sensor 62

5 Demonstration of Function 63
5.1 Introduction 63
5.2 Hold Times 63
5.3 Drift 64
5.3.1 Z Drift 64
5.3.2 XY Drift 65
5.3.3 Additional Tip-Sample Movement 65
5.4 Scanning 65

6 Electrostatic Force Microscopy 67
6.1 Introduction . . . 67
6.2 Theoretical Basis . . . 68
6.3 Experimental . . . 71
6.3.1 Calibration Sample Fabrication . . . 71
6.3.2 Electronics . . . 72
6.3.3 Electrostatic Force Microscopy Scanning Procedure . . . 73
6.4 Results . . . 74
6.4.1 Large Area Scanning . . . 74
6.4.2 Scanning Resolution of Electrode Gap . . . 76
6.4.3 Scanning Resolution of Isolated Electrode . . . 76
6.5 Discussion and Outlook . . . 79

7 Double Quantum Dot Conductance Image Simulations 81
7.1 Introduction . . . 81
7.2 Theoretical Background . . . 82
7.2.1 Coulomb Blockade in Single Quantum Dots . . . 82
7.2.2 Coulomb Blockade in Double Quantum Dots . . . 87
7.3 Details of Simulation . . . 93
7.3.1 Tip to Dot Capacitance . . . 94
7.3.2 Conductance Simulations . . . 95
7.4 Results . . . 97
7.4.1 Charge Stability and Conductance of Uncoupled Dots . . . 97
7.4.2 Charge Stability due to Tip Gating . . . 97
7.4.3 Double Dot Conductance Image Simulations . . . 99
7.5 Discussion and Outlook . . . 101

8 Conclusions 102
8.1 Future Directions . . . 103
8.2 Potential LT-SPM Modifications . . . 104
8.3 Concluding Remarks . . . 105

Bibliography 106

A Sample Chip Carrier Fabrication 113

B Head Assembly and Room Temperature Alignment Procedure 115

C Microscope Installation and Cryostat Evacuation 118
C.1 Mircoscope Insertion . . . 118
C.2 Top Hat Installation . . . 119
C.3 Sample Space Evacuation . . . 120

D Cooling Procedures **121**
D.1 Nitrogen Pre-Cool 121
D.2 Liquid Helium-4 Cooling 122
D.3 Liquid Helium-4 Refilling 123

List of Figures

1.1 Illustration of a scanning probe tip near a quantum point contact . . 2
1.2 Scanning gate image of electron flow through a quantum point contact 3
1.3 Scanning gate images of semiconductor nanowire quantum dot 4

2.1 Microscope construction 9
2.2 Sample chip carrier 11
2.3 Piezotube schematic 12
2.4 Piezotube assembly 14
2.5 Assembled piezotube and cage 16
2.6 Cantilever chip and tip 18
2.7 Cantilever resistance sensing bridge 19
2.8 Assembly of cantilever chip mount to head 21
2.9 Head assembly 22
2.10 Coarse positioning wedge assembly 24
2.11 Coarse positioning head design 25
2.12 Cantilever chip mounting assembly 27
2.13 Microscope head to cage attachment 29
2.14 Microscope cage base feedthrough bores 30

3.1 Sectional illustration of cryostat 32
3.2 Cryostat coldplates 34
3.3 Attachment of microscope to coldplate 37
3.4 Exploded projection of cryostat top hats and collars 41
3.5 Cryostat operation 42
3.6 Illustration of magnet support 45

4.1 Horizontal feedthrough rods 55
4.2 Vertical feedthrough rods 56

5.1 Demonstration of topographic scanning 66

6.1 Schematic of electrostatic force microscopy 68

6.2 SEM of reference electrode pattern 71
6.3 Experimental schematic of sample and applied voltages for EFM . . . 72
6.4 Large area EFM scan of reference electrode pattern 75
6.5 EFM scan of fine electrode features 77
6.6 EFM of isolated electrode 78

7.1 Quantum dot circuit diagram 84
7.2 Schematic of quantum dot electrochemical potential 86
7.3 Double quantum dot circuit diagram 88
7.4 Double quantum dot charge stability diagram 90
7.5 Illustration of electron conduction through a double quantum dot . . 91
7.6 Double quantum dot SPM tip circuit diagram 93
7.7 Double dot electrochemical potential for conductance simulations . . 96
7.8 Double quantum dot SPM conductance image simulation 97
7.9 Coupled double quantum dot minimum energy surface 98
7.10 Coupled double quantum dot SPM conductance image simulation . . 100

Acknowledgments

First and foremost, I would like to thank Bob Westervelt for his guidance and mentorship throughout my PhD. His understanding, encouragement, and support of my professional exploration during graduate school has been an invaluable blessing.

Thank you to Eric Heller and Federico Capasso for their guidance as my committee members throughout my work. I am deeply grateful to Vinny Manoharan for joining my committee in the last few months of my PhD.

Thank you to all my colleagues from the Westervelt lab; my contemporaries, Erin Boyd, Keith Brown, and Alex Nemiroski, for their friendship, support, and guidance; Sagar Bhandari, for his enthusiasm and inspiration; Jesse Berezovski for fruitful discussions, friendship, and perspective; Tom Hunt, Dave Issadore, and Jonathan Aguilar, for their energy and optimism. Additionally, I have a great appreciation for the all too short time that I had to learn from Ania Bleszynski-Jayich, Kathy Aidala, and Parisa Fallahi.

I am deeply indebted to all those who have supported my research over the past six years; the Scientific Instrument Shop team, especially Louis Defeo and Al Chandler; Jim MacArthur in the Electronics Shop; Stan Cotreau in the Physics Machine Shop; the CNS for running the cleanroom, imaging suite, and other facilities.

I would like to acknowledge the Nanoscale Science and Engineering Center at Harvard University for supporting my research through the National Science Foundation grant number PHY-06-4609.

Thank you to the support of all the individuals in the Physics Department and SEAS for your support. Of specific import are Naomi Brave, for her outstanding work keeping the lab and NSEC running smoothly, and the team consisting of Sheila

Ferguson and Bill Walker, who consistently keep an eye out for the well being of graduate students in the Physics Department.

My time in graduate school has been shaped by far more than lab work alone. It is with the deepest gratitude that I thank all those who enabled me to pursue professional development during graduate school; Venky Narayanamurti of SEAS/HKS, for the opportunity to teach *An Introduction to Technology and Society*; Sue Goldie of HSPH, for the opportunity to teach *Global Health Challenges: Complexities of Evidence-Based Policy*, and explore careers outside of the sciences; Ethan Karp, for the opportunity to lead the Harvard Graduate Consulting Club; George Ye and Prashant Raghavan, among others, for their incredible contributions as leaders of the HGCC.

To my closest friends, Adam Pivonka, Dave Kaz, David Woolf, and Ryan McGorty, it has been a pleasure to get to know them as we have worked through graduate school. Their support and friendship has been invaluable since my arrival to the States.

I am forever indebted to my family for the love and support they provide; Margaret and Joe, Martha and Kiran, Nyah and Shivani, Lyn and Dick, Jean and Bob.

My final thanks goes to Rebekah Gowler, whose drive and ambition is second to none. The blossoming of our relationship over the past two years has been an inspiration that drives me to greater heights everyday. Thank you.

Throughout my graduate school experience I have worked with many talented and passionate individuals; thank you all for providing such amazing opportunities for personal growth. I wish you all the best for what lies ahead.

Chapter 1

Introduction

Semiconductor technology has become a ubiquitous aspect of daily life since its introduction in the mid-20th century.[1] The miniaturization of semiconductor electronics, now solidly within the nanometer realm,[2] continues to move forward at an astounding pace. The scientific community's interest in nanoscale semiconductor electronics is two-fold motivated; these systems are ideal candidates for potential device applications in nanoscale computing, spintronics, and quantum information processing,[3, 4, 5, 6, 7] and they provide an ideal playground in which to investigate quantum mechanical phenomena, such as coherence, interference, and the wave properties of electrons.[8, 9, 10, 11]

As the size of devices move further into the nanometer regime, it becomes considerably more difficult to probe their properties; bulk measurements, such as photoluminescence and electronic transport, do not elucidate the spatial variation of device properties on the length scales necessary to understand the subtleties of their behavior. As such, we turn our attention to the use of scanning probe techniques to

investigate nanometer scale spatial variations in the electronic properties of semiconductor devices.

1.1 Scanning Probe Microscopy Techniques

Scanning probe microscope (SPM) techniques were introduced as tools to spatially resolve sample properties on the nanometer scale in 1982 with the invention of the scanning tunneling microscope.[12, 13] Diversification of the technique has led to plethora of scanning probe techniques.[14, 15, 16] One such technique, scanning gate microscopy (SGM), was pioneered in the Westervelt lab in the late 1990s.[17, 18]

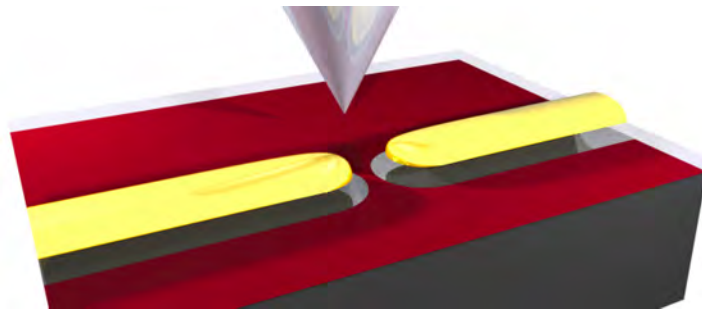

Figure 1.1: Illustration of a scanning probe tip proximal to a quantum point contact in a two-dimensional electron gas (2DEG), depicted as a red sheet. The application of a sufficiently negative voltage to two gold electrostatic gates will deplete the 2DEG below. This forms a quasi-one dimensional constriction in which electronic modes become quantized. A sufficiently negative voltage applied to the tip will deplete the 2DEG in a small region immediately below the tip, which acts as a moveable scatterer in the 2DEG.

SGM utilizes the spatially dependent capacitive coupling of a cooled SPM tip to perturb the electronic energies within a semiconductor nanostructure. Since its introduction, SGM has been used to probe the properties of systems comprising of

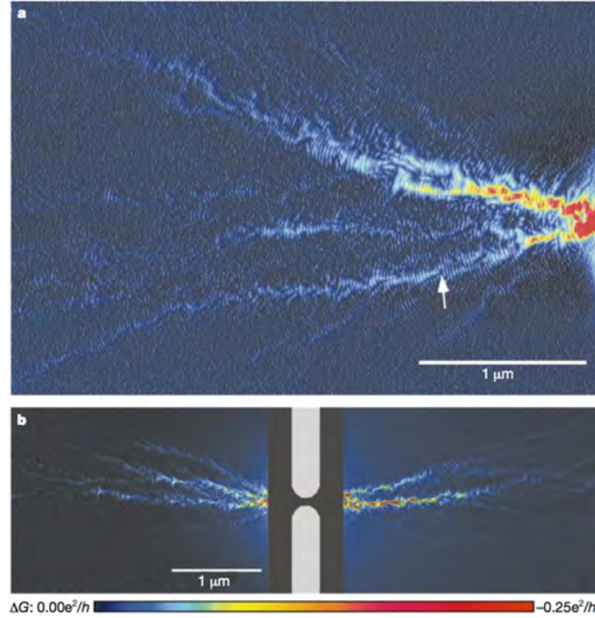

Figure 1.2: Scanning gate microscopy images of electron flow through the lowest energy mode of a quantum point contact showing branched flow at 1.7 K. Fringes spaced at half the Fermi wavelength indicate phase coherence over length of the scan. Image adapted from [18].

two-dimensional electron gases (2DEGs),[17, 18, 19, 20, 21, 22, 23, 24] semiconductor nanowires,[25, 26, 27] carbon nanotubes,[28, 29] and graphene.[30, 31, 32, 33]

In the context of open systems, in which transport is dominated by ballistic electron flow, the SGM acts as a moveable scatterer. Figure 1.2 shows an SGM scan of a 2DEG in which the tip strongly scatters ballistic electrons moving through a quantum point contact (QPC). The signal corresponds to the electron flux through the region directly below the tip position. Branching and bunching of electron paths can be seen as the electrons move away from the QPC.

In closed systems, such as quantum dots, confinement of electrons allows the SGM acts as a local, moveable, electrostatic gate. This can be used to determine the location of a quantum dot within a semiconductor nanowire, as seen in Figure 1.3, or

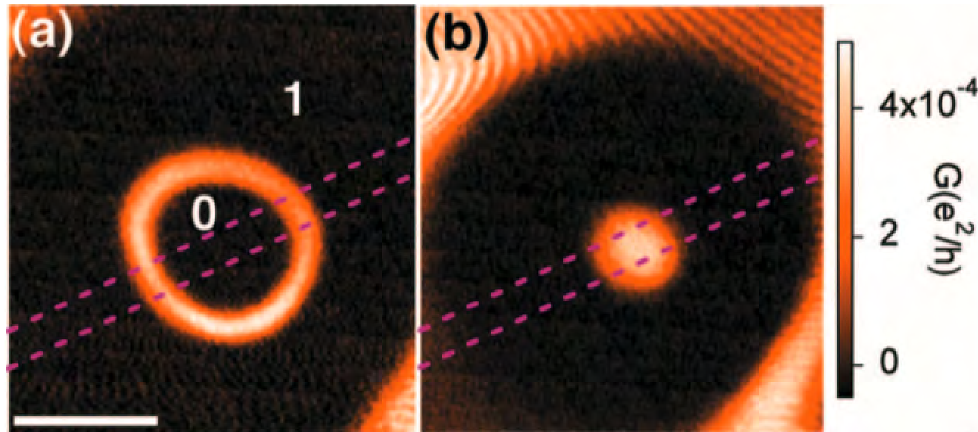

Figure 1.3: Scanning gate microscopy Coulomb-blockade conductance images of the last electron in a quantum dot formed between two InP barriers in an InAs nanowire. The scale bar length is 100 nm and the dotted lines represent the position of the nanowire. Scans are taken at 4.2 K with the tip 100 nm above the dot. Image adapted from [26].

to manipulate the dot's charge state.

The original Westervelt low temperature scanning probe microscope (LT-SPM), built my Mark Topinka and housed in a small IR Labs dewar, proved to be an excellent tool with the ability to cool a sample to 1.7 K in vacuum. Unfortunately, the thermal load and relatively small liquid cryogen reservoirs conspire to afford only a short, 8 hour, cryogen hold time. Although this is nominally enough to perform scanning probe measurements, extended sample investigation is inconvenient at best.

The second revision of the microscope, built by Kathy Aidala, began full operation in 2004. The SPM, based on the same operating principles as that of Topinka, is housed in a superinsulated liquid helium cryostat that allows the microscope to be inserted into the bore of a 7 T superconducting magnet. Drawbacks to this design include; the sample is held in a medium vacuum (0.3 mbar) environment that has recently led to sustained arcing of high voltage lines in the system; and the restricted

size of the cold space due to its insertion into the magnet bore.

1.2 Design Specifications of LT-SPM

Much of the work that I have performed as part of my PhD has related to the design and construction of a new LT-SPM that incorporates the most desirable aspects of the lab's two previous versions discussed above. In addition to these qualities, we wish to include a mechanism for coarse positioning the tip and sample at cold temperature; an aspect initially absent from previous SPM iterations, although retrofitted to the Aidala system. Thus, the list of most desired specifications, aside from high precision scanning and sample detection abilities that are standard on the two previous designs, are as follows;

1. Ensure the cryogen hold time is in excess of 24 hours, allowing the investigation of samples over the course of days or weeks without the likelyhood of unexpected warming of the system.

2. Incorporate a coarse positioning mechanism to move the tip over a region of 200 μm$\times$200 μm with precision of 5 μm while the system is held at liquid helium temperatures.

3. Allow the application of a 7 T magnetic field to the cooled sample.

4. Provide a large, liquid helium-4 cooled coldspace for the sample, microscope, and all associated cold temperature hardware. Excess space is desirable to allow for modifications or additions to the system.

5. Include a helium-3 cooling mechanism to decrease the temperature of the SPM to 500 mK or below.

1.3 Outline of Thesis

This thesis describes the design and functionality of the LT-SPM built for the investigation of semiconductor nanoscale electronic devices.

Chapter 2 discusses the design of the microscope itself. The discussion moves from the smallest aspects of the microscope, the sample and SPM tip, to its larger components, including the mechanisms that allow microscopic and macroscopic tip-sample movement. Of particular interest is the implementation of low temperature coarse positioning, as mentioned in the specifications outlined in Section 1.2.

Chapter 3 transitions to the design of the cryostat that houses and cools the SPM. The custom built cryostat is based around a set of liquid cryogen cooled coldplates that allow cooling of the SPM to cryogenic temperatures while in vacuum. We estimate the heat load due to radiative, conductive, and convective heat transfer and approximate cryogen consumption rates and hold times for the LT-SPM system.

In Chapter 4, the discussion moves to the implementation of mechanical and electrical feedthroughs into the coldspace. These allow for the manipulation of the microscope at cold temperature, but have the adverse effect of introducing additional thermal load on the coldspace. We discuss thermal isolation of the sample and estimate the heat leak due to these feedthroughs.

Chapter 5 highlights the operation of the LT-SPM in terms of cryogen hold times, scanning ranges at room and cryogenic temperatures, and topographic sensitivity of

the system.

Chapter 6 presents a demonstration of electrostatic force microscopy (EFM), an imaging technique based on the capacitive coupling between tip and sample. The opening discussion covers the theoretical basis of the technique and experimental details. We present results of EFM used to image a patterned reference electrode at room and liquid helium temperatures, from which we estimate the resolution of this technique in the LT-SPM.

Chapter 7 presents simulations that confirm the viability of the LT-SPM to image multiple quantum dot systems at low temperature using scanning gate microscopy (SGM). We calculate the conductance through a semiconductor nanowire double quantum dot in the presence of a conducting tip as a function of tip position. These simulations show the ability of SGM to determine the charge state and polarization of these nanoscale devices.

Chapter 8 contains concluding remarks, future experimental directions, and possible modifications to the LT-SPM.

Chapter 2

Microscope Assembly

2.1 Introduction

In this chapter we will discuss the design of the low temperature scanning probe microscope (LT-SPM) that I designed while in the Westervelt Lab. A partially sectioned illustration of the microscope is shown in Figure 2.1. The sample sits atop the piezotube assembly and, during scanning, is translated with respect to the tip, which is held fixed within the head assembly.

The chapter begins with a brief discussion of overarching microscope construction considerations. In Section 2.3 we discuss the specifications and fabrication of the sample carrier, onto which samples are mounted for measurement. Section 2.4 discusses the characteristics of the piezotube and associated assembly. Section 2.5 concerns the cage base and cage. Section 2.6 pertains to the tip and cantilever currently in use in the system. In Section 2.7 we discuss the design considerations of the head, including its components (Section 2.7.1), the incorporation of cold temperature

coarse positioning (Section 2.7.2), the mounting of the cantilever chip (Section 2.7.3), and warm temperature sample alignment (Section 2.7.4). We outline the attachment of the head to the cage in Section 2.8. The chapter concludes with a brief discussion of considerations regarding mechanical feedthroughs to the head in Section 2.9.

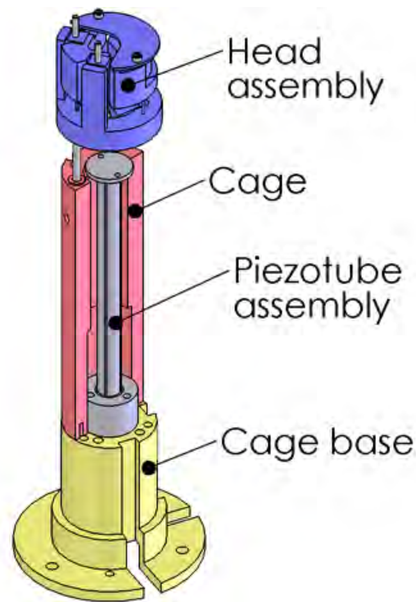

Figure 2.1: Isometric projection highlighting the major components of the microscope.

2.2 Overall Construction Considerations

The operation of the microscope in vacuum and at low temperature require a number of considerations to be at the forefront of a one's mind during design and construction of the system. We highlight a number of these considerations below.

Material Choice

In order to reduce isotropic thermal contraction while maintaining high thermal conductivity at low temperature, brass is used as the primary construction material

of the microscope. Where high thermal conductivity is especially important, such as feedthrough coldsinking, oxygen-free high-conductivity (OFHC) copper is used. Materials of each part are discussed along with their design throughout the remainder of this chapter.

Screw Joints

Thermal and mechanical anchoring between microscope parts is most commonly achieved through the use of screw joints. As the screw compresses two or more parts together, its material must be chosen to match the thermal contraction of the parts it joins. Most commonly found in this microscope are brass screws joining brass parts.

Trapped Gas

The slow release of trapped gas between assembled parts, most commonly in blind screw holes, has the potential to undermine the vacuum of the microscope. Great care is taken to incorporate venting holes throughout the design to remove potential pockets of trapped gas.

Gold Plating

The formation of a patina on brass and copper parts increases thermal impedance through surface joints. These parts are gold plated prior to assembly to inhibit patina formation. Bright Electroless Gold, manufactured by Transene Company of Danvers, MA, has proved to be a simple and effective way to gold plate these parts.

2.3 Chip Carrier

The chip carrier is a 14 mm diameter circular printed circuit board (PCB) onto which we attach our sample. Figure 2.2(a) shows a typical chip carrier with twelve of its fifteen bond pads wired for electrical contacting of a sample. The chip carrier is 1.5 mm thick, although the sample mounting area is usually milled out to be approximately 1 mm below the surface of the bond pads. Two 0-80 through holes on either side of the carrier secure it to the microscope. The blue shaded area in Figure 2.2(a) denotes the region in which the tip can be aligned over the sample, and hence where a sample should be mounted. Figure 2.2(b) shows a photo of the as delivered PCB. Appendix A outlines the fabrication of chip carriers.

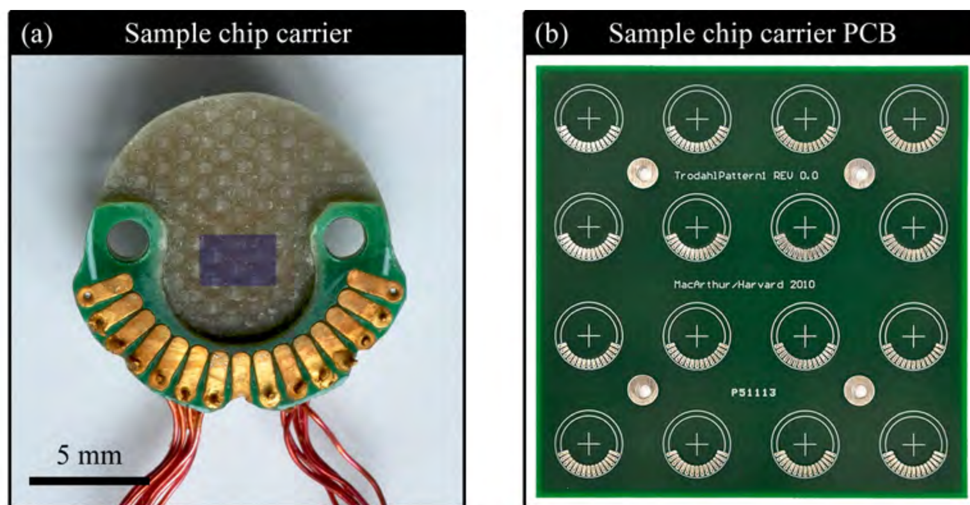

Figure 2.2: (a) Photo of a milled, soldered, and gold plated chip carrier. Two 0-80 through holes allow attachment of the chip carrier to the microscope. The blue area denotes the area over which the cantilever and tip can be aligned. (b) Photo of chip carrier printed circuit board containing 16 chip carriers and measuring 4” by 4”.

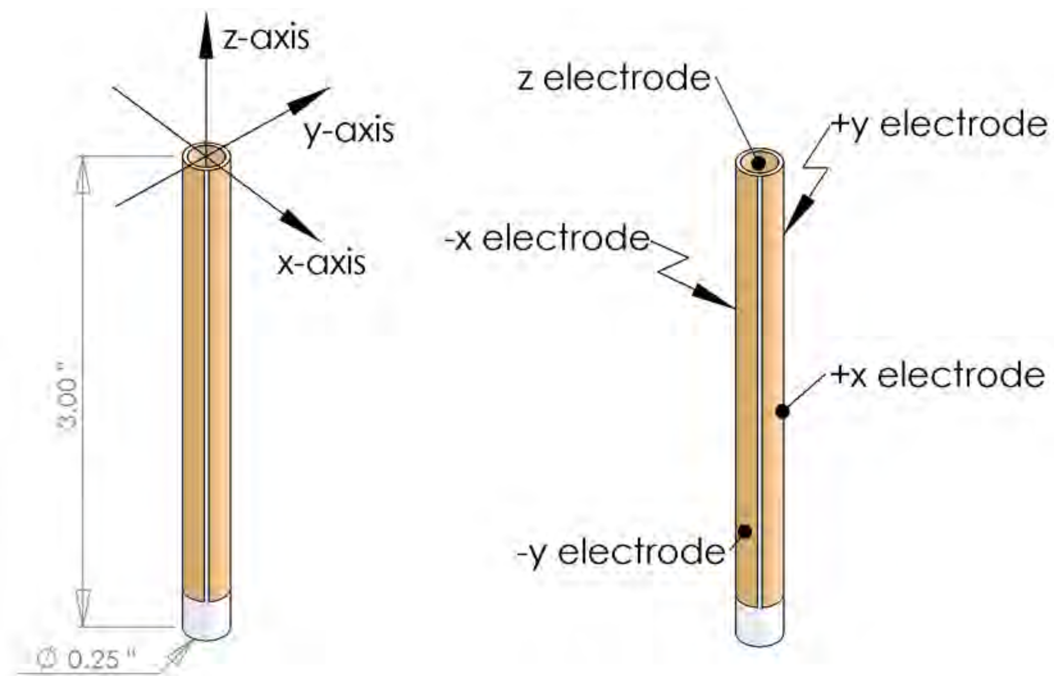

Figure 2.3: (left) Schematic of piezotube, piezotube electrodes, and system of axes. (right) The four electrodes on the outside of the piezotube are used for motion in the x and y directions, the centre electrode for motion in the z direction.

2.4 Piezotube

The operation of the microscope relies on the ability to move the tip with respect to the sample. This is achieved by mounting the sample on a piezoelectric ceramic tube that can be translated with the application of appropriate voltages. The tubes currently in use are custom ordered from EBL Products of East Hartford, CT. They are 3" long, 0.25" in diameter, 0.02" thick, and made of PZT. CAD renders of the tube are shown in Figure 2.3. Four external electrodes contact the quadrants of the piezotube. These run the length of the tube except for 0.3" at one end. An electrode on the interior runs the entire length of the tube runs.

Movement of the piezotube in the xy plane is achieved by applying equal and opposite voltages to opposing electrodes. To move the piezotube in the $+x$ direction, a negative voltage must be applied to the $+x$ electrode and a positive voltage to the $-x$ electrode. Applying voltages of ± 200 V results in movement of approximately 10 μm at 4 K and 30 μm at room temperature. Elongation (contraction) of the piezotube in the z direction is achieved by applying a positive (negative) voltage to the inner z electrode. Applied voltages of ± 200 V result in changes in length of approximately 1 μm at 4 K and 3 μm at room temperature. It should be noted that these scanning ranges vary by tube and should be calibrated during operation.

To allow for mounting of the chip carrier to the piezotube, and mounting of the piezotube to the cage base, the four part piezotube assembly is epoxied together as shown in Figure 2.4. The epoxy used is Stycast 1266, a staple of low temperature experimentalists, manufactured by Emerson & Cuming. The piezotube is directly connected to only two pieces, both of which are Macor ceramic glass, an electrical

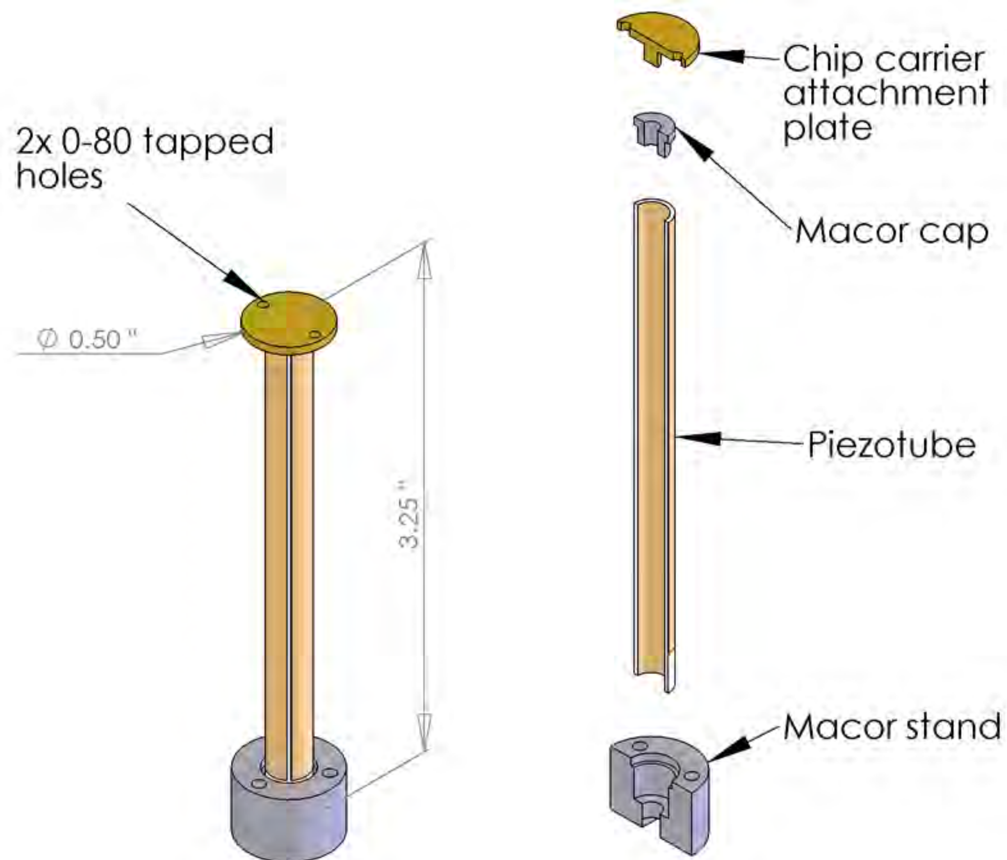

Figure 2.4: (left) Isometric projection of the piezotube assembly. Two 0-80 tapped holes in the brass chip carrier attachment plate allow for mounting of the chip carrier to the piezotube assembly. (right) Exploded section of the piezotube assembly. The four pieces are epoxied together prior to attachment to the microscope. Note that the two pieces that directly contact the piezotube are both Macor, an insulating glass ceramic produced by Corning Incorporated, of Corning, NY, to ensure electrical isolation of the piezotube from the rest of the microscope.

insulator, to ensure the piezotube is electrically isolated from the rest of the microscope. A brass chip carrier attachment plate is the fourth part of this assembly, and allows for the mounting of the chip carrier with two 0-80 screws.

Electrical connection to each piezotube electrode is made by a solder connection to AWG 26 wire. It should be noted that the connection to the z electrode must be made prior to epoxying of the piezotube assembly. Full instructions for the assembly of the piezotube assembly can be found in the thesis of Kathy Aidala.[34]

2.5 Cage Base and Cage

The OFHC copper cage base is the common rigid support to which both the sample, via the piezotube, and the tip, via the cage and head, attach. Figure 2.5(a) shows the piezotube assembly mounted on the cage base with three 1-72 screws. The brass cage fits over the piezotube and bolts onto the cage base with three 2-56 $\times$1.5” screws, accessible from the underside of the base. The assembled cage is shown in Figure 2.5(b).

In order to reduce pickup in the sample measurement circuitry, it is necessary to ensure the sample and sample leads are adequately shielded from the piezotube driving voltages. To reduce pickup at the sample end of the piezotube, a small copper shim, grounded to the cage, is placed between the chip carrier and its attachment plate. At the base of the cage, a tin plated copper sheath is placed around the piezotube driving leads. The copper shim (screwed onto the chip carrier attachment plate) and the piezo lead sheath can be seen in Figure 2.5(b).

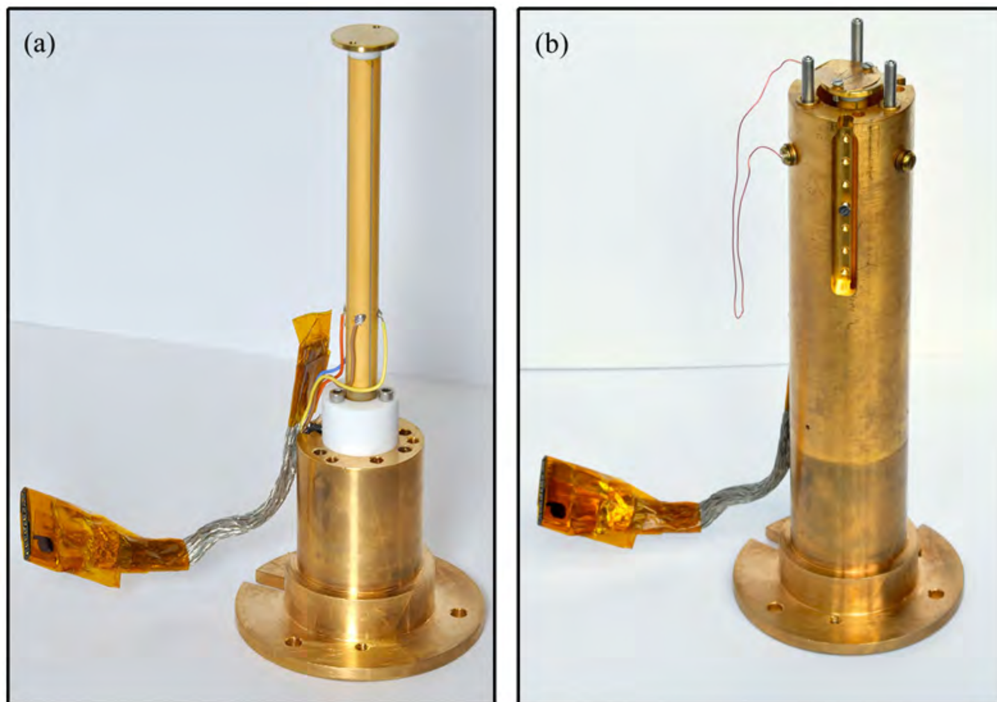

Figure 2.5: (a) Photo of epoxied piezotube assembly mounted on the cage base. (b) Cage base and piezotube with cage attached. A copper grounding shim and its connection to the cage can be seen attached to the sample chip attachment plate.

2.6 Tip and Cantilever

Laser detection of cantilever deflection, as is typical in most atomic force microscopy (AFM) techniques, has the potential to adversely affect the conduction properties of photosensitive semiconductor samples at low temperature. Due to this, piezoresistive cantilevers are used in this SPM to avoid interaction of cantilever deflection measurement with the sample.

The cantilevers currently used in this experimental setup are DFM PRC120 produced by KLA Tencor. A photo of a representative cantilever chip is shown in Figure 2.6(a). These cantilevers are 125 μm in length, and have a spring constant of 40 N/m. The tip on each cantilever is approximately 5 μm in height, and is nominally 20nm in radius. The resistance over the cantilever is typically in the 600-700 Ω range. We measure changes of resistance with cantilever deflection measured at the tip to be 0.02 Ω/nm. The cantilevers have a resonant frequency of 250-300 kHz and quality factor 350-500, although the current setup does not mechanically oscillate the cantilever.

In addition to the piezoresistive cantilever, the chip contains a balance resistor made to the same specifications as the piezoresistive section of the cantilever. Figure 2.6(b) shows a scanning electron micrograph of the cantilever and on-chip balance resistor. Four gold pads provide electrical connections to the cantilever and balance resistor leads. Experience has proven that these connections break when cooled to liquid nitrogen temperature. To ensure electrical connection at cold temperature, we wirebond each gold pad to its respective cantilever or balance lead prior to cooling.

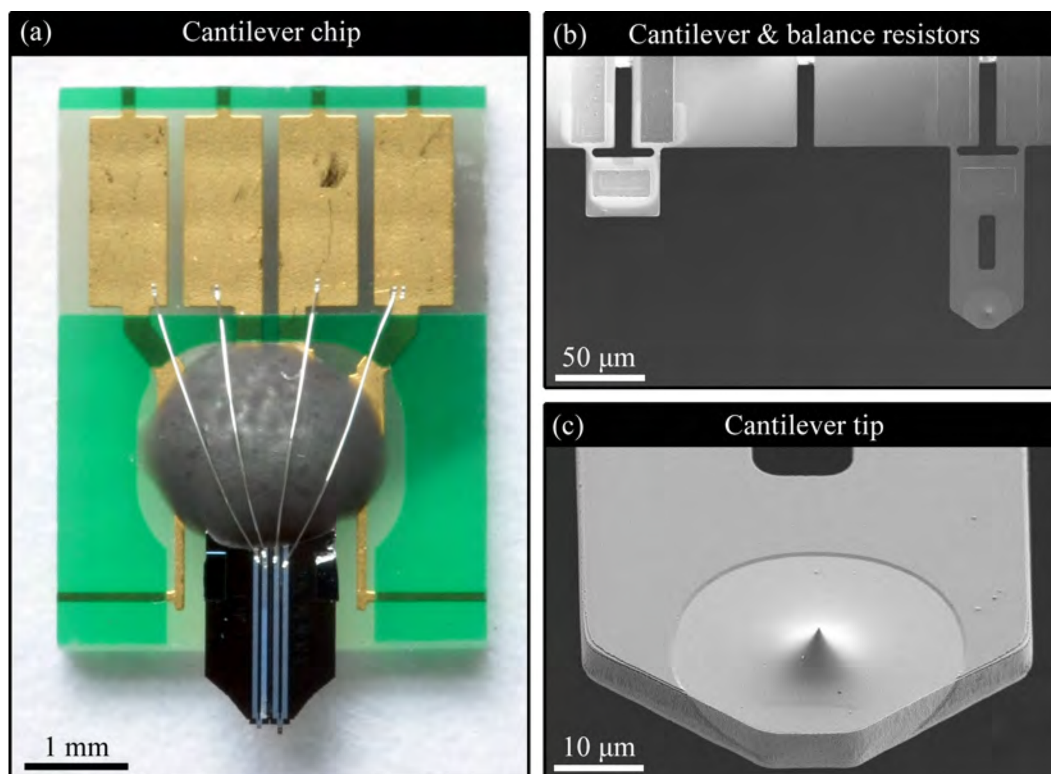

Figure 2.6: (a) Photo of cantilever chip. The cantilever can be seen protruding from the silicon chip toward the bottom of the photo. Four gold plated pads at the top of the chip allow for electrical connection to the piezoresistive cantilever and on-chip balance resistor. Wire bonds between each of these bond pads to the four electrodes on the silicon chip ensure an electrical connection at low temperature. (b) Scanning electron micrograph (SEM) of the on-chip balance resistor (left) and piezoresistive cantilever (right). The thin section of material joining the cantilever to the bulk of the chip provides the piezoresistive section used to detect cantilever deflection. (c) SEM of the tip at the end of the cantilever, taken at a 45 degree tilt. The end of the tip has a radius of 20nm and sits approximately 5 μm above the surface of the cantilever.

Figure 2.7: Circuit diagram of the Wheatstone bridge used to detect changes in the deflection of the piezoresistive cantilever. The right arm of this bridge circuit is comprised of the cantilever resistance, R_{cant}, and the on-chip balance resistor, R_{bal}. The left hand arm is made up of two identical balancing resistors, R_{bridge}. With an applied bias voltage, V_{bias}, changes in the measured bridge voltage, V_{bridge}, are indicative of cantilever deflection. The potential with respect to ground of the bridge circuit, and hence the cantilever and tip, can be adjusted changing the voltage V_{tip}.

Detection of the changes in cantilever resistance are measured with a Wheatstone bridge, as depicted in Figure 2.7. In order to maximize the sensitivity of this bridge to the cantilever resistance, R_{cant}, the on-chip balance resistor, R_{bal}, is used as the resistor in series with the cantilever. The two resistors in parallel with the cantilever arm, R_{bridge}, are 650 Ω metal film resistors. The applied bias voltage, V_{bias}, is set between 0.2 V to 1.5 V depending on the sensitivity required. The voltage measured over the probe nodes of the bridge, V_{bridge}, is,

$$V_{bridge} = V_{bias} \left(\frac{1}{2} - \frac{R_{bal}}{(R_{bal} + R_{cant})} \right). \tag{2.1}$$

If a 1.5 V bias is applied to the bridge, a 1 nm tip deflection will result in a change in V_{bridge} of approximately 13 μV. Details of the electronics used for detection

are discussed in the theses of Mark Topinka.[35]

2.7 Head Assembly

The head assembly consists of two major components, the head and the cantilever chip carrier. Figure 2.8(a) shows exploded CAD projections of the head assembly. The head design is adapted from designs previously employed in the Westervelt Lab.[34, 35, 36, 37]

2.7.1 Head

The bulk of the head consists of two brass pieces, known as the lower head and upper head, joined together by three phosphor bronze spring posts. Figure 2.9 shows projections of the exploded and assembled head. Phosphor bronze is chosen as the spring post material as it retains elastic behavior at low temperature. These spring posts are nominally press fit into the upper and lower head, although we have found it necessary to epoxy them in place to ensure stability of the head.

2.7.2 Cold Temperature Coarse Positioning Mechanism

The spring posts provide a semi-rigid support between the upper and lower head, which is the basis of the low temperature coarse positioning system integrated into this design. The spring posts act as rigid supports in the z direction that maintain a constant distance between the upper and lower head. The posts act as strong springs in the xy plane, allowing relative motion between the upper and lower head in the

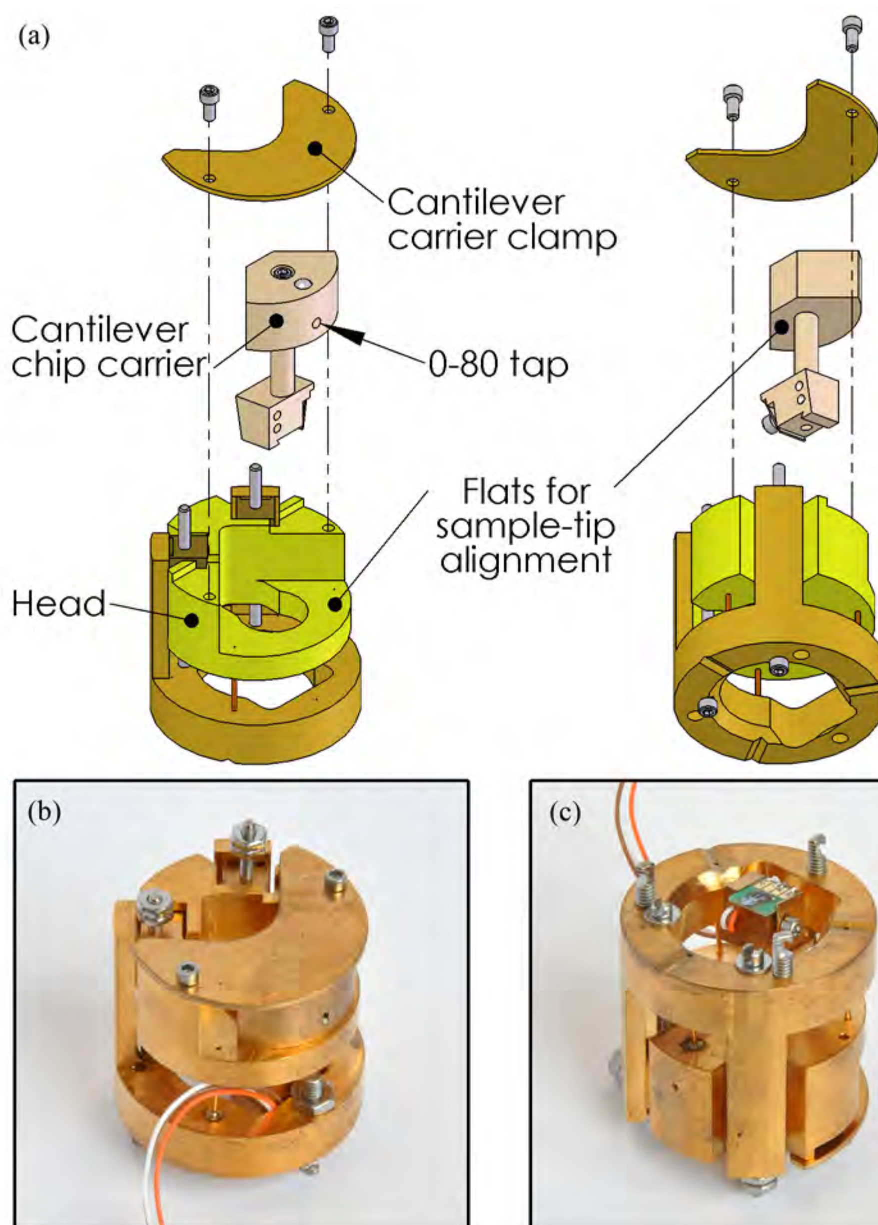

Figure 2.8: (a) Isometric projections of the exploded microscope head and cantilever mounting assembly. Flat surfaces on the upper head and the cantilever mount slider allow for room temperature coarse positioning over an area of approximately 3 mm by 3 mm. An 0-80 screw can be inserted into a tapped hole in the back of the cantilever mount slider and allows for precise positioning of the cantilever with respect to a sample. A brass clamp holds the cantilever mount in place when in the desired position. (b) and (c) Photos of the assembled head and cantilever mount, with cantilever chip attached. Three hooks on the bottom of the head allow for the attachment of the head to the microscope cage with springs.

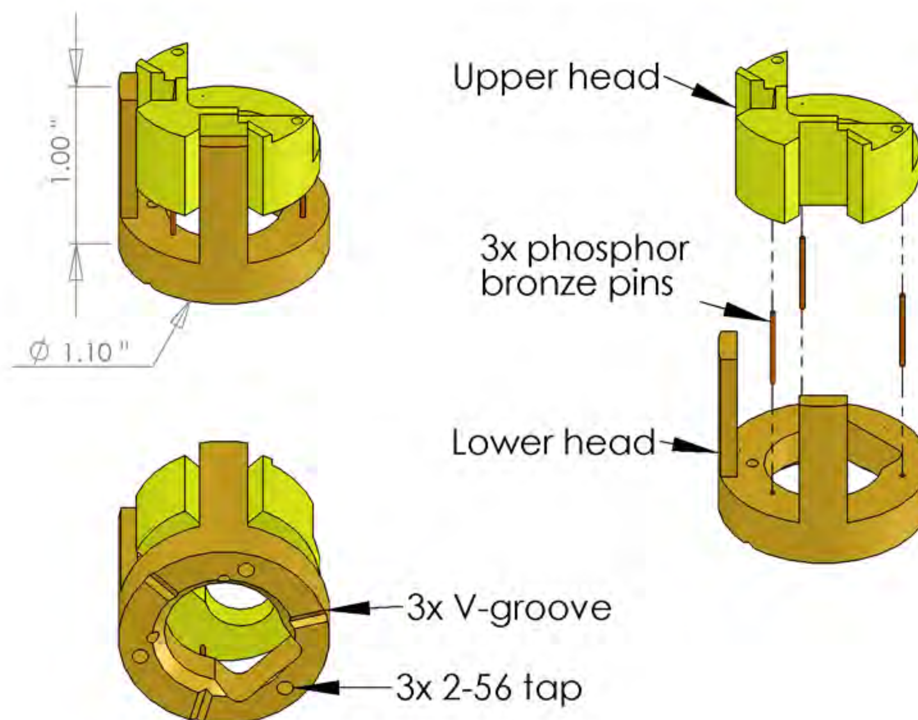

Figure 2.9: Isometric projections of the microscope head. The head is assembled from five parts; the upper and lower head, both made of brass, and three phosphor bronze spring posts. An exploded view (right) shows how the five pieces fit together prior to epoxying the spring posts in place. (lower left) Three V shaped grooves on the bottom face of the lower head ensure its orientation is held constant with respect to the cage and sample. Three 2-56 tapped holes allow for the connection of springs between the head and the cage.

lateral directions. Relative motion is achieved by applying a lateral force between the upper and lower head. When such a force is removed, the spring posts, and hence upper and lower head, return to their neutral position. In practice, this lateral movement is controlled through the use of two small brass wedges attached to the head by two 0-80 screws. The placement and assembly of these wedges into the head are shown in Figure 2.10.

Figure 2.11 shows a sectioned detail of the upper head, lower head, and wedge. A 5° offset between opposing faces of the wedge matches the offset between opposing faces of the upper and lower head. Moving the wedges down their respective 0-80 screws forces the upper head to move relative to the lower head, resulting in coarse positioning orthogonal to the face of the lower head that the wedges slide against. The motion provided by each wedge is at 90° to the other, providing coarse positioning in the xy plane.

We approximate the precision of the coarse positioning mechanism to be 4 μm, using the conservative estimate that it is possible to turn the 0-80 screw by as little as an eighth of a revolution. The unimpeded range of motion of the wedge is 0.5”, allowing for a maximum range of coarse positioning of approximately 1 mm in each direction. Both the range and precision of the coarse positioning have proven to be more than adequate for our anticipated needs.

2.7.3 Cantilever Chip Carrier

The cantilever carrier is a three part brass assembly that provides a mounting stage for the cantilever chip. Figure 2.12 shows an exploded CAD projection and

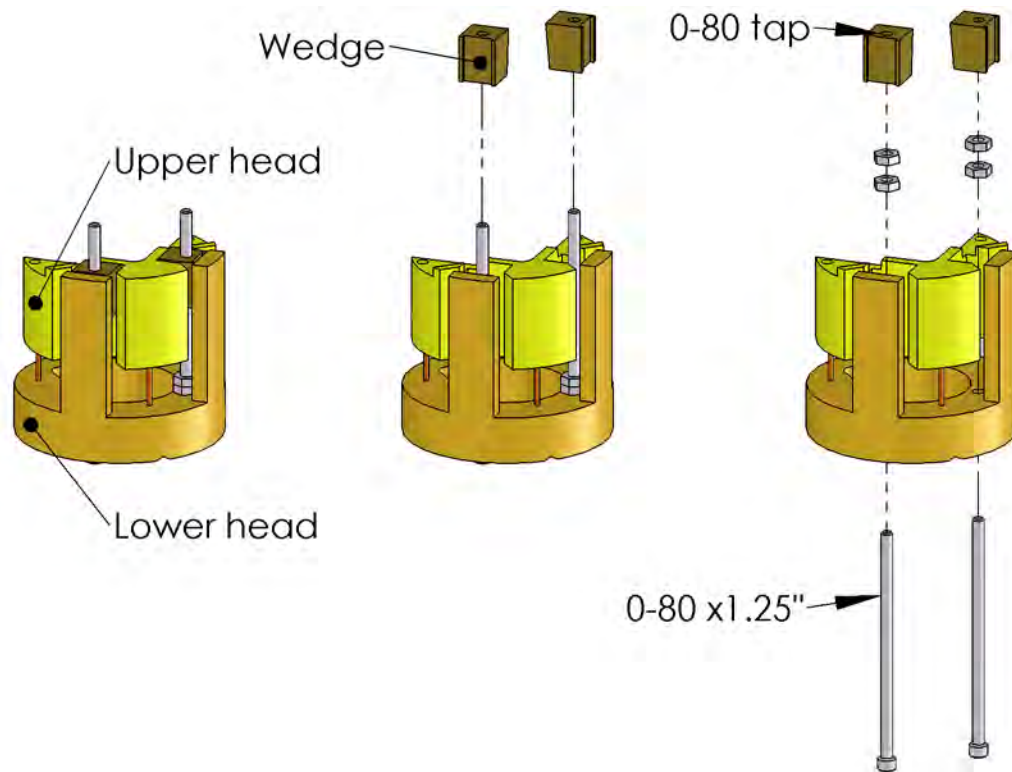

Figure 2.10: Isometric projections demonstrating the incorporation of the coarse positioning wedges into the head. (left) Head with installed wedges. (center) Exploded view illustrating installation of wedges. (right) Exploded view showing two 0-80 ×1.25" screws that hold the wedges in place and drive them along the length of the head. These two screws fit through an untapped through-hole in the head and thus can freely rotate. They are held in place with two 0.12" 0-80 nuts tightened against each other.

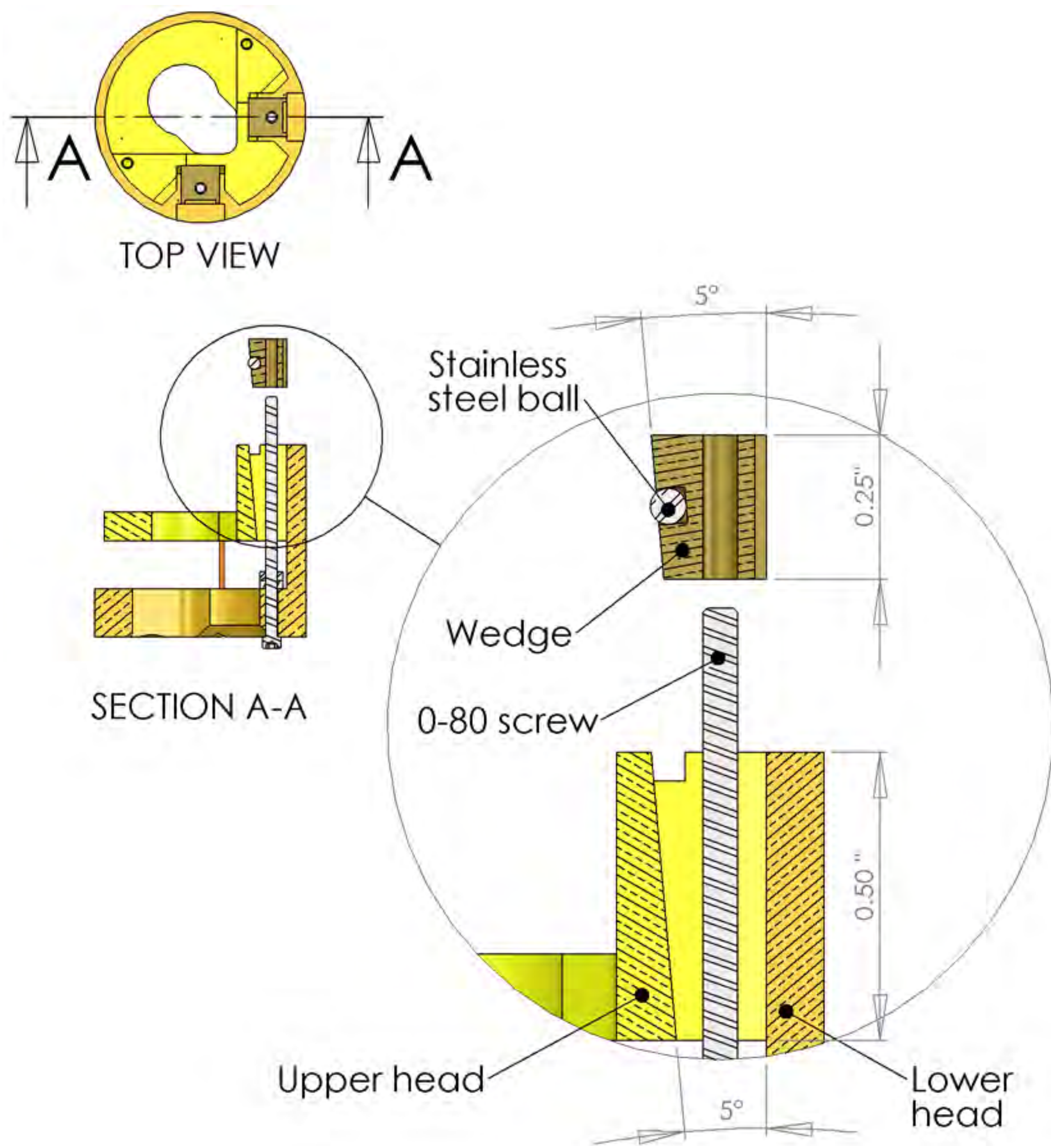

Figure 2.11: Technical drawings of the coarse positioning mechanism. (above) Top view and section of the head assembly, including wedges. (below) Detail view of section. A vertical face on the lower head opposes a near vertical face on the upper head. The 5° offset of these faces matches the offset between the corresponding wedge faces. When the wedge is moved down between these two faces, it forces the the translation of the upper head with respect to the lower head. The direction of movement created by each wedge is at right angles to each other, thus allowing for positioning in xy plane. A press fit stainless steel ball serves to reduce the contact area between the wedge and upper head, reducing the likelihood that the coarse positioning system will freeze in place at low temperature.

photo of the assembled carrier. A cantilever chip can be seen mounted on the carrier in Figure 2.12(b). The cantilever chip is held in place with a small brass shim, seen on the right hand side of the mounting head in this photo. Three 32 guage wires provide electrical connection to the cantilever and on-chip balance resistors. These wires are fed through two holes in the mounting head in order to reduce stress on their solder connections to the cantilever chip.

Two additional design considerations are of note with regards the cantilever carrier. Firstly, the upper surface of the slider, as depicted in Figure 2.12(a), is designed to be large enough to support the cantilever carrier when installed in the head assembly. Secondly, to ensure that the cantilever tip is the first part of the head to make contact with a sample, the cantilever chip mounting surface is offset by 10° with respect to the main slider face.

2.7.4 Head Assembly and Warm Temperature Alignment

The attachment of the cantilever chip carrier to the head is relatively straightforward and is shown in Figure 2.8. When installed, the cantilever points directly toward the V-groove on the front of the head, as can be seen in Figure 2.8(c). The attachment procedure involves carefully inserting the cantilever carrier into the central hole in the head and securing the cantilever carrier clamp. Flat surfaces on the cantilever carrier slider and the upper head allow for the carrier to be positioned anywhere in an area of approximately 4 mm by 4 mm prior to clamping. This flexibility of clamping placement provides the ability to align the cantilever with the sample to within approximately 10 μm. Further details of the alignment procedure are given in

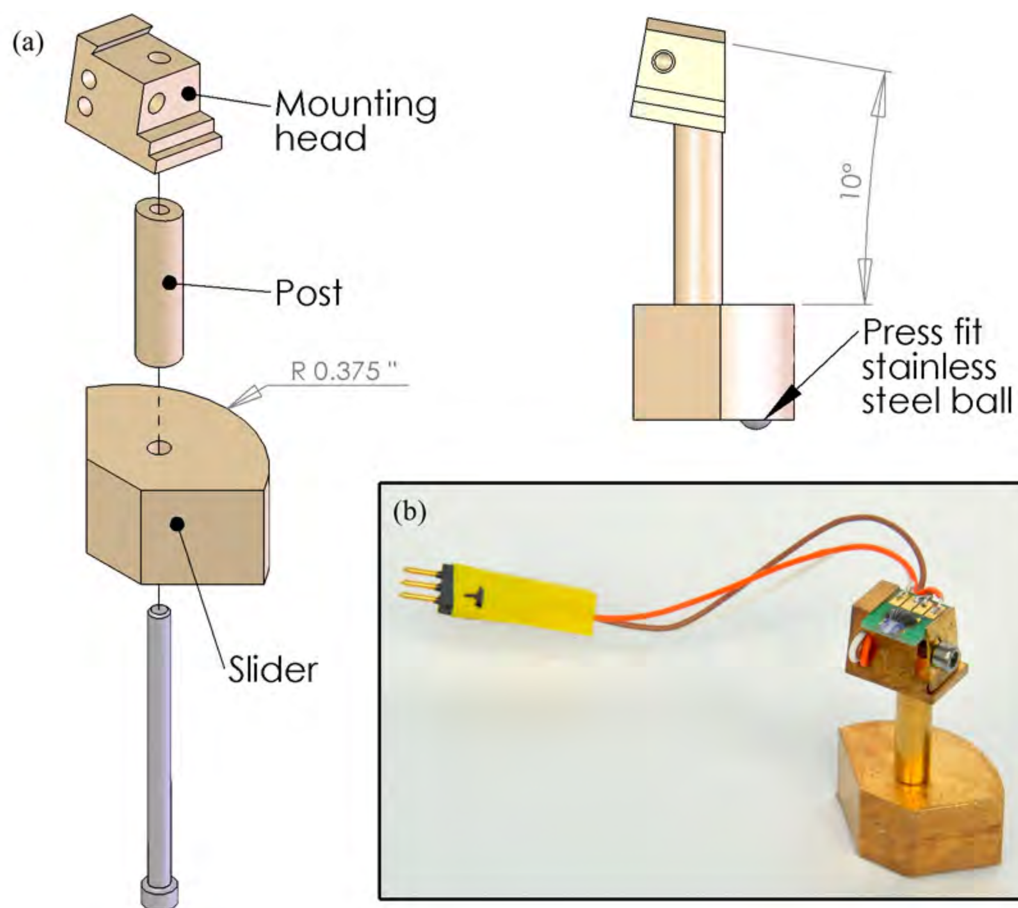

Figure 2.12: (a) (left) Exploded isometric projection of the cantilever chip mounting assembly and (right) side view of assembled tip holder. The angle of the chip mounting surface is offset by 10° with respect to the base slider to ensure the cantilever tip, rather than any other part of the cantilever chip, makes the first contact when tip and sample are brought into contact. (b) Photo of assembled holder and mounted cantilever chip. The cantilever chip is clamped in place with the small brass shim on the right hand side of the assembly. Three AWG 32 wires soldered to the cantilever chip lead to a Microtech connector and provide electrical connections to the cantilever and balance resistors.

Appendix B.

Although this alignment mechanism is similar to those of earlier implementations in the lab, three subtle differences are present. Firstly, the shape and size of the flats of the slider and upper head are such that the slider is supported both in front and behind the post connecting to the carrier head, providing more stability than previous designs. Secondly, a screw inserted into a 0-80 tapped hole at the back of the cantilever slider allows for much finer control of motion when aligning the cantilever and tip to a sample. Thirdly, a stainless steel ball bearing is press fit into the carrier slider in order to ensure the cantilever carrier clamp always applies pressure directly to the centre of the slider. The result of these changes is a more stable clamping mechanism, both while aligning the cantilever to the sample, and when cooling and operating the microscope.

2.8 Attachment of Head to Cage

A rigid attachment of the head to the cage is crucial to the operation of the microscope. To achieve this, the head is held against three M2.5-0.2 ball end set screws protruding from the cage. Figure 2.13(a) shows an exploded CAD render of the cage, ball end screws, and head. The three ball end screws align with V-grooves in the bottom of the lower head. This ball and groove design provides the ability to coarse approach in z, adjust the plane of the head with respect to the cage, and ensures that the head remains centered on the cage when cooled to liquid helium temperatures. Note that the orientation of the head is important as the cantilever must point towards the z coarse approach ball end screw. Once the head is in place,

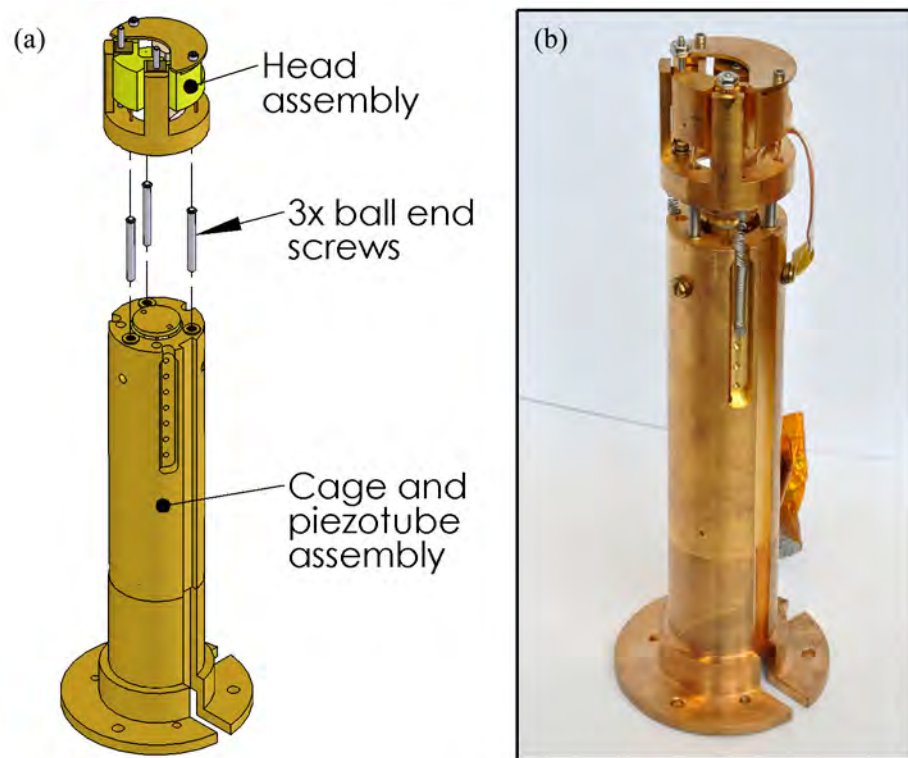

Figure 2.13: (a) Isometric projection of the microscope head and cage showing the position of three M2.5-0.2 ball end set screws. Each screw fits into a threaded bushing epoxied into the cage. The ball of each screw sits in the V-shaped groves in the bottom of the lower head to ensure that the head is rigidly held over the cage. (b) Photo of the assembled cage and head. Three springs (one visible) hold the head firmly against the ball end screws of the cage.

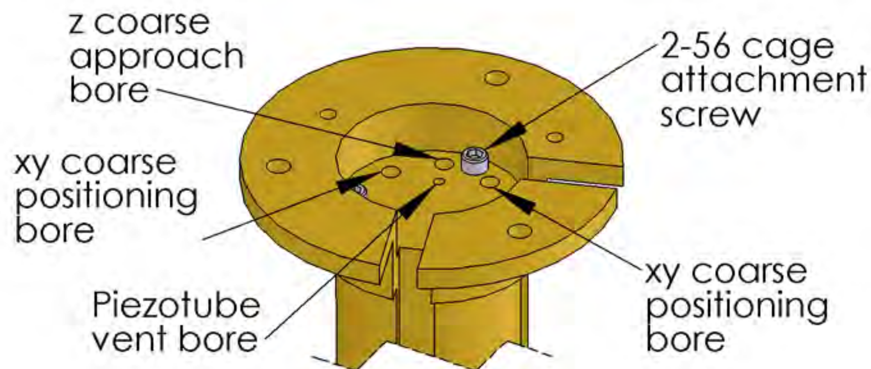

Figure 2.14: Isometric projection of the bottom of the cage base showing the two xy coarse positioning and the z coarse approach bores. Also visible are 2-56 screws attaching the cage to the cage base and a bore that vents a screw holding the piezotube assembly to the cage base.

three springs, one of which is visible in Figure 2.13(b), attach the head to the cage to ensure that the head remains in held in place throughout alignment and imaging.

2.9 Coarse Positioning Feedthrough Bores

Once the cage and head is assembled, the xy coarse positioning and z coarse approach screws are accessed through three 0.1” diameter feedthrough bores that run the length of the cage and cage base. Figure 2.14 shows a CAD projection of the bottom of the assembled microscope.

Chapter 3

Liquid Helium Cooled Cryostat

3.1 Introduction

In this chapter we discuss the construction of the liquid helium cryostat in which the microscope is cooled. The interested reader can find more comprehensive discussions of design considerations in a number of low-temperature engineering resources.[38, 39, 40, 41, 42, 43]

The low temperature scanning probe microscope is cooled through thermal contact to a liquid helium bath in a vacuum housed cryostat. Sectioned illustrations of the cryostat highlighting the various solid bodies and vacuum spaces are shown in Figure 3.1. A room temperature vacuum jacket creates the exterior of the cryostat. Housed within this are two liquid cryogen cooled jackets and their associated cryogen reservoirs. Attached to the inner of these two reservoirs is a liquid helium cooled coldplate, onto which we attach the microscope and its associated hardware. The cryostat was designed in collaboration with, and built by, Precision Cryogenic

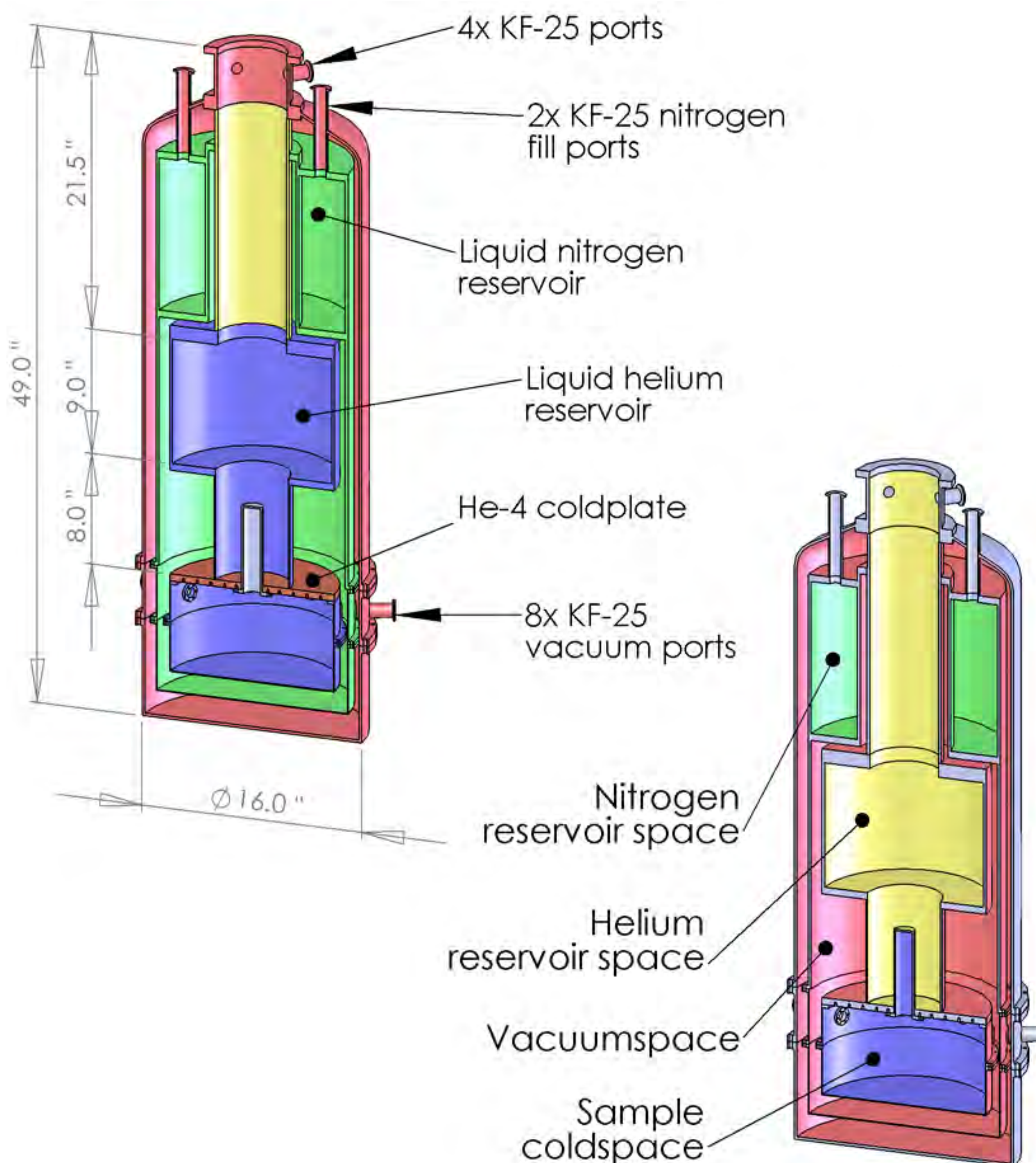

Figure 3.1: Dimetric projections of sectioned cryostat. (left) Colors highlight the various solid bodies of the cryostat. Red is the room temperature body, green is the liquid nitrogen reservoir and radiation shield, blue the liquid helium reservoir and radiation shield. The helium-4 coldplate is depicted in brown, and the fiberglass neck in yellow. (right) Colors correspond to the various closed spaces of the cryostat. Green is the liquid nitrogen reservoir space, yellow the liquid helium reservoir space. Red is the cryostat vacuum space, which also extends to the blue sample space.

Systems, of Indianapolis, IN.

This chapter begins in Section 3.2 with a description of the cryogen cooled coldplates. Section 3.3 discusses the liquid cryogen reservoirs and radiation jackets, while Section 3.4 describes access to the coldspace, during both operation and setup of the system. Section 3.5 discusses the superconducting magnet support and installed helium level monitoring hardware. Section 3.6 concerns the heat leak into the cryostat. The chapter concludes with a brief description of an alternative sample cooling method in Section 3.7.

3.2 Coldplates

A liquid helium-4 (He-4) cooled coldplate is the central feature of the cryostat. We attach the microscope to this coldplate via a secondary, helium-3 (He-3) cooled coldplate. The following subsections discuss each of these coldplates and the attachment of the microscope.

3.2.1 Helium-4 Coldplate

The He-4 coldplate is a 12" diameter, gold plated, brass disc, an illustration of which is presented in Figure 3.2. When in use, the backside of the coldplate is immersed in liquid He-4, thus cooling it to 4.2 K. The base temperature of the coldplate can be reduced to 1.7 K by pumping on the liquid helium reservoir space. A 1.0" grid pattern of holes containing 8-32 helicoils provide the ability to mount hardware to the coldplate.

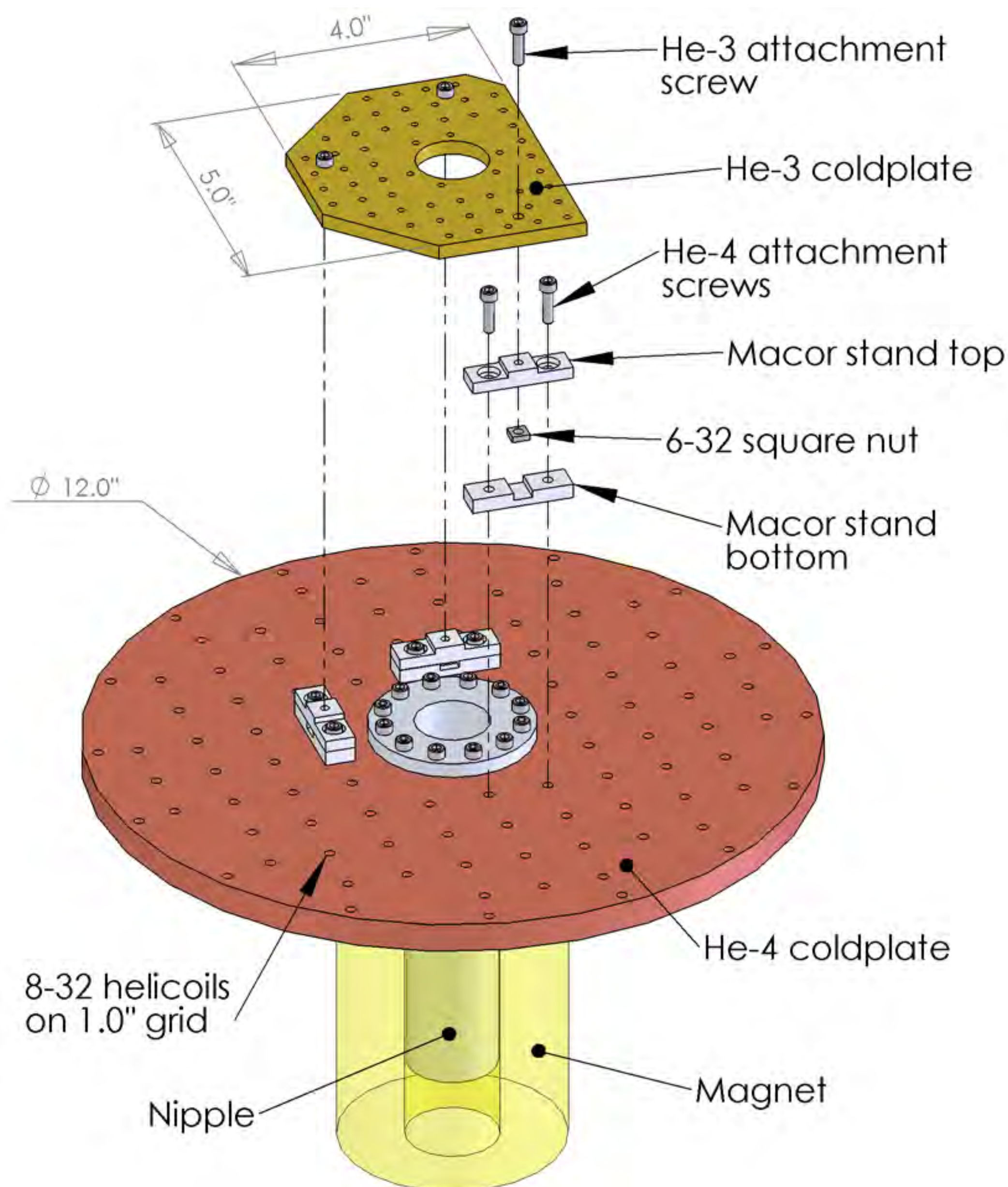

Figure 3.2: Dimetric projection of the liquid helium cooled coldplates. The He-3 coldplate is held in place with three Macor glass ceramic stands to ensure thermal isolation from the liquid He-4 coldplate. A 6" long nipple in the He-4 coldplate allows for the insertion of the microscope into the bore of a superconducting magnet mounted on the backside of the coldplate.

A 1.5” diameter hole in the center of the He-4 coldplate provides access to the bore of a superconducting magnet mounted against the coldplate’s backside. A 6” long aluminum nipple, as seen in Figure 3.2, bolts to the coldplate to separate the helium reservoir space from the sample vacuum space. An indium seal between the coldplate and nipple ensures superfluid helium cannot penetrate the vacuum space.

3.2.2 Helium-3 Coldplate

Upon installation, the microscope is attached to a secondary He-3 coldplate rather than the main He-4 coldplate. This He-3 coldplate is a 4.5” by 4.0”, 0.25” thick, OFHC copper body, as seen in Figure 3.2. When installed, a 1.5” diameter hole through the center of the He-3 coldplate is coaxial to the aluminum nipple on the He-4 mainplate, allowing for the insertion of the microscope into the magnet bore. A 0.5” grid of 4-40 tapped holes provide attachment points for the microscope and additional hardware.

The He-3 coldplate is thermally isolated from the He-4 coldplate and can be cooled to approximately 500 mK with the use of a single-stage sub-Kelvin He-3 cooler. Although not currently installed, the He-3 cooler was built to the specifications of our cryostat by Chase Research Cryogenics, of Sheffield, UK. Operating instructions for the He-3 cooler are covered in the operating manual of the cooler.

When in use, the He-3 coldplate must be thermally anchored to the coldhead of the He-3 cooler. A copper braid with cross-sectional area greater than 1 mm^2, equivalent to AWG 17, is more than sufficient to ensure the cooling power of the system is limited by the He-3 cooler rather than the anchoring mechanism. When cooling only to He-4

temperatures, this braid is connected directly to the He-4 mainplate.

We thermally isolate the He-3 coldplate by mounting it to the He-4 mainplate on three Macor stands, as seen in Figure 3.2. Macor, a glass ceramic, has a thermal conductivity of approximately 0.01 $\mathrm{Wm^{-1}K^{-1}}$ at liquid helium temperatures.[44] Given the cooling power of the He-3 cooler, we calculate that the microscope can be cooled to approximately 1 K using these Macor stands. To reach temperatures in the 500 mK range, further thermal isolation is likely necessary. We recommend constructing the stands from a stack of polymerous shim stock, such as nylon, to increase their thermal impedance.

3.2.3 Attachment of Microscope to Coldplates

Figure 3.3 shows the microscope mounted to the He-3 coldplate. The head and cage assembly is inserted through the coaxial 1.5" bores in the He-3 and He-4 coldplates, and into the aluminum nipple. Three 4-40 screws secure the cage base to the He-3 coldplate.

The inset in Figure 3.3 illustrates the position of the microscope within the nipple. The dimensions of the microscope, He-3 coldplate, and Macor stands are such that a mounted sample sits in the maximum field of a standard, 7" tall superconducting magnet.

3.3 Cryogen Reservoirs and Radiation Shields

The cryostat is constructed of three concentric radiation and vacuum jackets, shown in Figure 3.1. The outermost jacket is the room temperature wall of the

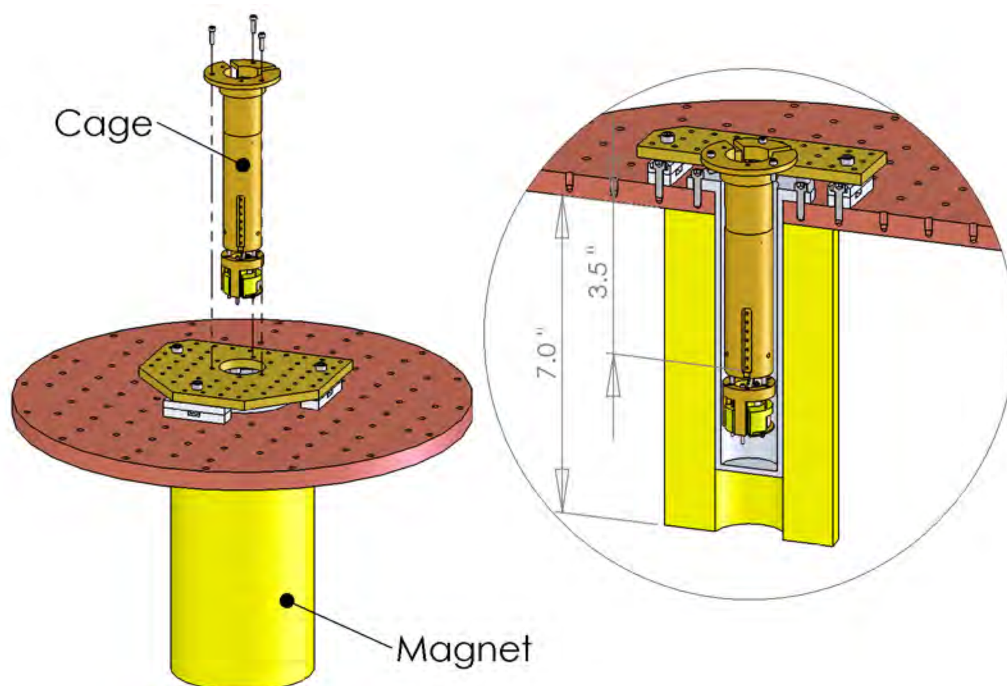

Figure 3.3: Exploded view of assembled microscope and coldplates. (inset) Cutaway of coldplates and magnet showing position of microscope cage and head. The dimensions of the cage, Macor stands, and He-3 coldplate, are such that the sample sits 3.5" below the bottom of the coldplate and in the maximum field of a 7" tall superconducting magnet.

cryostat and creates the exterior of the sample vacuum space. An intermediate jacket is cooled with liquid nitrogen and acts as a radiation shield to reduce the thermal load on the helium space. The innermost jacket is liquid helium cooled and acts as a radiation shield to protect the microscope and associated hardware from radiation emitted by bodies at higher than 4.2 K. A layer of aluminum foil is adhered to the surfaces of the radiation shields and the interior surface of the room temperature jacket. This low emissivity foil reduces the radiative heat load on the liquid cryogens. Further discussion of the radiative heat load can be found in Section 3.6.2.

3.3.1 Helium Reservoir and Radiation Shield

The He-4 coldplate is cooled through contact with liquid He-4 contained in a 15 L reservoir directly abutting the coldplate. In order to reduce the thermal load on the reservoir, a low thermal conductivity fiberglass neck connects the reservoir to the exterior of the cryostat.

A radiation shield bolted directly to the coldplate prevents blackbody radiation emitted by warmer bodies from heating the hardware attached to the He-4 coldplate. One should note that this radiation shield is not vacuum tight.

3.3.2 Nitrogen Reservoir and Radiation Shield

The 16 L nitrogen reservoir is a toroidal space enclosed in aluminum directly above the helium reservoir. Like the helium reservoir, the nitrogen reservoir connects to the exterior of the cryostat is via the fiberglass neck.

A cylindrical aluminum radiation shield, concentric to the helium cooled radiation shield, is attached to the nitrogen reservoir and runs the length of the cryostat. A 1" gap separates the nitrogen and helium radiation shields. The nitrogen shield is not vacuum tight.

3.3.3 Room Temperature Jacket

The exterior of the cryostat is a vacuum tight aluminum jacket. The 16" diameter of the vacuum jacket provides a 1" clearance to the nitrogen cooled radiation shield. Eight vacuum ports provide electrical and mechanical feedthroughs to the sample space and will be discussed in more detail in Section 3.4.1. A burst disc toward the top of the cryostat ensures venting of the cryostat if the internal pressure significantly exceeds that of atmosphere.

3.4 Access to the Coldspace

Low temperature operation of the microscope relies on our ability to electrically and mechanically access the system. Additionally, installation of the microscope and associated cooled hardware requires full physical access to the He-4 coldplate.

3.4.1 Operational Access to the Coldspace

Operational access to the vacuum space is provided by eight, KF-25 vacuum ports in the room temperature jacket of the cryostat. Access through the liquid nitrogen and liquid helium cooled radiation shields is through eight, 0.75" diameter,

feedthrough flanges positioned coaxially with the vacuum ports in the external jacket. Each feedthrough flange is surrounded by a 1” diameter bolt circle of six 4-40 tapped holes for the installation of radiation plugs. These feedthrough ports and flanges provide eight access points 1.5” above the frontside of the He-4 coldplate. Specific details of electrical and mechanical feedthroughs into the sample coldspace are discussed in Chapter 4.

3.4.2 Full Physical Access to the Coldspace

The vacuum jacket and each of the liquid cryogen cooled radiation shields can be opened and removed along two joints in each, allowing unimpeded access to the He-4 coldplate. An exploded illustration of the coldplate and radiation jackets is shown in Figure 3.4. We refer to the two removable sections of the jacket and shields as the top hat and collar. Two viton O-rings at the room temperature jacket joints ensure a vacuum tight seal of the cryostat.

Removal of the three successive top hats allows access to the coldplate for routine sample exchange and microscope installation. Additionally, the three collars can be removed for more comprehensive adjustments that require unimpeded access to the He-4 coldplate and collars, such as installation of electrical and mechanical feedthroughs.

Flipping the Cryostat

Figure 3.5(a) shows the cyrostat ready for operation. The top hats are at the bottom of the cryostat, the coldplate faces downward, and the liquid cryogen reser-

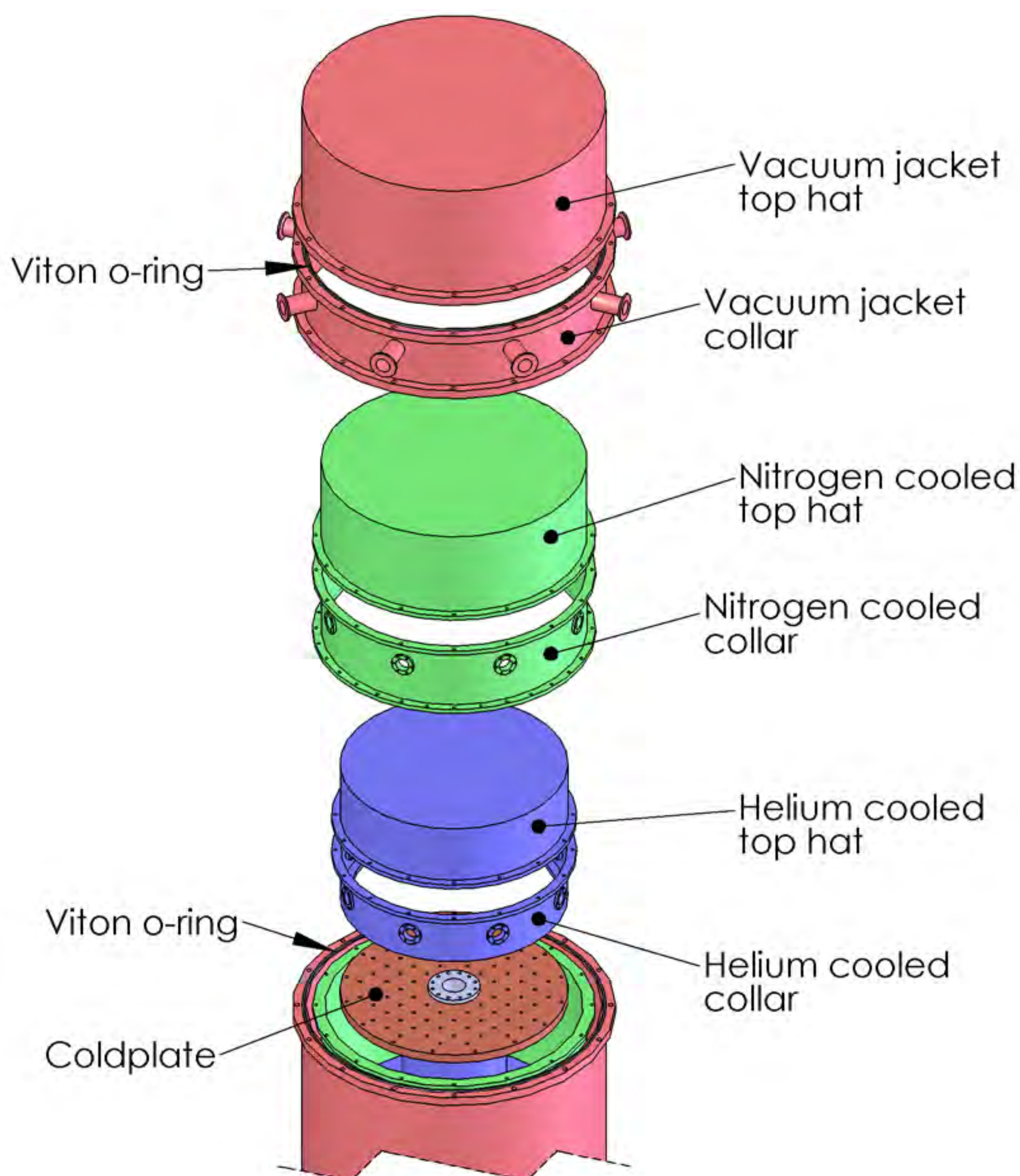

Figure 3.4: Exploded projection of cryostat top hats and collars. When assembled, the liquid helium and liquid nitrogen cooled top hats and collars provide radiation shields to ensure the cooling of the coldplate and sample. The helium and nitrogen collars each have eight feedthrough ports that align with the KF-25 ports on the room temperature collar. The two stage opening allows for the microscope to be quickly installed or removed without disturbing feedthroughs that require the use of the ports.

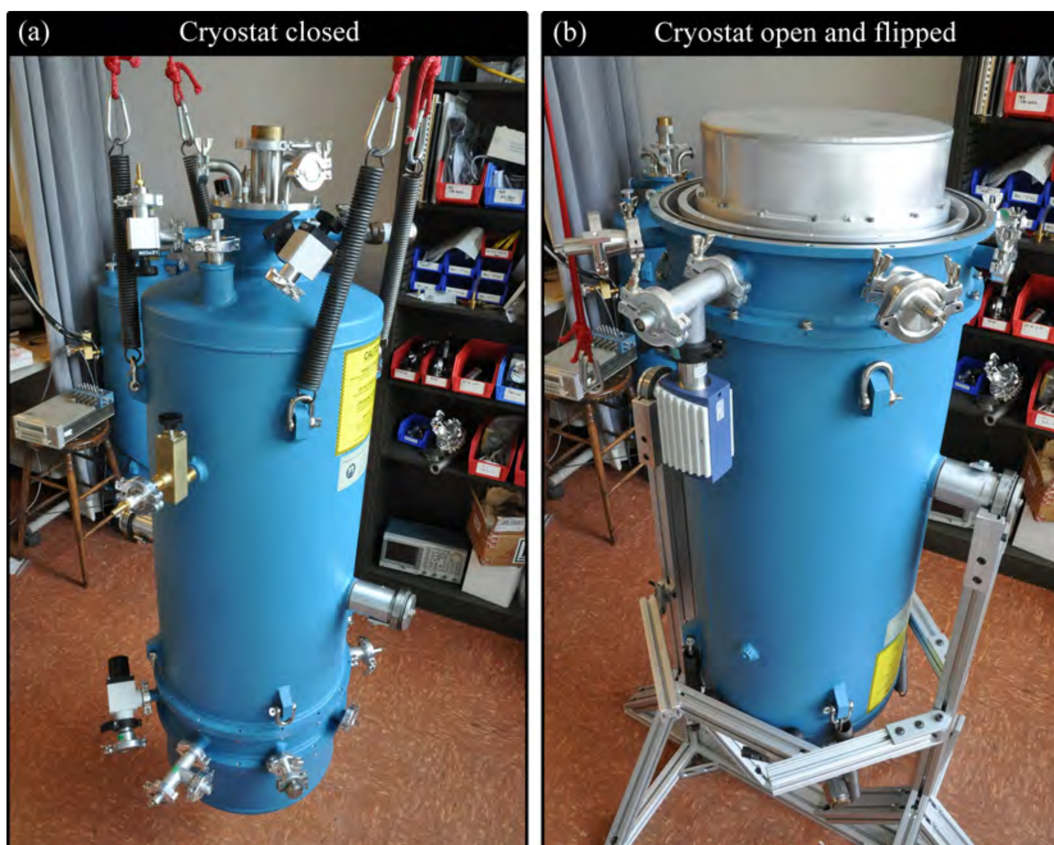

Figure 3.5: (a) Closed cryostat ready for cooling. Nylon ropes and steel springs provide vibration isolation. (b) Partially open cryostat with vacuum and nitrogen cooled top hats removed.

voirs can be filled to cool the cryostat. When installing the microscope or making adjustments to the hardware attached to the coldplate, the cryostat must be rotated such that the top hats point upward before their removal. Figure 3.5(b) shows the cryostat flipped with the two exterior top hats removed. Lifting lugs and rotating attachment points on the exterior of the cryostat allow for lifting and flipping of the cryostat. A winch on the wall of the experimental room provides a method to lift the cryostat with relative ease. Nylon ropes and steel springs suspend the cryosat from the ceiling and adequately damp most vibrations.

3.5 Magnet Support

A magnet support allows for the mounting of a superconducting magnet against the backside of the He-4 coldplate. The magnet support and its insertion into the cryostat are illustrated in Figure 3.6.

3.5.1 Copper Baffles

Six copper baffles distributed along the length of the magnet support act as radiation shields in the neck of the cryostat, reducing the radiative heat load on the liquid helium bath. This radiative heat load is discussed in further detail in Section 3.6.2.

3.5.2 Helium Level Monitoring

A liquid helium level meter and three diagnostic resistors mounted on the magnet support provide a means to monitor the liquid helium level in the reservoir during

operation. A DBEE 104 A056 Fischer connector in one of the KF-25 ports at the top of the magnet support provides electrical connections to these monitoring systems.

Helium Level Meter

An 8" helium level meter produced by American Magnetics Incorporated, of Oak Ridge, TN, is attached to the magnet support below the lowest copper baffle. This meter allows the monitoring of the helium level throughout the main reservoir space. One should note that this meter does not extend into the space where the magnet sits, and as such does not account for any liquid helium in this volume. This additional volume is approximately 1 L with a magnet installed, and 3 L without.

Diagnostic Resistors

Three diagnostic resistors are mounted along the length of the magnet support. These allow for monitoring of cryogens in the helium reservoir independently of the helium level meter, both during normal operation and liquid nitrogen precool. These resistors are attached to the magnet support plate at the base of the support stick, on the lower most copper baffle, and on the third highest copper baffle. The temperature dependence of their resistance provides a means to determine whether they are immersed in cryogens or not. The respective resistances of the magnet plate, lower baffle, and higher baffle resistors are; 1071 Ω, 1009 Ω, and 1015 Ω at room temperature; 1340 Ω, 1265 Ω, and 1250 Ω at 77 K; and 4.05 kΩ, 3.80 kΩ, and 3.87 kΩ at 4.2 K.

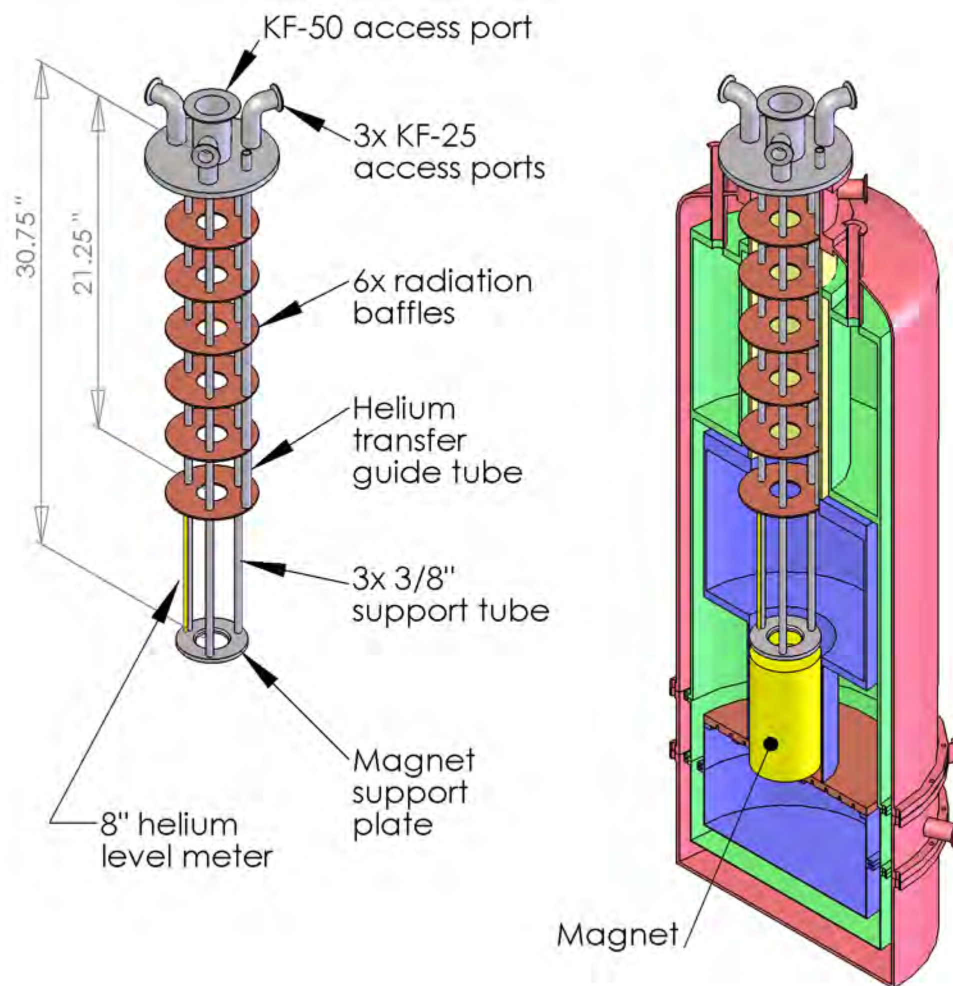

Figure 3.6: Illustrations of the magnet support. The support is comprised of three 3/8" stainless steel support tubes that hold a stainless steel support plate onto which the magnet is secured. The thermal load on the helium reservoir due to radiation incident down the neck of the cryostat is reduced by the presence of six copper radiation baffles connected to the magnet support. An 8" helium level meter attached to the lower section of the support allows for monitoring of the amount of liquid helium operation.

3.5.3 Magnet Leads

Although not currently installed, magnet leads can produce a large thermal load on the helium bath. As such, great care must be taken to ensure magnet leads are convectively cooled by cold helium gas evaporating from the helium bath. The cryostat and magnet support that house the LT-SPM are designed such that implementation of the magnet lead cooling design discussed at length in the thesis of Alex Rimberg should present no problem.[45]

3.6 Evaluation of Static Cryostat Heat Leak

In this section we assess the static heat leak of the cryostat on the liquid helium bath. This heat leak results from conductive, radiative, and convective heat transfer. Comprehensive discussions of heat transfer can be found in Bailey and Hands[46] and White.[47] Heat leak from electrical and mechanical feedthroughs will be addressed in Chapter 4.

3.6.1 Conductive Heat Leak

We use one-dimensional thermal conduction to approximate conductive heat leaks into the cryostat. Consider a thermally conducting body of length L, cross-sectional area A, and thermal conductivity $\kappa(T)$, joining two heat reservoirs at temperatures T_H and T_C. Reducing Fourier's law of heat conduction to one-dimension, the conductive heat transfer per unit time, q_{cond}, goes as,

$$q_{cond} = -\frac{A}{L}\theta(T_C, T_H), \tag{3.1}$$

where $\theta(T_C, T_H)$ is the thermal conductivity integral of the conducting body, defined by,

$$\theta(T_C, T_H) = \int_{T_C}^{T_H} \kappa(T) dT. \tag{3.2}$$

It should be noted that this analysis does not include the effects of cooling of the support structures by passing cold gas after evaporation from the helium bath, which will be discussed in Section 3.6.4.

Conductive Heat Leak of the Magnet Support

The stainless steel support rods of the magnet support contribute a significant heat leak to the system. These rods are 3/8" diameter thin wall stainless steel, which has a thermal conductivity integral from 300 K to 4.2 K on the order of 3 kW/m.[46, 48] The contribution of these three rods to the thermal load on the helium bath is approximately 300 mW.

Conductive Heat Leak Down the Neck

An additional heat leak is present due to conduction down the fiberglass neck of the cryostat. Assuming the neck is cooled only through direct thermal contact with the bath, we can put an upper limit on the expected heat leak by approximating the thermal conductivity integral from data available in Marquardt and Radebaugh[48] and Hust.[49] As the liquid nitrogen shield thermally anchors the neck at 77 K, we use the geometry of the neck and thermal conductivity integral from 77 K to 4.2 K of 15 W/m to approximate the conductive heat transfer to the helium bath to be

200 mW. We can similarly approximate the heat leak on the nitrogen bath to be 3 W, using the thermal conductivity integral of 90 W/m from 300 K to 77 K.

3.6.2 Radiative Heat Leak

Radiative heat leak can be understood by considering the net transfer of blackbody radiation between two infinite planar bodies held at temperatures T_H and T_C. It follows from the Stefan-Boltzmann law for blackbody radiation that the heat transfer per unit time per unit area, q'_{rad}, between these two bodies of identical emissivity, ε, is,

$$q'_{rad} = \sigma\varepsilon(T_H^4 - T_C^4), \tag{3.3}$$

where σ is the Stefan-Boltzmann constant. For the geometry of two concentric surfaces whose separation is much less than their size, the radiative heat transfer per unit time, q_{rad}, becomes,[46]

$$q_{rad} = \frac{\sigma\varepsilon A_C}{2}(T_H^4 - T_C^4), \tag{3.4}$$

where A_C is the surface area of the cold body. The materials used in this cryostat have emissivities of approximately 0.1 at the wavelengths of radiation dominant at the operating temperatures.

Transfer to Cryogenically Cooled Shields

Using the surface area of the liquid helium reservoir and radiation shield, we calculate the radiative heat load on the helium reservoir per unit time to be 70 mW. A similar calculation for the liquid nitrogen radiation shield indicates the radiative heat load from the room temperature jacket to be 30 W.

Reflective Layers and Superinsulation

An alternative construction, and one that is used in all other cryostats in our lab, is to forgo the liquid nitrogen cooled jacket, and replace it with 150-200 layers of aluminized mylar, commonly known as superinsulation. The result of these n floating (*i.e.* uncooled) radiation shields is to modify Equation 3.4 such that the net radiative heat transfer per unit area becomes,

$$q_{rad} = \frac{\sigma \varepsilon A_C}{2}(T_H^4 - T_C^4)/(n+1). \tag{3.5}$$

The introduction of n radiation shields reduces the radiative heat load on the cooled chamber by a factor of $(n + 1)$. We calculate the net radiative heat load on the helium space using either a liquid nitrogen radiation shield or superinsulation to be approximately equal, indicating that either method is expected to insulate the helium space adequately.

The inclusion of superinsulation increases the surface area inside the vacuum space approximately 200-fold. This increases the time required to evacuate the cryostat due to the presence water adsorbed to the internal vacuum chamber surfaces. As it is necessary to expose the vacuum space of our cryostat to atmosphere during sample exchange, we have opted not to use superinsulation in this system to avoid extended evacuation times.

Cryostat Neck

As discussed in Section 3.5.1, six copper baffles in the neck of the cryostat reduce the radiative heat load on the helium bath. Assuming that these baffles act as floating

radiation shields, we can modify Equation 3.3 such that q'_{rad} becomes,

$$q'_{rad} = \sigma\varepsilon(T_H^4 - T_C^4)/(n+1). \tag{3.6}$$

We calculate the radiative heat load down the neck of the cryostat to be 70 mW, approximately equal to the radiative heat transfer from the liquid nitrogen cooled radiation shield.

3.6.3 Convective Heat Leak

Convective heat leak is limited by the evacuated space between the room temperature cryostat exterior and liquid helium cooled sample space. An extended discussion of convective heat transfer can be found in Bailey and Hands,[46] but suffice it to say that provided the pressure is low enough that gas is in the molecular flow regime, *i.e.* the mean free path of molecules in the gas phase is much longer than the separation between cryostat walls, convective heat transfer is minimized sufficiently that its effect is negligible in comparison to the conductive and radiative heat leaks discussed earlier. Typical vacuum pressures of 10^{-5} Torr or better are appropriate to achieve the necessary thermal isolation. To aid in reaching and maintaining these pressures, the cryostat has activated charcoal mounted in the vacuum space on the rear side of the He-4 coldplate. When cooled, the large surface area of this charcoal effectively cryopumps the coldspace, ensuring excellent vacuum when cold.

3.6.4 Total Heat Leak and Expected Hold Time

The preceding calculations provide an estimate of the heat leak to the cryogen baths in the cryostat. Here we make initial estimates the hold time for each of the

cryogen reservoirs during operation of the bare cryostat.

Helium Bath

Summing the heat leaks from all forms of heat transfer, we estimate the heat load on the helium bath to be 0.7 W. Assuming this entire heat load goes toward vaporizing liquid helium, we calculate the rate of helium consumption to be approximately 0.7 L per hour, leading to a hold time on the order of 20 hours.

One should note that this is a conservative estimate of the hold time, as we have not considered the enthalpy of the helium vapor as it warms from 4 K while exiting the cryostat. This enthalpy is 70 times larger than that latent heat of vaporization for an equivalent amount of helium. Thus, we expect to observe hold times in excess of those estimated above.

Nitrogen Bath

The heat leak of approximately 30 W is compensated by the large latent heat of vaporization of nitrogen. With a boil off rate of approximately 1.5 L per hour, we estimate a hold time of approximately 10 hours, although similarly to that discussed for helium, this does not take into account the convective cooling due to exiting gasses.

3.7 Alternative Sample Insert Use

In addition to the standard operation described above, the cryostat can serve as a helium reservoir into which a sample is inserted down the cryostat neck. A KF-50 and 1.5" coupling at the top of the magnet support allow a cylindrical insert, such

as that used in the Aidala microscope, to be dropped into the liquid helium reservoir from the top of the cryostat. Bores of 1.6" diameter in each copper baffle ensure the path of the insert is unobstructed. Furthermore, the aluminum nipple in the He-4 coldplate can be exchanged for a blank flange, thus allowing the insert to penetrate the bore of a mounted magnet.

Chapter 4

Feedthroughs and Connections External to the Cryostat

4.1 Introduction

Operation of the SPM relies on the ability to electrically and mechanically manipulate the microscope and sample at cold temperature. Three rotating feedthroughs provide the ability to manipulate the z coarse approach and xy coarse positioning mechanisms of the microscope. Electrical feedthroughs provide connection to the cantilever bridge, 16 sample leads, and piezotube control lines. In order to ensure the microscope and sample thermally equilibrate with the coldplate, great care must be taken to adequately coldsink the various to the He-3 and He-4 coldplates. Consideration of the connections of hardware external to the cryostat, such as the microscope controller and vacuum pumps, is of critical importance for the elimination of ground loops that introduce noise into the detection electronics used for investigation of

nanoscale electronic devices.

This chapter is broken into two main sections, the first of which, Section 4.2, discusses considerations relating to the rotating and electrical feedthroughs into the cryostat, including an estimate of the heat leak they introduce. Section 4.3 covers connections from the cryostat to other hardware, including sample, cantilever and piezotube control leads, and connections for the evacuation and monitoring of the sample vacuum and helium reservoir spaces.

4.2 Feedthroughs

4.2.1 Rotating Feedthroughs

Figure 4.1 illustrates the rotating feedthrough assembly implemented in the microscope. Mechanical access to the coldspace is achieved through the use of three Ferrotech rotating vacuum feedthroughs (model SS-188-SLAA). A rotating shaft assembly attaches directly to the vacuum feedthrough, transferring the mechanical motion into sample coldspace. Thin wall stainless steel tubing, comprising much of the shaft's length, provides high thermal impedance between the room temperature feedthrough and the coldspace. An OFHC copper plug at the cold end of the rod assembly ensures the shaft is adequately coldsunk to an OFHC copper support stand attached to the He-4 coldplate. A Macor plug at the cold end of the shaft and a section of brass tubing provide a high thermal impedance connection to a stainless steel rod heat sunk to the He-3 coldplate.

The square cross-section of the Macor plug, brass tubing, and one end of the

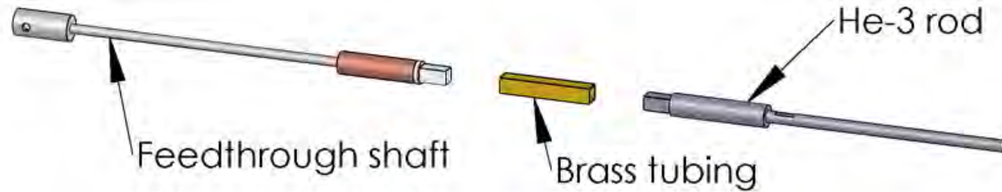

Figure 4.1: Illustration of the horizontal section of the rotating feedthrough mechanism. The feedthrough shaft connects directly to a vacuum feedthrough port in the top hat of the cryostat. A stainless steel He-3 rod is held on the He-3 coldplate and accepts a worm or mitre gear for translation of the axis of rotation from horizontal to vertical. A section of square cross-sectional brass tube transfers torque from shaft to rod while accommodating for motion of the two pieces along their axis of rotation due to thermal contraction. Additionally, the square cross-sectional dimensions of the rod, shaft, and tube, are chosen to create a weak thermal link between the shaft and rod.

He-3 rod, transfers torque from shaft to rod while allowing for thermal contraction of the of each without putting undue stress on the mechanism. Additionally, the cross-sectional dimensions of the tube are slightly larger than than if the shaft and rod to form a relatively weak thermal connection between rod and shaft. Depending on the feedthrough, a mitre or worm gear are attached to the He-3 rod to facilitate transfer of motion from the feedthrough axis to the primary microscope axis.

XY Coarse Positioning

Two vertical feedthrough rods, shown in Figure 4.2, provide access to the xy coarse positioning screws of the microscope head. Each rod is comprised of a length of 0.1" diameter thin walled stainless steel with stainless steel caps epoxied to each end. The upper cap is sized to accepts a 45 degree mitre gear (PIC Design, N1-7-S). An identical gear on the He-3 feedthrough rod transfers the axis of rotation from perpendicular to parallel to the microscope z axis. The lower cap ends in a flat head

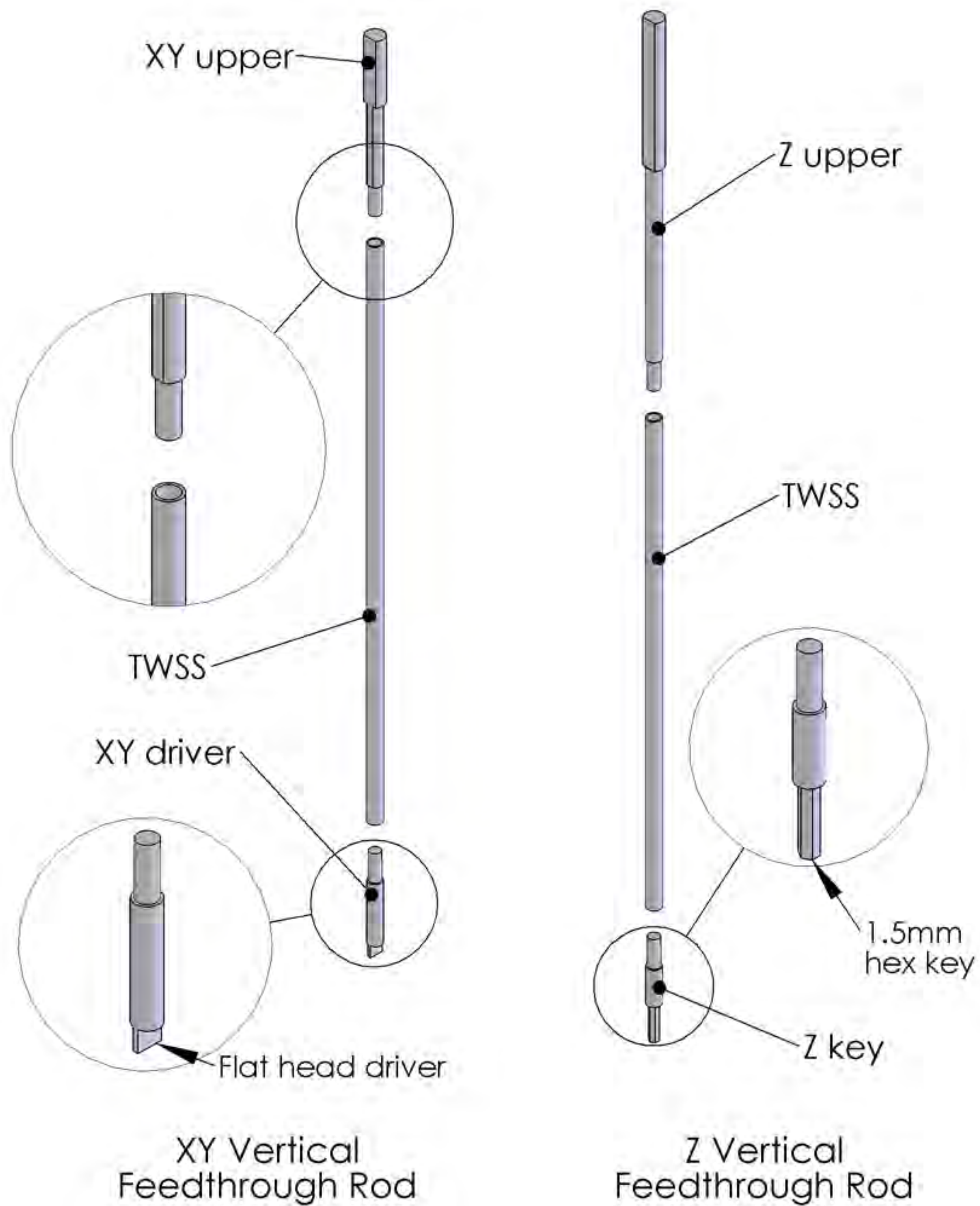

Figure 4.2: Illustrations of the xy and z vertical feedthrough rods. Each rod is comprised of a 0.1" diameter thin wall stainless steel rod with stainless steel plugs epoxied in each end. The upper plug allows for the attachment of a worm or mitre gear to drive the feedthrough, while the lower plug allows for the driving of the xy coarse position screws with a flat head driver, or the z coarse approach screw with a 1.5 mm hex driver.

driver accepted by the coarse positioning screws.

Z Coarse Approach

A third vertical feedthrough rod provides access to the z coarse approach ball end screw. The three part construction of this rod is similar to that of the xy coarse positioning feedthrough rods. The z-upper accepts a worm gear driven by a worm (PIC Design, Q8-1 and Q7-15 respectively) attached to the z He-3 rod. This gearing mechanism transfers the drive axis from horizontal to vertical and reduces the rotation by a ratio of 30:1. The lower plug of the feedthrough terminates in a 1.5 mm hex accepted by the coarse approach ball end screw.

4.2.2 Electrical Feedthroughs

In order to measure quantum effects in semiconducting electronic devices, the electron bath that connects to a sample must be thermally anchored to, but electrically isolated from, the liquid helium reservoir and coldplate of the cryostat. This section describes the techniques employed to ensure the sample, cantilever, and piezotube are thermally anchored to the liquid helium bath.

Good thermal anchoring of electrical feedthroughs introduces a conductive heat load on the coldspace. The Wiedermann-Franz law tells us that the thermal conductivity, κ, and electrical conductivity, σ, of a metal are related by,

$$\kappa \propto \sigma T, \tag{4.1}$$

where T is the temperature of the material. In order to reduce the conductive thermal load on the coldspace, high resistance materials such as fine gauge manganin wire and stainless steel are used for all electrical feedthroughs.

Sample Leads

Sample leads enter the cryostat through a 16-pin Fischer connector (DBEE 104 A086). AWG 32 manganin (a copper, manganese, nickel alloy) wire provides a high resistance electrical connection into the coldspace. Adequate coldsinking of the electrons in each lead is achieved by wrapping a three foot section of the wire around an OFHC copper spool thermally anchored to the He-4 coldplate. In order to minimize pickup in the leads, this coldsunk section of wire is folded in half and twisted on itself prior to being wrapped on the copper spool. GE varnish applied to the spool and wire during wrapping ensure good thermal contact. Further discussion of this coldsinking technique can be found in [35]. The resistances from the Fischer connector to the He-4 coldsunk wires range from 95 to 105 Ω. Similar coldsinking to the He-3 coldplate is necessary when using the He-3 cooler.

High Voltage Leads

High voltage leads for driving the piezotube enter the cryostat through a 6-pin Fischer connector (DBEE 104 A065). To reduce pickup in the sample measurement leads, high voltage driving leads are connected to the piezotube by ultra miniature stainless steel coaxial cable produced by Lakeshore Cryotronics, of Westerville, OH. Coldsinking of these cables is achieved by clamping a 2” length between two OFHC copper plates thermally anchored to the He-4 and He-3 coldplates, as described by

Smith *et al.*[50] The cable cladding is grounded at the He-4 thermal anchoring station and left floating at the Fischer feedthrough in order to break the thermal conduction path from room temperature to the coldplate via the cladding.

Cantiliver Bridge Leads

In order to reduce capacitive crosstalk to sample measurement leads, all cantilever bridge circuit leads are shielded throughout the cryostat. The cantilever leads enter the cryostat through a 6-pin Fischer connector (DBEE 104 A065) and are brought into the sample coldspace via four ultra miniature stainless steel coaxial cables. These cables enter a shielded box on the He-4 coldplate, in which they connect to spool wrapped manganin wire to ensure good thermal anchoring. Two bridge balance resistors are contained within this shielded box, while those on the tip are connected via a 4 conductor shielded cable. The shields of the coaxial cables and multiple conductor cable are connected to ground at the shielded bridge box. Similar coldsinking to the He-3 coldplate is necessary when operating the He-3 cooler.

4.2.3 Assessment of Heat Leak

The mechanical and electrical feedthroughs introduce conductive thermal leaks into the system, which we estimate according to Equation 3.1. Using the approximate value of 3 kW/m for the thermal conductivity integral for stainless steel, as was discussed in Section 3.6, we estimate the heat leak due to each of the rotating feedthroughs to be 30 mW. The ultra miniature stainless steel coaxial cable used for high voltage and cantilever bridge feedthroughs contains a AWG 32 inner conductor,

which introduces a heat leak of 0.3 mW per line. The thermal conductivity integral of manganin over this temperature range is approximately 5 kW/m,[51, 52] leading to a leak of 0.5 mW per lead.

Summing these heat leaks over all electrical and mechanical feedthroughs, we estimate the total heat leak to be less than 100 mW. This heat leak is a fraction of that due to the cryostat construction discussed in Chapter 3 and is expected to make little difference to the liquid helium consumption rate and the cryostat hold time.

4.3 Connections External to Cryostat

4.3.1 SPM Controller

The controller used to drive the SPM is currently that designed by Mark Topinka and previously used for the operation of the Topinka microscope. The function and operation of the controller are detailed at length in Topinka's thesis.[35] New breakout boxes for the cantilever and piezotube driving voltages were made to allow interfacing of the new SPM with the older controller.

4.3.2 Sample Lead Breakout

A breakout box for electrical connections to the sample connects directly to the sample lead Fischer feedthrough. The inner pin of 16 BNC plugs provide connections to the sample leads in the coldspace, the outer shield is connected to the exterior of the breakout box and cryostat, which is electrically connected to the coldplate and microscope cage. A switch for each lead will ground, float, or bus its center pin.

A 17th BNC on the breakout box provides the connection point of the cryostat to ground. The inner pin of this BNC should be connected directly to the grounding bar on the electronics rack. Connection of the digital to analog converter, analog to digital converter, and current and voltage preamplifiers to the sample lead breakout box do not introduce ground loops as the outer BNC connections of these electronics float with respect to ground. However, this is not the case for the PAR 124 lock-in used in the system, and as such, the separate ground connection should be removed when the lock-in is connected to the breakout box.

4.3.3 Cable Connections

The cryostat is connected to breakout boxes for the cantilever bridge circuit and high voltage piezotube driving lines by multiple-conductor cables with Fischer plugs at each end. The ground shield of each cable is connected to only one of the Fischer plugs. This ensures the inner conductors are shielded while avoiding the introduction of ground loops into the system.

4.3.4 Vacuum Valves

Two vacuum valves are connected to the cryostat to allow the evacuation of the sample and helium reservoir spaces. To ensure electrical isolation of the cryostat and pumps, each valve is attached to the cryostat with an insulating plastic clamp and plastic O-ring spacer.

4.3.5 Pressure Sensor

An Inficon BPG400 pressure gauge is attached to one of the KF-25 ports on the cryostat to allow monitoring of the internal pressure throughout cooldown and operation. When connected to a gauge controller, the gauge body is grounded. In order to ensure ground loops are not introduced into the measurement system, the gauge is electrically isolated from the cryostat by attaching it with a plastic clamp and plastic O-ring spacer.

Chapter 5

Demonstration of Function

5.1 Introduction

The ability to maintain cold temperature, approach and scan the SPM above a sample is the ultimate test of the system. Here we discuss operational aspects related to the cooling and scanning of the microscope, including the measured hold times and drifts, and a demonstration of topographic scanning of the SPM. Operational procedures relating to cooling the system are discussed in Appendix D.

5.2 Hold Times

The observed hold times of the cryostat exceed the specifications that were laid out in Chapter 1. We find the initial helium fill hold time to be approximately 60 hours, much longer than the estimate discussed in Chapter 3. As the initial fill must cool the coldplate and microscope from 77 K to 4.2 K, we expect subsequent fills to have

even longer hold times. The hold time of the nitrogen reservoir is around 36 hours, providing plenty of buffer time should refilling be unexpectedly delayed.

5.3 Drift

The microscope tip tends to drift with respect to the sample position as the cryostat is cooled to liquid helium temperature. This is due to mismatched thermal contractions in the microscope body, predominantly those between the piezotube and microscope cage. Drift occurs in both the z direction and that in the xy plane. Most thermal contraction occurs between room and liquid nitrogen temperatures, thus is it possible to test the microscope following a liquid nitrogen precool to understand whether the drift is likely to cause significant problems in terms of approaching the sample.

5.3.1 Z Drift

As the microscope is cooled, the tip drifts toward the sample. To avoid crashing the tip, it must be backed away from the sample surface prior to cooling. Three and a half turns of the z coarse approach screws (100 turns of the external z feedthrough) is sufficient to ensure the tip does not crash during cooling. Once at cold temperature, approximately 20 turns of the external feedthrough will bring the tip into contact with the sample.

5.3.2 XY Drift

Drift in the xy plane is usually no more than 70 μm and tends to be repeatable for a given piezotube. When cooling a piezotube for the first time, it is recommending to align the tip to the center of a 200 μm$\times$200 μm alignment pattern for initial drift measurement.

5.3.3 Additional Tip-Sample Movement

In addition to drift during cooling, bumps and knocks to the microscope can disturb the tip position relative to the sample. The most extreme movements observed in the Aidala and Topinka microscopes are on the order of 50 μm, although movement of 5-10 μm is more common. The greatest risk of movement is during initial alignment, nitrogen precool, and helium cooling. In this system, we have observed movements of no more than 1 μm during the most disruptive procedures of top hat installation, cryostat flipping, and sample space evacuation.

5.4 Scanning

As discussed in Chapter 2, the scan range in x and y is approximately 30 μm at room temperature and 10 μm at liquid helium temperature. These correspond to measured voltage to movement ratios of approximately 8 V/μm and 22 V/μm respectively. The response of the piezotube at liquid nitrogen temperatures is similar to that at room temperature.

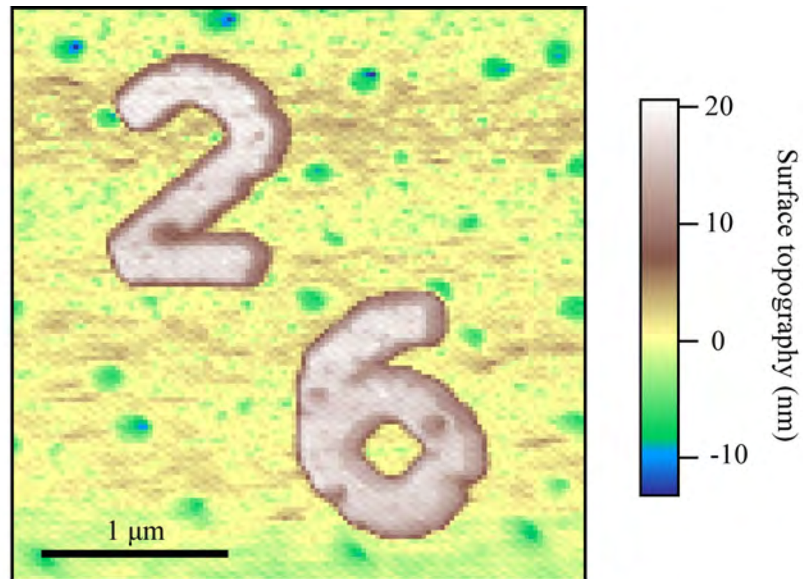

Figure 5.1: Topographic scan of gold alignment markers on a silicon substrate. The numbers are easily identifiable and pits on the substrate surface can clearly be seen.

The initial test of the SPM is its ability to acquire detailed topographic images. Figure 5.1 shows a topographic scan of a set of numbers used to indicate the position of the tip on a sample. The numbers are 20 nm of gold deposited on a silicon substrate. Not only are the numbers easily identified, pits in the substrate on the order of 5 nm in depth and 20 nm in size are clearly visible in the scan.

Chapter 6

Electrostatic Force Microscopy

6.1 Introduction

Electrostatic force microscopy (EFM) is an atomic force microscopy technique sensitive to the capacitive coupling and potential difference between a conducting sample and SPM tip.[53, 54] The technique is based on the measurement of cantilever deflection induced by the electrostatic force between tip and sample. Here we demonstrate the ability to image the spatial variation in capacitive coupling to a reference sample using EFM measurements in our LT-SPM.

In this chapter we discuss the theoretical basis of EFM, details of the experimental setup, fabrication of samples, and scanning procedure. EFM scans at room and liquid helium temperatures are presented and allow us to estimate the resolution of capacitive coupling based imaging techniques. Future directions and implications to alternative SPM techniques conclude the chapter.

Figure 6.1: (a) Schematic diagram illustrating the capacitive coupling between a conducting tip and sample. Capacitances from the tip to the sample, C_{tip}, and the bulk of the cantilever to the sample, C_{cant} contribute to the total capacitance, C. V_{tip} and V_{sample} are voltages applied to the tip and sample respectively. (b) Schematic identifying the tip-sample separation, z, and the cantilever deflection, Δz. Note that these schematics are not to scale.

6.2 Theoretical Basis

To probe the capacitive interaction that EFM is based on, a conducting SPM tip sits at a height z above a conducting sample, as shown in Figure 6.1. The capacitive coupling between the tip and sample is characterized by a capacitance, C. Voltages V_{tip} and V_{sample} are applied to the tip and sample respectively. Thus, the energy stored in this capacitive system, U, is given by,

$$U = -\frac{1}{2}C\Delta V^2, \tag{6.1}$$

where ΔV is the potential difference between the tip and sample. For the purposes of this experiment, we will assume that the contact potential difference between the tip and sample is negligible in comparison to the applied voltages, allowing us to write,

$$\Delta V = V_{tip} - V_{sample}. \tag{6.2}$$

The capacitive coupling introduces a force on the cantilever in the z direction, F, given by,

$$F = \frac{1}{2}\frac{\partial C}{\partial z}\Delta V^2. \tag{6.3}$$

This force deflects the cantilever as per Hooke's law,

$$\Delta z = \frac{F}{k}, \tag{6.4}$$

where k is the spring constant of the cantilever.

If we consider applying a voltage difference with both DC and AC components, ΔV becomes,

$$\Delta V = V_{DC} + V_{AC}\sin(\omega t), \tag{6.5}$$

where ω is the angular frequency of the applied AC voltage. We can now expand Equation 6.3 as,

$$F = \frac{1}{2}\frac{\partial C}{\partial z}\left(\left[V_{DC}^2 + \frac{1}{2}V_{AC}^2\right] + \left[2V_{DC}V_{AC}\sin(\omega t)\right] + \left[\frac{1}{2}V_{AC}\cos(2\omega t)\right]^2\right). \tag{6.6}$$

This force contains terms constant in time, oscillating at frequency ω, and oscillating at frequency 2ω.

Observing cantilever deflection at DC is difficult as the cantilever signal has the propensity to drift during a scan due to thermal fluctuations or proximity to charged defects. If the driving frequency is chosen to equal the resonant frequency of the cantilever, an amplification of the signal by the quality factor of the cantilever is observed. However, we find this amplification to be unnecessary in our experimental setup and use a frequency well below the resonant frequency of the cantilever. For the remainder of this analysis we consider observation of the cantilever deflection at

the AC driving frequency, ω. The ω component of the capacitive force, F_ω, is equal to,

$$F_\omega = \frac{\partial C}{\partial z} V_{DC} V_{AC} \sin(\omega t). \tag{6.7}$$

If we now consider only the ω frequency component of Δz, substitution of Equation 6.4 into Equation 6.7 reveals,

$$\Delta z_\omega = \frac{\partial C}{\partial z} \frac{V_{DC} V_{AC}}{k} \sin(\omega t), \tag{6.8}$$

where Δz_ω is the ω frequency oscillatory cantilever deflection. Thus, by measuring the cantilever deflection at the applied AC frequency as a function of tip position, we can probe the spatial variation of sample potentials and $\frac{\partial C}{\partial z}$.

Cantilever Contribution

The total capacitance from the sample to the cantilever and tip can be broken into two component parts, illustrated in Figure 6.1(a) and described by,

$$C = C_{tip} + C_{cant}, \tag{6.9}$$

where C_{tip} is the capacitance between the tip and the sample, and C_{cant} is the capacitance between the bulk of the cantilever and the sample. From Equation 6.8 and Equation 6.9, we find,

$$\Delta z_\omega = \left(\frac{\partial C_{tip}}{\partial z} + \frac{\partial C_{cant}}{\partial z} \right) \frac{V_{DC} V_{AC}}{k} \sin(\omega t). \tag{6.10}$$

Due to the cantilever's large spatial extent, the C_{cant} component introduces a constant term in the oscillation amplitude.[55] Subtraction of this constant term from an EFM scan isolates the C_{tip} term, which varies depending on the local sample

Figure 6.2: Scanning electron micrograph of 20 μm×20 μm reference electrode pattern on a silicon substrate. Each arm of the pattern is 200 nm in width and made of 17 nm thick thermally evaporated gold atop a 3 nm layer of chromium.

geometry and voltage. It is this C_{tip} term that is of most interest in terms of tip-sample interaction for LT-SPM techniques.

6.3 Experimental

6.3.1 Calibration Sample Fabrication

The calibration samples used in this experiment are gold/chrome electrode structures patterned on a silicon substrate. The sample substrates are 2 mm×3 mm chips of 500 μm thick, n+ doped silicon with a 300 nm thermal oxide on the top surface. These chips are prepatterned with bond pads and master electrodes as discussed in the thesis of Erin Boyd.[36] Chips are chemically cleaned in trichloroethylene and a bilayer of polymethylmethacrylate (PMMA) (495PMMA A2% and 950PMMA A2%, Michrochem Inc.) is spun onto each chip. A pattern of 200 nm wide interconnecting electrodes and alignment marks are written on the sample by electron beam lithography. The PMMA resist is developed in a 3 part to 1 part by volume, IPA:MIBK

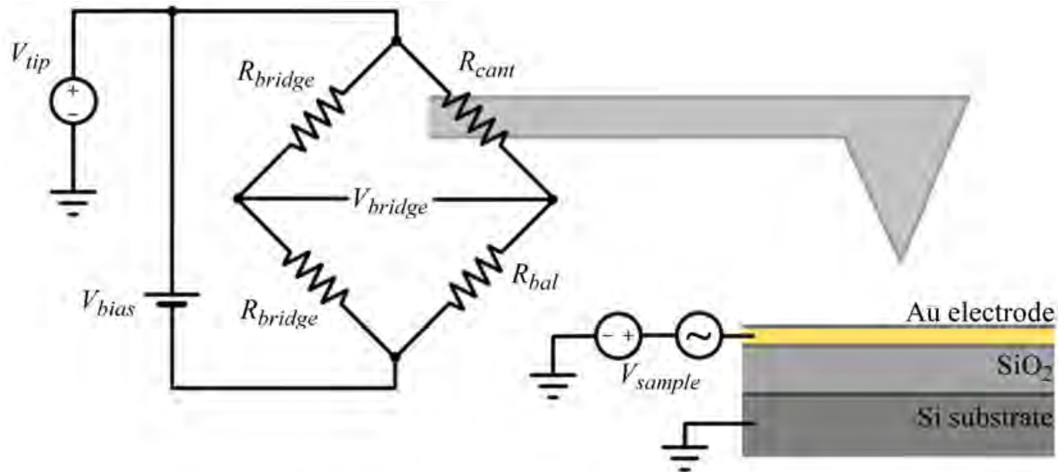

Figure 6.3: Schematic of sample and applied voltages for EFM measurements. The sample voltages are carried by a gold electrode insulated from a grounded silicon substrate by a 300 nm layer of silicon oxide. The voltage applied to the gold electrode, V_{sample}, contains both DC and AC components, whereas the voltage applied to the tip, V_{tip}, is DC only. V_{tip}, and the DC component of V_{sample} are sourced from the SPM controller. The AC component of V_{sample} is sourced from a PAR 124 lock-in amplifier, which is also used to measure the AC component of V_{bridge}.

developer solution for 60s, quenched in IPA, and blown dry with nitrogen gas. A 30 second oxygen plasma etch is used to remove residual PMMA from the silicon substrate and reduce surface roughness at the pattern edges. 3 nm of chromium and 17 nm of gold are deposited onto the sample by thermal evaporation. The remaining EBL resist is removed in acetone and samples are stored in dry nitrogen until measured. A scanning electron micrograph of a typical sample structure is presented in Figure 6.2.

6.3.2 Electronics

Figure 6.3 shows a schematic of the electronics used to operate the SPM in EFM mode. DC voltages sourced from the SPM controller are applied to both the tip

and sample. In order to induce cantilever oscillation, an AC voltage at a frequency, $f = \frac{\omega}{2\pi}$, of 4.65 kHz sourced from a PAR 124A lock-in amplifier is applied to the sample. This AC voltage is applied to the sample rather that the cantilever in order to avoid direct coupling to the cantilever bridge voltage. Cantilever deflection is measured with a Wheatstone bridge as discussed in Chapter 2. The component of the cantilever bridge voltage, V_{bridge}, at frequency ω is detected by standard lock-in techniques using a PAR 118 preamplifier and PAR 124A lock-in amplifier. The silicon substrate is grounded throughout scanning experiments.

6.3.3 Electrostatic Force Microscopy Scanning Procedure

EFM measurements are taken in a two pass technique. With tip and sample voltages set to zero, the average plane of the substrate is determined so that a constant tip-sample height can be maintained throughout subsequent scans. The tip is brought into contact with the sample and scanned over the region of interest, allowing the topography of the sample to be measured as a function of xy position over the scan region. These topographic scans reveal the location of electrodes on the substrate surface. A subsequent EFM measurement is taken by lifting the tip 25-40 nm above the sample substrate (5-20 nm above the sample electrodes), applying appropriate voltages to the tip and sample electrodes, and scanning the tip over the region of interest. The component of the bridge voltage oscillating at the frequency of the applied AC electrode voltage is recorded as a function of tip position over the scan region.

6.4 Results

In this section we present preliminary results of EFM measurements on gold electrode samples. We demonstrate the ability to scan over large (3 μm $\times$ 3 μm) scan areas and observe changes in an EFM signal correlated with the underlying electrode pattern. Estimates of the resolution of the SPM working in EFM mode are obtained by imaging features on the order of 100 nm and through analysis of the lineshapes of scanning data from isolated electrodes.

6.4.1 Large Area Scanning

Figure 6.4(a) presents a topographic scan of the electrode pattern, clearly showing the location of electrodes that rise 20 nm above the substrate surface. Figure 6.4(b) shows the cantilever deflection amplitude when scanning in EFM mode with the tip is raised 20 nm above the electrode at room temperature. The deflection amplitude is approximately 10% larger when the tip is directly over the electrode. This corresponds to an additional force on the cantilever of 12 nN.

As the sample contains one contiguous electrode, changes in the cantilever deflection reflect variations of $\frac{\partial C}{\partial z}$ with tip position, rather than spatial variations of the sample potential. When the tip is proximal to the electrode, the cantilever deflection indicates an increase in the z derivative of the tip-sample capacitance, *i.e.* the C_{tip} term in Equation 6.10. We approximate $\frac{\partial C_{tip}}{\partial z} = 0.5$ aF/nm when the tip is directly over the center of the electrode pattern.

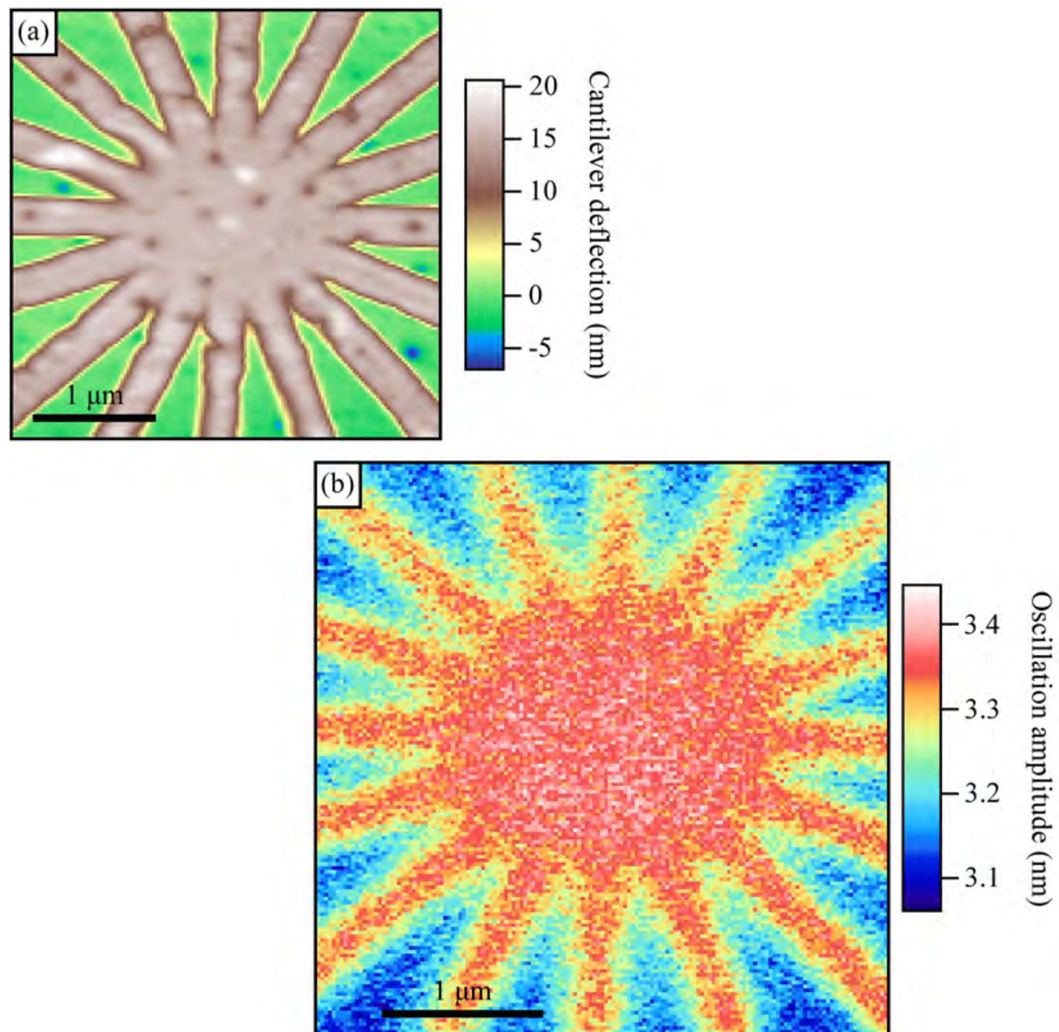

Figure 6.4: (a) Topographic and (b) EFM scans of a reference pattern at room temperature. In (b), the tip is scanned 20 nm above the surface of the electrodes with V_{tip} = +5 V, V_{sample} has a DC component of -7 V and an AC component of 2 V oscillating at 4.65 kHz. The cantilever deflection at this driving frequency is clearly correlated with the underlying electrode pattern.

6.4.2 Scanning Resolution of Electrode Gap

The EFM scanning technique in this SPM is sensitive to electrode geometries down to the scale of approximately 100 nm. Figure 6.5(a) shows a scanning electron micrograph of the region where two electrode arms meet. The radius of curvature where the arms of the electrode meet is less than 5 nm. Figure 6.5(b) shows a topographic SPM scan of the same region, revealing a topographic scanning resolution of approximately 50 nm. This is larger than the nominal tip radius of 20 nm, indicating a somewhat worn tip.

EFM scanning of the same region, shown in Figure 6.5(c), with the tip 10 nm above the surface of the electrode, demonstrate the ability to image the gap between the arms of the electrode. We estimate the resolution of EFM scanning for the detection of gap in local electrodes to be 30 nm. This resolution estimate corresponds to the minimum radius of the contour representing a 10% drop in the EFM signal from that directly over the electrode.

6.4.3 Scanning Resolution of Isolated Electrode

Figure 6.6(a) shows an EFM deflection scan of an isolated 200 nm wide electrode. This scan is taken at 4.2 K with the tip held 5 nm above the electrode. The average cantilever oscillation amplitude over the cross-section of this scan is shown in Figure 6.6(b). From this scan we can determine our ability to resolve the size of an isolated electrode. We estimate the resolution to be the distance the tip must travel for the electrostatic force due to C_{tip} to rise from 25% to 75% of the value over the electrode. This indicates an EFM resolution of 85 nm.

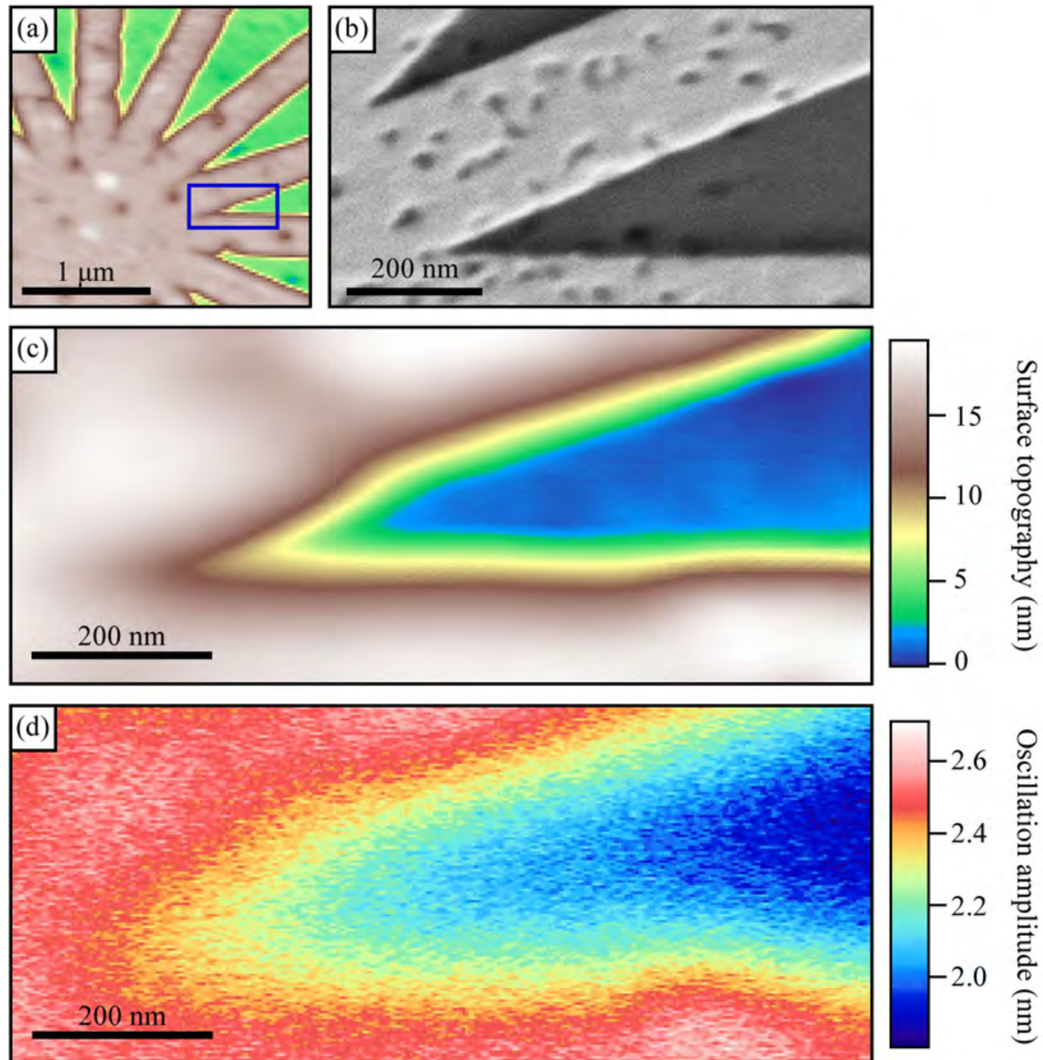

Figure 6.5: (a) Topographic scan of patterned electrode. (b) Scanning electron micrograph of the area of interest of a typical reference pattern. (c) Topographic scan of blue sectioned area in (a). (d) EFM scan over the same area as (c) including contributions from C_{tip} and C_{cant}. The tip is scanned 10 nm above the surface of the electrodes, $V_{tip} = +5$ V, V_{sample} has a DC component of -7 V and an AC component of 2 V oscillating at 4.65 kHz. All images are taken are room temperature.

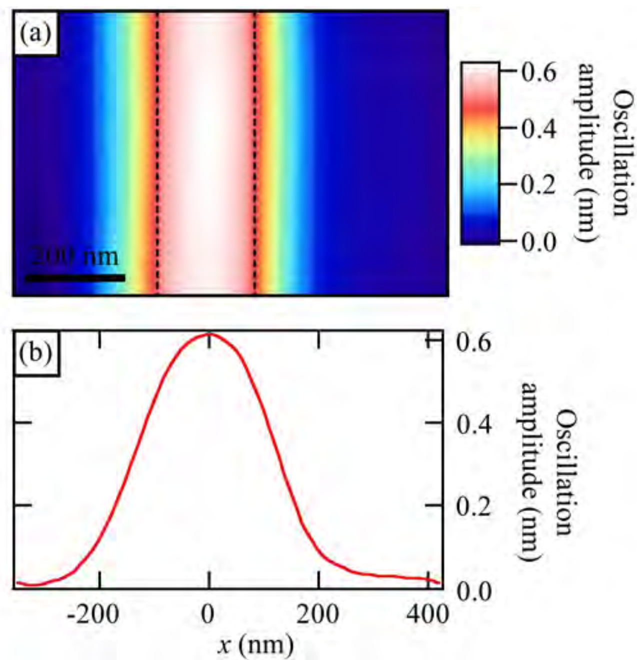

Figure 6.6: (a) C_{tip} contribution to EFM oscillation amplitude of a cantilever scanning 5 nm above the surface of a 200 nm wide electrode at 4.2 K. The position of the electrode is represented by two vertical dotted lines. The electrode voltage has a DC component of -5 V, and an AC component of 2 V oscillating at 4.65 kHz. The voltage on the tip is set to 0 V. (b) Average line scan of the EFM image in (a) centered on the electrode.

The EFM signal quickly drops to zero as the tip moves away from the center of the electrode. The full width at half maximum of the averaged scan trace in Figure 6.6 is 270 nm, within our estimated EFM resolution.

A 10% change in the deflection signal due to a the movement of the tip is well within our ability to image at 4.2 K. As such, we can conclude that changes of $\frac{\partial C}{\partial z}$ on the order of 0.1 aF/nm are more than adequate for the detection of the electrostatic force.

6.5 Discussion and Outlook

In this section we have demonstrated the ability to use the SPM as a capacitive probe to investigate electrostatic forces between the tip and a patterned electrode. The measurement of cantilever deflection due to the electrostatic force indicates a resolution of this technique of 80 nm to measure the width of an isolated electrode. Observation of relative changes in tip-to-electrode coupling allow us to detect gaps in electrodes on the order of 30 nm. We now turn to the implications of these results to scanning probe techniques for the investigation of nanometer scale electronic devices.

Firstly, let us consider the possibility of using EFM to detect the presence of an electron on a quantum dot. From Equation 6.3, we can write the force on the cantilever as a function of the z derivative of the tip-to-dot capacitance, and the potential difference between tip and dot. Provided a quantum dot can charge and discharge from a source or drain, the largest potential difference to be expected between the SPM tip and the dot would be equal to the energy required to add an electron to the dot divided by the electron charge. Even in very small nanowire systems, the

largest we can expect this voltage to be is on the order of a 10 mV. If we estimate $\frac{\partial C}{\partial z}$ as 0.1 aF/nm, a generous estimate given the spatial extent of a quantum dot, we calculate the force between the tip and dot due to the addition of a single electron to be on the order of 10 fN. Although this force is within the detection limit of AFM, we would need to gain five orders of magnitude in force sensitivity to be able to measure this in our LT-SPM. Operating at the resonant frequency of the cantilever, we could increase sensitivity by approximately three orders of magnitude. Achieving significantly more force sensitivity with our current cantilevers is unlikely. As such, we conclude that detection of single electrons is likely not possible with the current setup. However, the head design allows for a relatively uncomplicated transition to different piezoresistive cantilevers if more suitable options are identified.

Secondly, we consider the possibility of oscillating the cantilever to induce electronic transport through a quantum dot or multiple dot system experiencing Coulomb blockade. Let us start by supposing we can oscillate the cantilever such that the amplitude at the tip is on the order of 5 nm and that $\frac{\partial C}{\partial z}$ is 0.1 aF/nm. If the voltage difference between tip and dot is on the order of 5 mV, the change in energy of the capacitive system will be approximately 0.1 meV. This is comparable to that of the thermal energy at 1 K, and is thus large enough to control charging and discharging events of the quantum dot. In conclusion, although the SPM does not currently accommodate the mechanical oscillation of the tip, we believe inclusion of this into the head would allow the ability to control the charge state of a quantum dot with the oscillation of a nearby LT-SPM tip.

Chapter 7

Double Quantum Dot Conductance Image Simulations

7.1 Introduction

Semiconductor nanowires show great promise for applications in nanoelectronics, spintronics, quantum information processing, and nanophotonics.[56, 57, 58] A subset of these systems, semiconductor heterostructure nanowires, allow for the highly controlled incorporation of ultrasmall structures, such as quantum dots, with atomically sharp interfaces, and highly controllable size and composition within nanowires.[3, 10, 58] InAs is a particularly attractive candidate for potential applications due to its large, tunable g-factor,[59] surface charge accumulation layer,[60] and well characterized growth mechanism.[61, 62]

SGM has been used to image and manipulate the electronic charge in InAs/InP heterostructure nanowire quantum dots.[25, 26, 27] Coulomb blockade provides the

imaging mechanism by which this technique is used to elucidate system parameters, such as the location of a dot along a wire, charging energy of the dot, and the energy difference between electronic quantum states within the dot. The LT-SPM tip acts as a local, moveable, electrostatic gate, capacitively coupled to the quantum dot. The capacitive coupling between the tip and dot is tunable, as it depends on the geometrical parameters of the system, *i.e.* the position of the tip with respect to the dot in x, y, and z.

Single-electron quantum dots in InAs/InP heterostructure nanowires are attractive for spin manipulation due to their small size and the close proximity of the two dots. Gating these systems is challenging as dot size and spacing is typically smaller than the resolution of lithographic techniques used to define gates.

In this chapter we present simulations that demonstrate the ability to extend work in imaging single quantum dots in InAs/InP heterostructure nanowires to double quantum dot systems. The chapter begins with a theoretical treatment of single and double quantum dots in Section 7.2. Section 7.3 outlines the details of SGM conductance image simulations. The results of simulations are presented in Section 7.4. A brief discussion concludes the chapter in Section 7.5.

7.2 Theoretical Background

7.2.1 Coulomb Blockade in Single Quantum Dots

Let us consider a system consisting of a quantum dot capacitively coupled to a nearby electrostatic gate and connected to source and drain leads by tunnel junctions.

A circuit diagram of this quantum dot system is shown in Figure 7.1. Provided that the tunnel junctions sufficiently isolate electrons on the dot from those in the leads, quantum confinement will result in a discrete electronic energy spectrum on the dot. If the following two conditions are met, this discrete energy spectrum will suppress current through the dot, otherwise known as Coulomb blockade.

Firstly, in order to suppress temperature induced tunneling, the energy associated with the Coulombic repulsion of adding an electron to the dot must be larger than the thermal energy of electrons in the leads.[63] This condition can be written as,

$$\frac{e^2}{C_\Sigma} \gg k_B T, \tag{7.1}$$

where e is the electron charge, C_Σ is the total capacitance of the dot to ground, k_B is Boltzmann's constant, and T is the electron temperature in the leads.

Secondly, the number of electrons on the dot must be a well defined integer, implying that the tunnel barriers provide sufficient isolation that the wavefunctions of electrons on the dot do not extend onto the leads. This condition can be restated as requiring device conductance, G, to be much less than the quantum of conductance,[63, 64]

$$G \ll \frac{e^2}{h}, \tag{7.2}$$

where h is Plank's constant.

The total free energy of a dot is the sum of the electrostatic and quantum energies of the electrons residing on the dot. If we consider the many electron regime, the quantum mechanical contribution becomes negligible. Thus, we can write the total

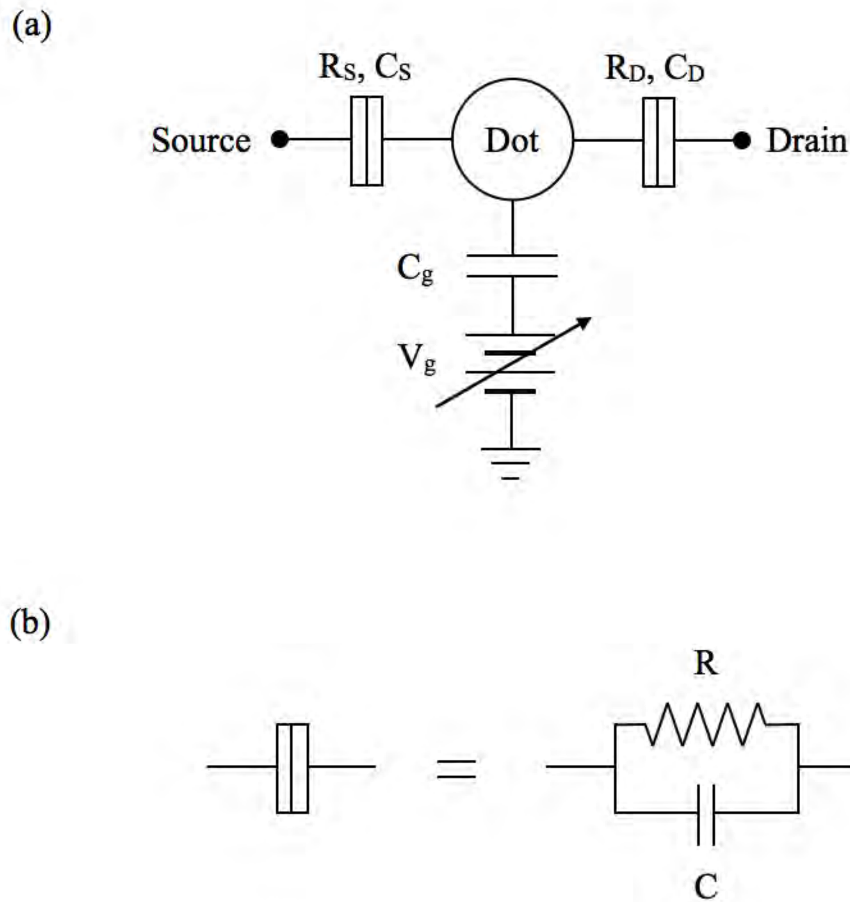

Figure 7.1: (a) Circuit diagram of a quantum dot. The quantum dot is connected to source and drain by tunnel junctions. The dot is capacitively coupled to an electrostatic gate. (b) Tunnel junctions are modeled as a resistor and capacitor in parallel. These junctions allow charge transfer between the dot and leads.

free energy, U, of a dot containing N electrons as the electrostatic contribution,[64, 65]

$$U(N) = \frac{(C_g V_g - Ne)^2}{2C_\Sigma}, \tag{7.3}$$

where C_g is the dot to gate capacitance and V_g is the gate voltage.

The energy of each charge state is parabolic in V_g, the nadir of which occurs when the electrostatically induced charge on the dot is an integer multiple of e. For a given V_g, electrons will tunnel on to or off of the dot until the most energetically favorable N is reached. This electronic configuration is the ground state and a region of charge stability in V_g. As all other charge states are energetically unfavorable, current through the dot is suppressed, forming a Coulomb blockade. The Coulomb blockade is lifted when V_g is adjusted such that two energy states become degenerate, allowing current to flow through the system.

The charging process can also be conceptualized in terms of the electrochemical potential of the dot states. The electrochemical potential of the Nth electron state is,[63]

$$\mu_{dot}(N) \equiv U(N) - U(N-1) = \frac{e^2\,(N-1/2)}{C_\Sigma} - \frac{eC_g V_g}{C_\Sigma}. \tag{7.4}$$

The first term of this equation represents the Coulombic repulsion of the Nth electron to the other $N-1$ electrons on the dot, as well as its self repulsion; the second term represents its capacitive interaction to the electrostatic gate.

The energy required to add a single electron to the quantum dot, known as the charging energy, E_C, is given by the difference between the electrochemical potential of the $N+1$ electron and N electron dot,

$$E_C \equiv \mu_{dot}(N+1) - \mu_{dot}(N) = \frac{e^2}{C_\Sigma}. \tag{7.5}$$

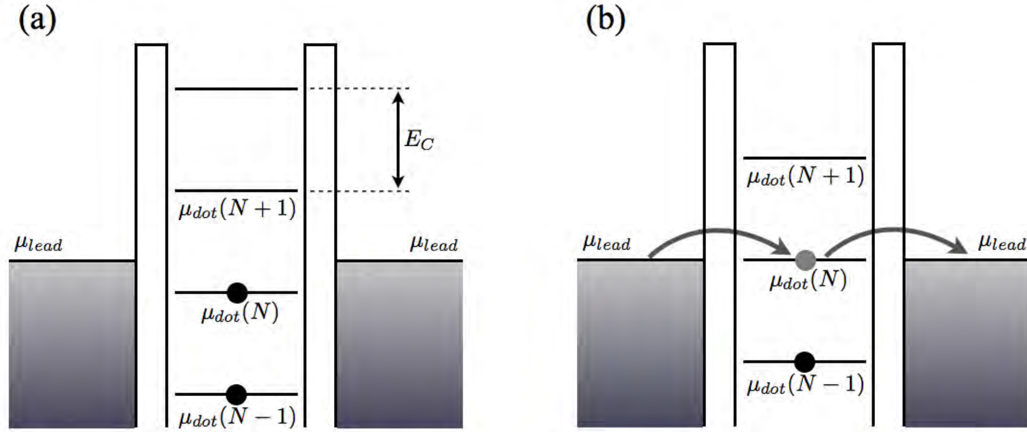

Figure 7.2: Schematic of the dot and lead electrochemical potentials. (a) The states with electrochemical potential less (more) than that of the leads will be occupied (unoccupied). When $\mu_{dot} \neq \mu_{lead}$, Coulomb blockade prevents the movement of electrons through the dot. (b) For $\mu_{dot}(N) = \mu_{lead}$, Coulomb blockade is lifted and electrons can move from source to drain via the N electron state of the dot.

It is this energy that inhibits the tunneling of electrons on to the dot for arbitrary gate voltage configurations, resulting in Coulomb blockade.

For a system in which the source and drain leads are held at the same electrochemical potential, μ_{lead}, we define,

$$\Delta_\mu(N) = \mu_{dot}(N) - \mu_{lead}. \tag{7.6}$$

Electrons will tunnel onto the dot to occupy all dot states in which $\Delta_\mu < 0$. This leads to current suppression as; electrons on the dot have insufficient energy to tunnel into empty states in the lead; electrons in the lead have insufficient energy to tunnel onto dot states for which $\Delta_\mu > 0$. The suppression will be lifted only if an electron pays no energetic cost when tunneling both on to and off of the dot, *i.e.* when $\Delta_\mu = 0$.

The thermal energy of electrons in the leads broadens the conductance of the system around $\Delta_\mu = 0$. Provided the tunnel barriers are opaque enough that finite

lifetime broadening of the dot states is negligible, the conductance varies according to,[65]

$$G = \frac{G_{max}}{[\cosh(\Delta_\mu / 2k_B T)]^2}, \tag{7.7}$$

where G_{max} is the maximum conductance through the device, which is determined by the tunnel junctions characteristics.

Imaging Single Quantum Dots

Coulomb blockade imaging utilized the spatial variation of tip-dot capacitance to tune the difference in lead and dot electrochemical potential. A conducting SPM tip will act as a moveable electrostatic gate, whose capacitive coupling to a dot changes depending on their relative position. By measuring the conductance through a quantum dot system as a function of tip position, this technique can provide information on dot location, electron number, charging energy, and the energy spectrum of the dot. This imaging technique has been used to study quantum dots in 2DEGs,[21] carbon nanotubes,[29], nanowires,[25, 26, 27] and graphene.[33]

7.2.2 Coulomb Blockade in Double Quantum Dots

Electrostatics and Charge Stability

Let us now consider a double quantum dot system in which two series quantum dots connect to source and drain leads. The circuit equivalent for this double dot is shown in Figure 7.3. Dot 1(2) is tunnel coupled to both the source (drain) lead and the other dot. We denote the interdot capacitive coupling as C_{int} and the number of electrons on dot 1(2) as $N_{1(2)}$. Additionally, each dot is capacitively coupled to

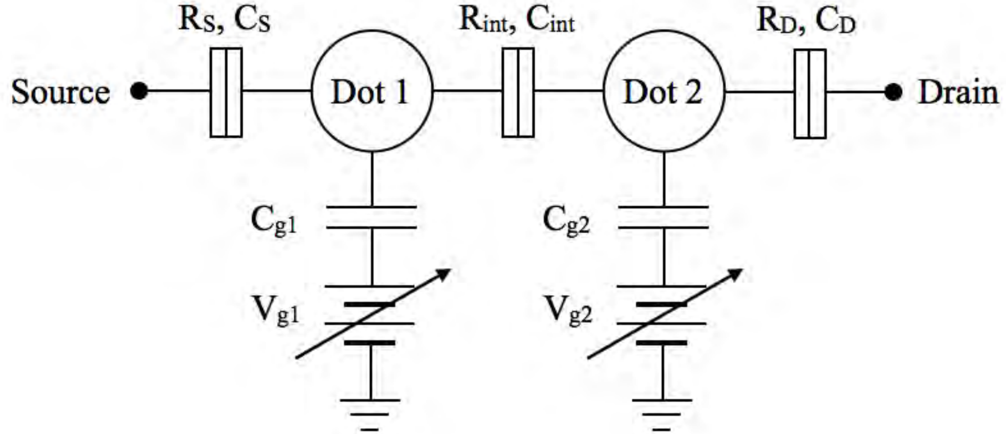

Figure 7.3: Circuit diagram of a double quantum dot. The dots are coupled by a tunnel junction parameterized by a capacitance C_{int}. Each dot is capacitively coupled to its own gate.

a nearby electrostatic gate. For simplicity, we assume that the dots have identical capacitance to ground, C_{Σ}. More rigorous analyses than that which follows can be found in Vidan[64] and van der Wiel *et al.*[66]

The electrostatic energy of a double dot is,[66, 67]

$$U(N_1, N_2) = \frac{1}{2}E_C \left[C_{g1}V_{g1} - N_1 e\right]^2 + \frac{1}{2}E_C \left[C_{g2}V_{g2} - N_2 e\right]^2 \\ + E_{int} \left[C_{g1}V_{g1} - N_1 e\right] \left[C_{g2}V_{g2} - N_2 e\right], \tag{7.8}$$

where E_C is the charging energy of each dot, E_{int} is the interdot coupling energy, $C_{g1(2)}$ is the capacitance between the gate 1(2) and dot 1(2), and $V_{g1(2)}$ is the voltage applied to gate 1(2). The interdot coupling energy, E_{int}, is the energy change of one dot when an electron is added to the other. The energies can be expressed as,

$$E_C = \frac{e^2}{C_{\Sigma}} \left(\frac{1}{1 - \alpha^2} \right), \tag{7.9}$$

$$E_{int} = \frac{e^2}{C_{int}} \left(\frac{1}{\alpha^{-2} - 1} \right), \tag{7.10}$$

where $\alpha \equiv C_{int}/C_{\Sigma}$.

Similar to a single dot, the ground state energy of the double dot is a set of charge stable paraboloids in the V_{g1}-V_{g2} plane. Coulomb blockade prevents current flowing through the system and is only lifted when multiple electron states are degenerate. Figure 7.4 shows charge stability regions for various interdot couplings. When no interdot coupling is present, $C_{int} = 0$, parabaloids for the (N_1, N_2), $(N_1 + 1, N_2)$, $(N_1, N_2 + 1)$, $(N_1 + 1, N_2 + 1)$ states meet at a quadruple point, allowing for a current to move through the double dot system. Intermediate coupling results in the splitting of these quadruple points into two triple points, separated in energy by E_{int}.[66] In the case of strong interdot coupling, the double dots becomes one large dot with total charge $N_1 + N_2$.

The intermediate coupling regime is the most interesting and demands further attention. Charge moves through each triple point via different conduction pathways. The pathway at vertices denoted as ● can be thought of as electron conduction, and is characterized by the evolution of charge states shown in Figure 7.5 and described by,

$$(N_1, N_2) \rightarrow (N_1 + 1, N_2) \rightarrow (N_1, N_2 + 1) \rightarrow (N_1, N_2). \tag{7.11}$$

Conduction through triple points denoted as ○ is mediated by the motion of holes where the evolution of dot states follows,

$$(N_1 + 1, N_2 + 1) \rightarrow (N_1 + 1, N_2) \rightarrow (N_1, N_2 + 1) \rightarrow (N_1 + 1, N_2 + 1). \tag{7.12}$$

The splitting of the triple points can be understood by considering the charge state (N_1, N_2), where the electrochemical potential of each dot is in resonance with those of the source and drain leads. The addition of an electron onto dot 1 from the

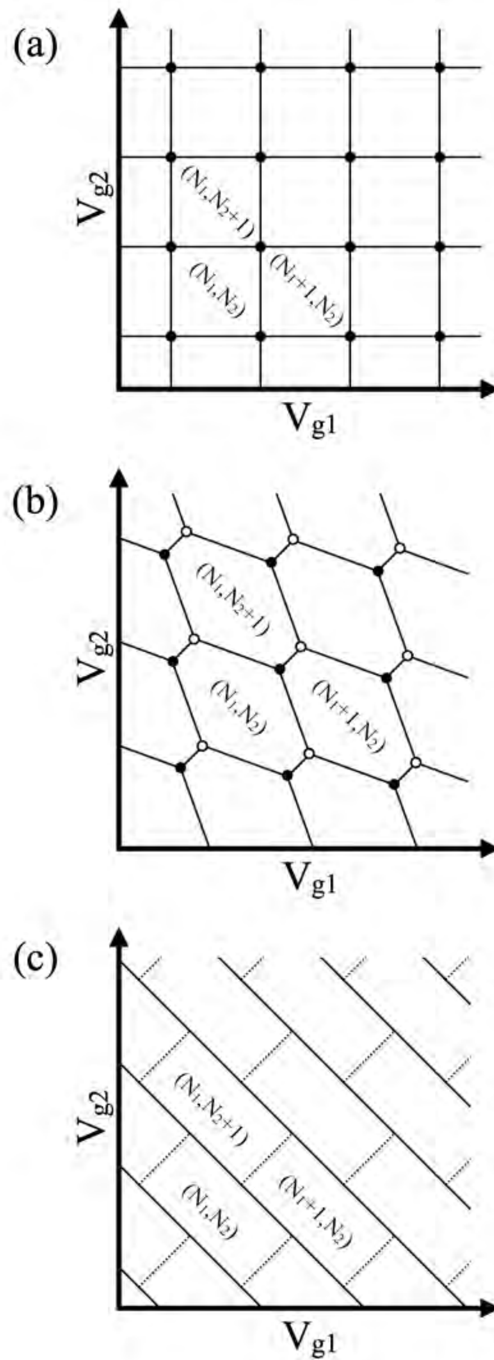

Figure 7.4: Double quantum dot charge stability diagrams showing the boundaries of stable states for (a) weak, (b) intermediate, and (c) strong interdot coupling. For the case of intermediate coupling, the splitting of two triple points indicate distinct conduction pathways corresponding the motion of electrons (●) and holes (○).

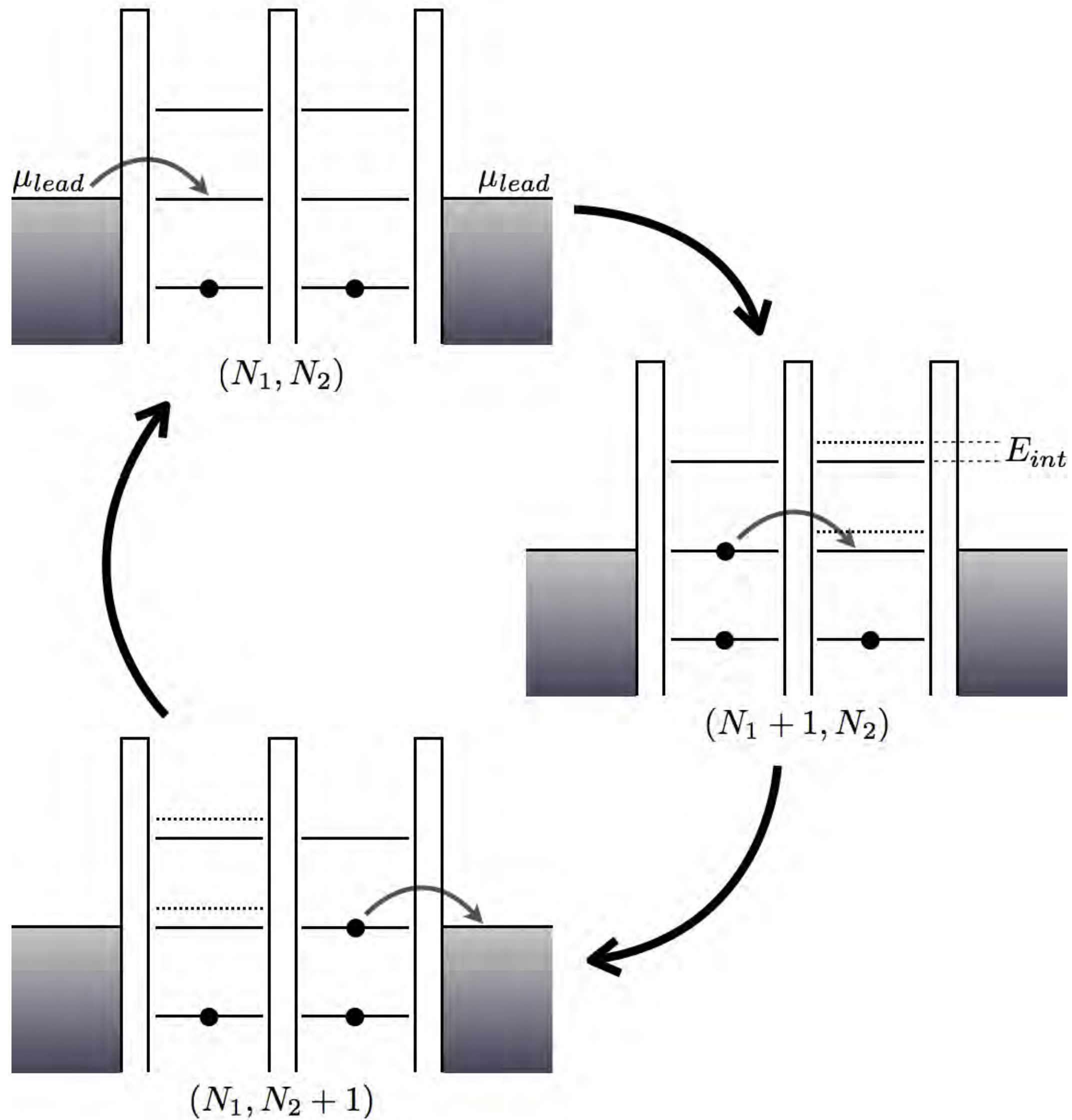

Figure 7.5: Illustration of the electron conduction pathway through a capacitively coupled double quantum dot. If the dot begins in the (N_1, N_2) state, an electron can tunnel from the source onto the left dot. The presence of this electron effectively raises the energy required for electrons to tunnel onto the right dot from the right lead by the interdot coupling energy, E_{int}, prohibiting the tunneling of an additional electron onto the dot. However, the electron on the left dot can tunnel directly to the right dot as this does not change the total dot electron number. Once on the right dot the electron can tunnel into an empty state on the right lead, resulting in a net charge transfer through the dot.

source will move the system to state $(N_1{+}1, N_2)$. This induces a sudden change in the electrostatic potential of dot 2 as seen from the drain, causing the state $(N_1{+}1, N_2{+}1)$ to become energetically inaccessible. However, the transition to (N_1, N_2+1) state is unhindered, allowing conduction through the electron transport triple point to take place. A similar mechanism takes place for the transport of holes through the double dot.[68] It follows that the total interdot capacitively induced energy change from the (N_1, N_2) state to the (N_1+1, N_2+1) state is $2E_{int}$.

Gating with the Tip

Now that we are familiar with the conduction processes in double quantum dots, we turn our attention to gating with a conducting SPM tip. Using an SPM tip as the gate for both dots leads to the circuit equivalent shown in Figure 7.6. If we consider this as the only gate in the system, we can rewrite Equation 7.8 as,

$$\begin{aligned} U(N_1, N_2) = \frac{1}{2} E_C \left[C_{T1} V_T - N_1 e\right]^2 + \frac{1}{2} E_C \left[C_{T2} V_T - N_2 e\right]^2 \\ + E_{int} \left[C_{T1} V_T - N_1 e\right] \left[C_{T2} V_T - N_2 e\right], \end{aligned} \tag{7.13}$$

where $C_{Ti} = C_{Ti}(\mathbf{R})$ is the capacitance between the tip and dot i as a function of tip position, $\mathbf{R}$, and V_T is the voltage applied to the tip.

Conductance of a Double Quantum Dot

The total conductance of the double dot, G_{DD}, is,

$$G_{DD} = G_e + G_h, \tag{7.14}$$

where $G_{e(h)}$ is the conductance of the electron (hole) conduction pathway. Assuming weak interdot tunnel coupling, we naïvely model the conductance through each dot

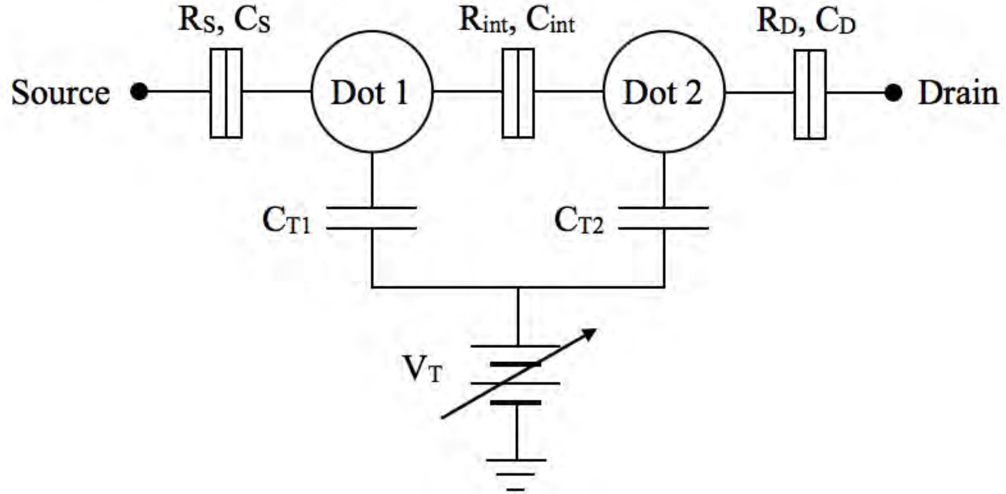

Figure 7.6: Circuit diagram of a double quantum dot gated by a conducting SPM tip. The ability of the tip to tune a double dot comes from the dependence of the tip-dot coupling on tip position.

as independent and following the form,

$$G_{e(h)} = \frac{1}{G_{e(h)1} + G_{e(h)2}}, \tag{7.15}$$

where $G_{e(h)1}$ and $G_{e(h)2}$ are single dot conductances of the electron (hole) mediated conduction pathway of dots 1 and 2 respectively. Each of $G_{e(h)1}$ and $G_{e(h)2}$ follows the form of Equation 7.7.

7.3 Details of Simulation

Simulation of SPM conductance images involves two steps; the first is to calculate the capacitive coupling between the tip and each dot; the second is to use this capacitive coupling to determine the change in electrochemical potential of dot states as a function of tip position that allows the calculation of the system capacitance.

7.3.1 Tip to Dot Capacitance

Two methods are employed to calculate the tip to dot capacitances; the first is to approximate the tip and dots as spheres and calculate the capacitance by analytical methods; the second is to calculate the relevant capacitances using finite difference electrostatic methods. Each method was validated by using it to model a single dot system and observing adequate agreement with experimental results.

Spherical Tip Model

The simplest approximation of the double dot system is to approximate the tip and dots as conducting spheres, and calculate the capacitance between the tip and each dot for various tip positions. The tip is modeled as a 20 nm radius sphere. The radius of the modeled dots is chosen so as to preserve the dot volume. It follows from the capacitance between two spheres[69] that we can write the capacitance between the tip and dot i as,

$$C_{Ti} = 4\pi\epsilon \frac{r_T r_i}{d} \left(1 + \frac{r_T r_i}{d^2 - 2r_T r_i} + \frac{r_T^2 r_i^2}{d^4 - 4d^2 r_T r_i + 3r_T^2 r_i^2} + \cdots \right), \tag{7.16}$$

where r_T is the radius of the tip, r_i is the radius of sphere i, and d is the center-to-center separation of the tip and dot. We use the first three terms in Equation 7.16 to calculate C_{Ti} over the scan range of the tip. Additional terms have negligible influence for scan heights greater than 5 nm.

Electrostatic Simulations

We simulate the capacitances of a double dot nanowire system by finite-element electrostatic simulation (Maxwell 11 - Ansoft Corporation). The model incorporates

a 50 nm diameter InAs nanowire insulated from a conducting substrate by a 100 nm thick silicon oxide layer. Three InP sections in the wire form tunnel barriers that define an InAs double quantum dot within the nanowire. The width of InP tunnel barriers are chosen to be thick enough that the energy associated with tunnel coupling between the dots is much less than E_{int}. The InP widths are typically 5 nm. The tip is modeled as a 500 nm tall cone that converges at 60° to a 20 nm radius sphere. The capacitance between the tip and each dot is calculated for discrete tip positions over a typical SPM scan area. The interdot and total dot to ground capacitances are also calculated, but do not vary with tip position.

7.3.2 Conductance Simulations

In order to calculate conductance through the double dot, we must first approximate the electrochemical potential spectra of each dot. This becomes more complicated when we consider the effect of electron and hole conduction pathways.

We write the electrochemical potential of the Nth state in dot i, contributing to the j conduction pathway as $\mu_{ij}(N)$. We choose the energy separation of electrochemical potentials in each spectrum to be the single dot charging energy, E_C. The hole spectra for each dot are shifted E_{int} higher in energy from the electron spectra to account for the total energy required to overcome the interdot coupling energy. Representative μ_{ie} and μ_{ih} are shown in Figure 7.7.

We next incorporate the change to each state's electrochemical potential due to the capacitive interaction with the tip,

$$\mu_{Tij}(N,\mathbf{R}) = \mu_{ij}(N) + \frac{C_{Ti}(\mathbf{R})V_T^2}{2}, \tag{7.17}$$

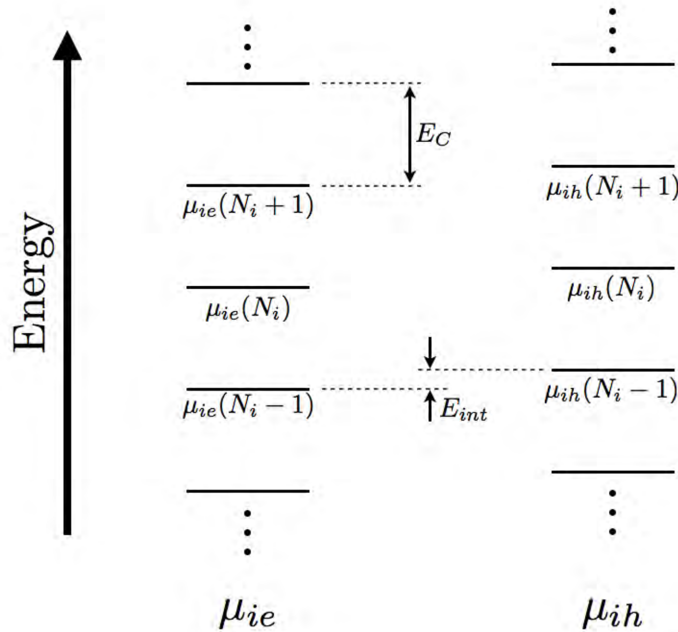

Figure 7.7: Model of the electrochemical potential used in conductance image simulations. Subscript i indicates the dot number, while e and h indicate the conductance pathway to which each spectra contributes. Each dot is assumed to have a continuum of electron states separated by E_C in electrochemical potential. The electrochemical potential of the hole conductance pathway is offset by E_{int} from the electron pathway for each dot.

where V_T is the voltage of the tip.

Δ_μ is calculated for each dot's electron states and used to calculate the conduction through the electron (hole) pathway of each dot as a function of tip position, as per Equation 7.7. The total conductance through the system is calculated following Equations 7.14 and 7.15. All conductances are calculated for lead temperature of 4.2 K and $\mu_{lead} = 0$.

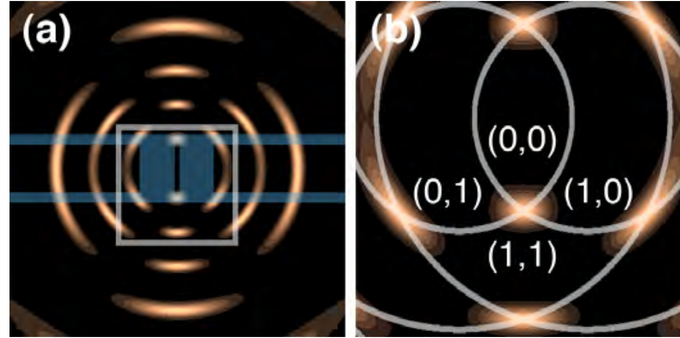

Figure 7.8: SPM conductance image simulation for a double quantum dot formed in a 50 nm diameter InAs/InP nanowire, outlined in blue. Dark (light) regions correspond to low (high) conductance. (a) The quantum dots, shaded in blue, are each 25 nm long and defined by 5 nm InP tunnel barriers. The tip is scanned 50 nm above the nanowire. (b) Zoom in of the boxed area in (a). Regions of charge stability are indicated by overlaid bullseye patterns. Numbers indicate the double dot electron configuration for charge stable regions.

7.4 Results

7.4.1 Charge Stability and Conductance of Uncoupled Dots

Figure 7.8 shows a SPM conductance image simulation for a pair of 25 nm long, non-interacting quantum dots. Ti to dot capacitances are calculated using the spherical tip-dot coupling approximation. Regions of charge stability are easily distinguished in this image, indicating the ability to manipulate the double dot charge state by simply moving the tip.

7.4.2 Charge Stability due to Tip Gating

Figure 7.9 shows the simulated minimum energy surface of a double dot as a function of tip position. Two 35 nm length InAs dots are defined within a 50 nm diameter nanowire. The total capacitance to ground of each dot is 31 aF, implying

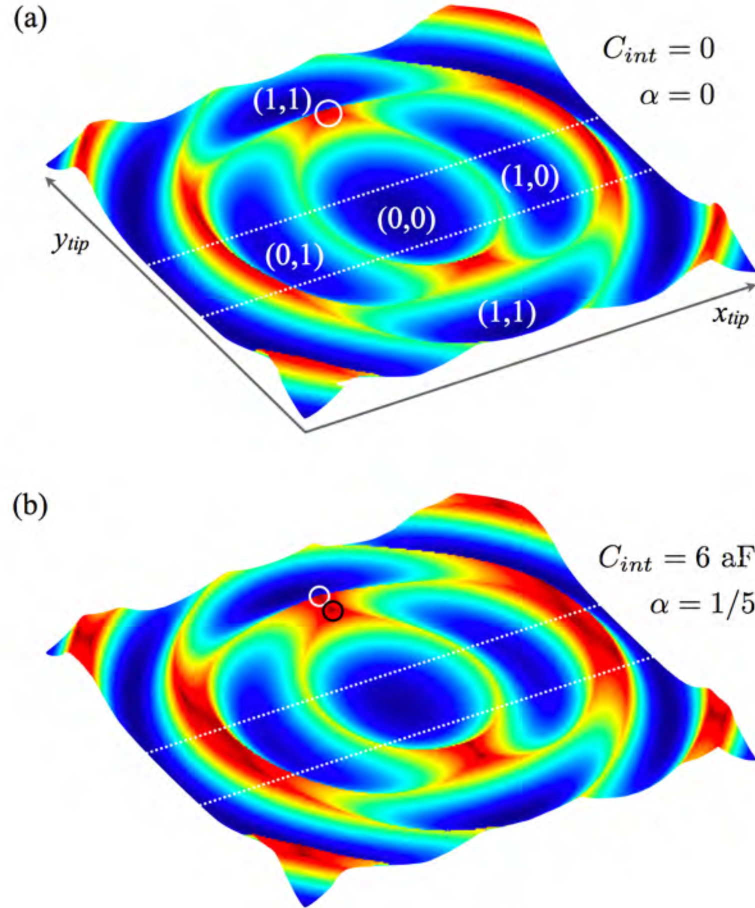

Figure 7.9: Minimum energy surface of as a function of SPM tip position as calculated from the capacitive model. The position of a 50 nm wire InAs nanowire is indicated by the dotted white lines. Two 35 nm quantum dots in the wire are defined by 5 nm InP tunnel barriers. The tip, held at $V_T =$ -100 mV, is scanned in a 250 nm×250 nm plane 20 nm above the top of the nanowire, centered on the interdot InP tunnel barrier. Low energy blue regions correspond to charge stable regions in which the electron number on the double dot is well defined. Points where three or more charge stability regions converge contribute to device conductance. (a) For zero interdot coupling, four charge stability regions meet at a peak in energy denoted by the white circle. Numbers indicate the double dot electron numbers (up to an arbitrary constant) in charge stable regions. (b) For moderate interdot coupling, the quadruple point is seen to split into two triple points, identified by the two open circles. The black (white) circle corresponds to the electron (hole) conduction pathway.

a $E_C \approx 5$ meV, much larger than thermal broadening at 4.2 K. The tip scans a 200 nm$\times$200 nm region and is 20 nm above the top of the nanowire.

Figure 7.9(a) shows the energy surface for uncoupled dots ($C_{int} = 0$). Regions of charge stability are seen in blue. This energy map clearly demonstrates the ability use the position of a SPM tip to manipulate the charge state of a double quantum dot.

As capacitive coupling between the dots is increased, the energy map shows splitting of the quadruple points to triple points. Hence, the tip has the ability to energetically probe the dot states, but it remains to be seen whether this technique has sufficient resolution to see splitting in conductance peaks.

7.4.3 Double Dot Conductance Image Simulations

SPM conductance image simulations for the double dot system described in Section 7.4.2 are shown in Figure 7.10. The dark (light) regions correspond to low (high) conductance. The four panels show the evolution of the conductance image as α is increased from zero to 1/2. As the interdot coupling is increased, conductance through electron and hole mediated conductance paths can be distinguished, indicating the resolution of this imaging technique allows for the measurement of interdot capacitive coupling. For large interdot coupling, the conductance image begins to resemble that of a single quantum dot.

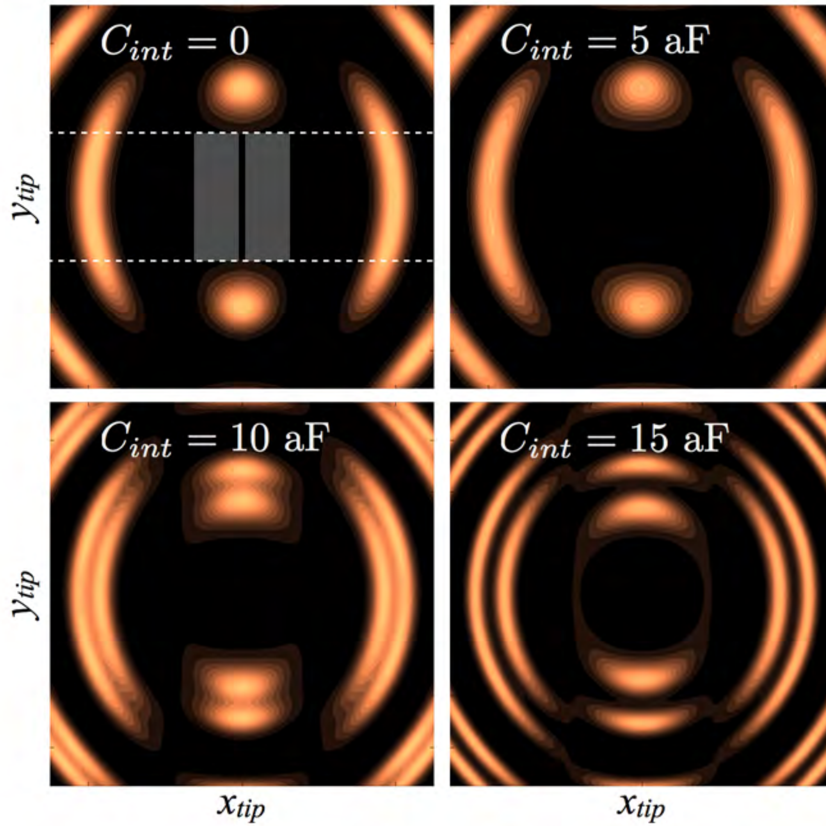

Figure 7.10: SPM conductance simulations for a capacitively coupled double quantum dot. The position of a 50 nm wire InAs nanowire is indicated by the dotted white lines. Two 35 nm quantum dots, indicated by a light area within the wire, are defined by 5 nm InP tunnel barriers and have $C_{\Sigma} = 31$ aF. The tip is scanned in a 250 nm×250 nm plane 20 nm above the top of the nanowire. Light (dark) regions correspond to high (low) conductance. As interdot coupling is increased, regions of high conductance split into two, indicative of quadruple point charge degeneracies splitting into triple points.

7.5 Discussion and Outlook

Conductance image simulations demonstrate the ability to use a SPM tip to tune the electronic state of a double quantum dot at 4.2 K. Regions of charge stability can be extracted from SPM conductance images, as can peak splittings due to interdot coupling. SPM conductance images in these systems are equivalent to traditional dual gate manipulation of double dots. The use of an SPM tip as a gate should allow for the manipulation of charges and spins on nanowire double quantum dots that have been difficult with lithographic techniques due to the size scales of the system. Dot systems consisting of three and four dots could be manipulated with the SPM if the V_T and the z component of the tip position are adjusted simultaneously with x and y position.

Chapter 8

Conclusions

We have designed and built a low temperature scanning probe microscope for the investigation of semiconductor electronic devices by scanning gate microscopy. We have demonstrated the ability of the microscope to scan and capacitively image at room temperature and liquid helium temperature. The SPM design meets the desired specifications set forth in Chapter 1, although the single-stage sub-Kelvin He-3 cooler must still be installed and its performance characterized.

The ability of the SPM to probe the capacitive coupling between tip and sample has been demonstrated by measuring the deflection of the SPM cantilever due to electrostatic forces from a nanometer scale patterned electrode. Forces on the order of 10 nN have been measured with considerable ease in the current experimental implementation. Initial electrostatic force microscopy measurements demonstrate the ability to measure changes in capacitance on the order of 0.1 aF/nm and locate a 200 nm wide charged electrode with precision of approximately 80 nm. Additionally, preliminary experiments show the ability to detect a 30 nm gap between two electrodes

held at the same potential.

Simulations of SGM of semiconductor nanowire double quantum dots indicate the viability of this technique to image conductance through such systems. These simulations indicate that SGM has the ability to manipulate the charge state and polarization of a multiple quantum dot in a nanowire system. Additionally, this technique looks to provide a method to transition between electron states without allowing conduction through the device, a key requirement for controlling electron-electron interactions in these systems.

8.1 Future Directions

Graphene. SGM studies of graphene have elucidated behavior such as universal conductance fluctuations,[30] weak localization,[31] and quantum confinement.[33] Based on increased mobility observed in suspended graphene,[70, 71] Sagar Bhandari has begun work on imaging patterned, suspended graphene using our LT-SPMs in scanning gate mode. Given the progress in terms of sample fabrication, this would be an ideal test of the functionality of the new LT-SPM.

Nanowires. Semiconductor nanowires are a system well suited for SGM investigation. Of particular interest are heterostructured nanowires in which quantum dots can be intentionally formed.[58, 72] SGM could be used to probe and manipulate nanowire quantum dots to study transitions between Luttinger liquid and Wigner crystal phases in ultra-thin nanowires[73] and image the electronic wavefunction.[36]

2DEGs. The first systems to be studied with SGM were GaAs/AlGaAs 2DEGs.[17, 18] Although considerable effort has gone into their investigation, many interesting device structures remain to be investigated. Possible experiments include; detection of spin polarized currents in electron focusing geometries;[74] imaging electron density in 2DEG quantum dots;[75] and the investigation of Zitterbewegung in 2DEG channels.[76, 77]

8.2 Potential LT-SPM Modifications

Three potentially valuable modifications to the LT-SPM are:

- Incorporation of a piezoactuator capable of oscillating the SPM cantilever at its resonant frequency. This would introduce the ability to modulate the tip-sample coupling, and hence system behavior, in the range of 100 kHz.
- Incorporation of coaxial or triaxial scanning probes based on those investigated by Brown *et al.*[78, 79] Coaxial probes modify the electric field due the tip from monopolar to dipolar,[80, 81] affording significant advantages for the investigation of resolution limited systems, such as wave-function mapping in quantum dots.
- The piezocapacitive properties of self-driving cantilevers described by Brown[81] may offer a substitute to the piezoresistive cantilevers currently used in the LT-SPM. The cantilever's embedded capacitor could be used to detect cantilever deflection, a reversal of the intended use. The ability to fabricate such embedded

capacitors in house, on most any commercially available cantilever is certainly an attractive possibility and warrants further investigation.

8.3 Concluding Remarks

Through meeting the desired specifications set forth in the opening chapter, we believe the low temperature scanning probe microscope discussed throughout this thesis offers significant advantages over others in the Westervelt lab. Now that the SPM is operational, the challenge moves to identification, fabrication, and investigation of interesting and novel nanometer scale electronic devices.

Bibliography

[1] Technology Working Group. International technology roadmap for semiconductors 2010 update. Technical report, International Technology Roadmap for Semiconductors, 2010.

[2] Intel Corporation. Introduction to Intel's 32nm process technology [White paper], 2009. Retrieved from http://download.intel.com/pressroom/-kits/32nm/westmere/Intel_32nm_overview.pdf.

[3] D.D. Awschalom, D. Loss, and N. Samaeth. *Semiconductor Spintronics and Quantum Computation*. Springer, 2002.

[4] S.A. Wolf, D.D. Awschalom, R.A. Buhrman, J.M. Daughton, S. vonMolnar, M.L. Roukes, A.Y. Chtchelkanova, and D.M. Treger. Spintronics: A spin-based electronics vision for the future. *Science*, 294(5546), 2001.

[5] C.H. Bennett and D.P. DiVincenzo. Quantum information and computation. *Nature*, 404(6775), 2000.

[6] M.A. Nielsen and I.L. Chuang. *Quantum computation and quantum information*. Cambridge University Press, 2000.

[7] D. Loss and D.P. DiVincenzo. Quantum computation with quantum dots. *Physical Review A*, 57(1), 1998.

[8] C.W.J. Beenakker and H. vanHouten. Quantum Transport in Semiconductor Nanostructures. *Solid State Physics - Advances in Research and Applications*, 44, 1991.

[9] S. Datta. *Electronic Transport in Mesoscopic Systems*. Cambridge University Press, 1995.

[10] L.L. Sohn, L.P. Kouwenhoven, and Schön, editors. *Mesoscopic electron transport*. Kluwer Academic, 1997.

[11] S. De Franceschi, L.V. Kouwenhoven, C. Schoenenberger, and W. Wernsdorfer. Hybrid superconductor-quantum dot devices. *Nature Nanotechnology*, 5(10), 2010.

[12] G. Binnig and H. Rohrer. Scanning Tunneling Microscopy. *Helvetica Physica Acta*, 55(6), 1982.

[13] G. Binnig, H. Rohrer, C. Gerber, and E. Weibel. 7×7 Reconstruction on Si(111) Resolved in Real Space. *Physical Review Letters*, 50(2), 1983.

[14] G. Binnig, C.F. Quate, and C. Gerber. Atomic Force Microscope. *Physical Review Letters*, 56(9), 1986.

[15] E. Meyer, H.J. Hug, and R. Bennewitz. *Scanning probe microscopy: the lab on a tip*. Springer, 2004.

[16] E. Meyer, S.R. Jarvis, and N.D. Spencer. Scanning probe Microscopy in materials science. *MRS Bulletin*, 29(7), 2004.

[17] M.A. Topinka, B.J. LeRoy, S.E.J. Shaw, E.J. Heller, R.M. Westervelt, K.D. Maranowski, and A.C. Gossard. Imaging coherent electron flow from a quantum point contact. *Science*, 289(5488), 2000.

[18] M.A. Topinka, B.J. LeRoy, R.M. Westervelt, S.E.J. Shaw, R. Fleischmann, E.J. Heller, K.D. Maranowski, and A.C. Gossard. Coherent branched flow in a two-dimensional electron gas. *Nature*, 410(6825), 2001.

[19] B.J. LeRoy, M.A. Topinka, R.M. Westervelt, K.D. Maranowski, and A.C. Gossard. Imaging electron density in a two-dimensional electron gas. *Applied Physics Letters*, 80(23), 2002.

[20] B.J. LeRoy, A.C. Bleszynski, K.E. Aidala, R.M. Westervelt, A. Kalben, E.J. Heller, S.E.J. Shaw, K.D. Maranowski, and A.C. Gossard. Imaging electron interferometer. *Physical Review Letters*, 94(12), 2005.

[21] P. Fallahi, A.C. Bleszynski, R.M. Westervelt, J. Huang, J.D. Walls, E.J. Heller, M. Hanson, and A.C. Gossard. Imaging a single-electron quantum dot. *Nano Letters*, 5(2), 2005.

[22] K.E. Aidala, R.E. Parrott, T. Kramer, E.J. Heller, R.M. Westervelt, M.P. Hanson, and A.C. Gossard. Imaging magnetic focusing of coherent electron waves. *Nature Physics*, 3(7), 2007.

[23] M.P. Jura, M.A. Topinka, L. Urban, A. Yazdani, H. Shtrikman, L.N. Pfeiffer, K.W. West, and D. Goldhaber-Gordon. Unexpected features of branched flow through high-mobility two-dimensional electron gases. *Nature Physics*, 3(12), 2007.

[24] A.E. Gildemeister, T. Ihn, R. Schleser, K. Ensslin, D.C. Driscoll, and A.C. Gossard. Imaging a coupled quantum dot-quantum point contact system. *Journal of Applied Physics*, 102(8), 2007.

[25] A.C. Bleszynski-Jayich, F.A. Zwanenburg, R.M. Westervelt, A.L. Roest, E.P.A.M. Bakkers, and L.P. Kouwenhoven. Scanned probe imaging of quantum dots inside InAs nanowires. *Nano Letters*, 7(9), 2007.

[26] A.C. Bleszynski-Jayich, L.E. Froberg, M.T. Bjork, H.J. Trodahl, L. Samuelson, and R.M. Westervelt. Imaging a one-electron InAs quantum dot in an InAs/InP nanowire. *Physical Review B*, 77(24), 2008.

[27] E.E. Boyd, K. Storm, L. Samuelson, and R.M. Westervelt. Scanning gate imaging of quantum dots in 1D ultra-thin InAs/InP nanowires. *Nanotechnology*, 22(18), 2011.

[28] M. Bockrath, W.J. Liang, D. Bozovic, J.H. Hafner, C.M. Lieber, M. Tinkham, and H.K. Park. Resonant electron scattering by defects in single-walled carbon nanotubes. *Science*, 291(5502), 2001.

[29] M.T. Woodside and P.L. McEuen. Scanned probe imaging of single-electron charge states in nanotube quantum dots. *Science*, 296(5570), 2002.

[30] J. Berezovsky, M.F. Borunda, E.J. Heller, and R.M. Westervelt. Imaging coherent transport in graphene (part I): mapping universal conductance fluctuations. *Nanotechnology*, 21(27), 2010.

[31] J. Berezovsky and R.M. Westervelt. Imaging coherent transport in graphene (part II): probing weak localization. *Nanotechnology*, 21(27), 2010.

[32] M.R. Connolly, K.L. Chiou, C.G. Smith, D. Anderson, G.A.C. Jones, A. Lombardo, A. Fasoli, and A.C. Ferrari. Scanning gate microscopy of current-annealed single layer graphene. *Applied Physics Letters*, 96(11), 2010.

[33] S. Schnez, J. Guettinger, M. Huefner, C. Stampfer, K. Ensslin, and T. Ihn. Imaging localized states in graphene nanostructures. *Physical Review B*, 82(16), 2010.

[34] K.E. Aidala. *Imaging Magnetic Focusing in a Two-Dimensional Electron Gas*. PhD thesis, Harvard University, 2006.

[35] M.A. Topinka. *Imaging Coherent Electron Wave Flow Through 2-D Electron Gas Nanostructures*. PhD thesis, Harvard University, 2002.

[36] E.E. Boyd. *Imaging Electrons in Ultra-thin Nanowires*. PhD thesis, Harvard University, 2011.

[37] B.J. LeRoy. *Imaging Coherent Flow Through Semiconductor Nanostructures*. PhD thesis, Harvard University, 2003.

[38] J.W. Ekin. *Experimental Techniques for Low-Temperature Measurements*. Oxford University Press, 2006.

[39] R.C. Richardson and E.S. Smith, editors. *Experimental Techniques in Condensed Matter Physics at Low Temperatures*. Addison-Wesley, 1988.

[40] G.K. White. *Experimental Techniques in Low Temperature Physics*. Oxford University Press, 1959.

[41] F. Pobell. *Matter and Methods at Low Temperatures*. Springer, 1992.

[42] B.A. Hands, editor. *Cryogenic Engineering*. Academic Press, 1986.

[43] A.L. Woodcraft. An introduction to cryogenics [White paper], 2007. Retrieved from http://uk.lowtemp.org/1-Woodcraft.pdf.

[44] A.L. Woodcraft and A. Gray. A low temperature thermal conductivity database. In A. Miller B. Cabrera and B. Young, editors, *Low Temperature Detectors LTD 13, Proceedings of the 13th International Workshop*. American Institute of Physics, 2009.

[45] A.J. Rimberg. *Magnetotransport in Uniform and Modulated Electron Gases in Wide Parabolic Quantum Wells*. PhD thesis, Harvard University, 1992.

[46] C.A. Bailey and B.A. Hands. Thermal design. In B.A. Hands, editor, *Cryogenic Engineering*, pages 89–121. Academic Press, 1986.

[47] G.K. White. *Experimental Techniques in Low Temperature Physics*, pages 178–202. Oxford University Press, 1959.

[48] E.D. Marquardt, J.P. Le, and R. Radebaugh. Cryogenic material properties database. In R.G. Ross, editor, *Cryocoolers 11: the Proceedings of the International Cryocooler Conference*. Kluwer Academic/Plenum Publishers, 2001.

[49] J.G. Hust. Thermal conductivity and thermal diffusivity. In R.P. Reed and A.F. Clark, editors, *Materials at Low Temperature*, pages 133–161. American Society for Matels, 1983.

[50] E.N. Smith, J.E. vanCleve, R. Movshovich, R.S. Germain, and E.T. Swartz. Cryogenic design aids. In R.C. Richardson and E.S. Smith, editors, *Experimental Techniques in Condensed Matter Physics at Low Temperatures*, pages 97–165. Addison-Wesley, 1988.

[51] R.W. Powell, C.Y. Ho, and P.E. Liley. Thermal conductivity of selected materials. Technical report, National Bureau of Standards, 1966.

[52] D.R. Lide, editor. *CRC Handbook of Chemistry and Physics*, pages 12–205. CRC Press, 89th edition, 2008.

[53] P. Girard. Electrostatic force microscopy: principles and some applications to semiconductors. *Nanotechnology*, 12(4), 2001.

[54] S. Belaidi, F. Lebon, P. Girard, G. Leveque, and S. Pagano. Finite element simulations of the resolution in electrostatic force microscopy. *Applied Physics A - Materials Science & Processing*, 66(Part 1, S):S239–S243, 1998.

[55] S. Belaidi, P. Girard, and G. Leveque. Electrostatic forces acting on the tip in atomic force microscopy: Modelization and comparison with analytic expressions. *Journal of Applied Physics*, 81(3), 1997.

[56] C.M. Lieber. Nanoscale science and technology: Building a big future from small things. *MRS Bulletin*, 28(7), 2003.

[57] P.D. Yang. The chemistry and physics of semiconductor nanowires. *MRS Bulletin*, 30(2), 2005.

[58] L. Samuelson, C. Thelander, M.T. Bjork, M. Borgstrom, K. Deppert, K.A. Dick, A.E. Hansen, T. Martensson, N. Panev, A.I. Persson, W. Seifert, N. Skold, M.W. Larsson, and L.R. Wallenberg. Semiconductor nanowires for 0D and 1D physics and applications. *Physica E - Low-Dimensional Systems & Nanostructures*, 25(2-3), 2004.

[59] M.T. Bjork, A. Fuhrer, A.E. Hansen, M.W. Larsson, L.E. Froberg, and L. Samuelson. Tunable effective g factor in InAs nanowire quantum dots. *Physical Review B*, 72(20), 2005.

[60] L.O. Olsson, C.B.M. Andersson, M.C. Hakansson, J. Kanski, L. Ilver, and U.O. Karlsson. Charge accumulation at InAs surfaces. *Physical Review Letters*, 76(19), 1996.

[61] M.T. Bjork, B.J. Ohlsson, T. Sass, A.I. Persson, C. Thelander, M.H. Magnusson, K. Deppert, L.R. Wallenberg, and L. Samuelson. One-dimensional steeplechase for electrons realized. *Nano Letters*, 2(2), 2002.

[62] M.T. Bjork, C. Thelander, A.E. Hansen, L.E. Jensen, M.W. Larsson, L.R. Wallenberg, and L. Samuelson. Few-electron quantum dots in nanowires. *Nano Letters*, 4(9), 2004.

[63] L.P. Kouwenhoven, N.C. van der Vaart, A.T. Johnson, W. Kool, C.J.P.M. Harmans, J.G. Williamson, A.A.M. Staring, and C.T. Foxon. Single electron charging effects in semiconductor quantum dots. *Zeitschrift fur Physik B - Condensed Matter*, 85(3), 1991.

[64] A. Vidan. *Charge and Spin Effects in Semiconductor Nanostructures*. PhD thesis, Harvard University, 2006.

[65] C.W.J. Beenakker. Theory of Coulomb-blockade oscillations in the conductance of a quantum dot. *Physical Review B*, 44(4), 1991.

[66] W.G. van der Wiel, S. De Franceschi, J.M. Elzerman, T. Fujisawa, S. Tarucha, and L.P. Kouwenhoven. Electron transport through double quantum dots. *Reviews of Modern Physics*, 75(1), 2003.

[67] C. Livermore, C.H. Crouch, R.M. Westervelt, K.L. Campman, and A.C. Gossard. The Coulomb blockade in coupled quantum dots. *Science*, 274(5291), 1996.

[68] R.H. Blick, R.J. Haug, J. Weis, D. Pfannkuche, K. vonKlitzing, and K. Eberl. Single-electron tunneling through a double quantum dot: The artificial molecule. *Physical Review B*, 53(12), 1996.

[69] C. Wasshuber. *Computational Single-Electronics*. Springer, 2001.

[70] K.I. Bolotin, K.J. Sikes, Z. Jiang, M. Klima, G. Fudenberg, J. Hone, P. Kim, and H.L. Stormer. Ultrahigh electron mobility in suspended graphene. *Solid State Communications*, 146(9-10), 2008.

[71] X. Du, I. Skachko, A. Barker, and E.Y. Andrei. Approaching ballistic transport in suspended graphene. *Nature Nanotechnology*, 3(8), 2008.

[72] C. Yang, Z.H. Zhong, and C.M. Lieber. Encoding electronic properties by synthesis of axial modulation-doped silicon nanowires. *Science*, 310(5752), 2005.

[73] J. Qian, B.I. Halperin, and E.J. Heller. Imaging and manipulating electrons in a one-dimensional quantum dot with coulomb blockade microscopy. *Physical Review B*, 81(12), Mar 2010.

[74] A. Reynoso, G. Usaj, and C.A. Balseiro. Detection of spin polarized currents in quantum point contacts via transverse electron focusing. *Physical Review B*, 75(8), 2007.

[75] P. Fallahi. *Imaging Electrons in Few-Electron Quantum Dots*. PhD thesis, Harvard University, 2006.

[76] J. Schliemann, D. Loss, and R.M. Westervelt. Zitterbewegung of electronic wave packets in III-V zinc-blende semiconductor quantum wells. *Physical Review Letters*, 94(20), 2005.

[77] U. Zuelicke, J. Bolte, and R. Winkler. Magnetic focusing of charge carriers from spin-split bands: semiclassics of a Zitterbewegung effect. *New Journal of Physics*, 9, 2007.

[78] K.A. Brown, J.A. Aguilar, and R.M. Westervelt. Coaxial atomic force microscope tweezers. *Applied Physics Letters*, 96(12), 2010.

[79] K.A. Brown and R.M. Westervelt. Proposed triaxial atomic force microscope contact-free tweezers for nanoassembly. *Nanotechnology*, 20(38), 2009.

[80] K.A. Brown, J. Berezovsky, and R.M. Westervelt. Coaxial atomic force microscope probes for imaging with dielectrophoresis. *Applied Physics Letters*, 98(18), 2011.

[81] K.A. Brown. *Imaging and Manipulation of Nanoscale Materials with Coaxial and Triaxial AFM Probes*. PhD thesis, Harvard University, 2011.

Appendix A

Sample Chip Carrier Fabrication

This appendix is to serve as a manual for the fabrication of sample chip carriers as briefly discussed in Chapter 2.

1. Secure a 4” by 4” sample chip carrier PCB to a mounting plate in preparation for milling. If a mounting plate cannot be found, one can be made by drilling and tapping holes in a 3.5” square aluminum or brass block.

2. Use the jeweler’s mill to drill two 0-80 through holes in a sample chip carrier. Orient these holes as shown in Figure 2.2. The center-to-center distance of these two holes should be 0.38”.

3. Use an end mill to remove approximately 0.03” (0.8 mm) in depth from the area between the bond pads of a sample chip carrier. Reduce the dust from the milling procedure by using plenty of machine oil.

4. Use an end mill to cut the sample chip carrier from the larger PCB. Take multiple passes, each approximately 0.01” in depth, to reduce the chances of damaging the chip carrier during milling. Reduce the dust from the milling procedure by using plenty of machine oil.

5. When the chip carrier is free, sand the edges and attach to the assembled microscope. Check the clearance from the xy coarse positioning feedthroughs and the z coarse approach screw to the chip carrier. Detach the chip carrier from microscope and remove material as necessary for clearance of 0.02” (0.5 mm).

6. Carefully strip 2 mm of insulation off the end of PVC insulated AWG 32 copper wire for sample leads. Insert these through the rear of the holes in the bond pads of the chip carrier so that the insulation meets the sample chip carrier. Trim the leads protruding from the top of the carrier to 1 mm.

7. Solder sample leads to bond pads. Begin by applying a small amount of flux to lead and pad. With a soldering iron set to 800°F or higher, burn off excess flux. Melt a very small amount of solder to the iron tip; touch the molten solder to the lead and pad. Once solidified, test the lead is held solidly to ensure good electrical contact. Remove residual flux with flux remover.

8. Sand off excess solder until the copper of each bond pad is visible. This provides a surface well suited for wirebonding.

9. Gold plate the sample chip carrier bond pads Bright Electroless Gold manufactured by Transene Company of Danvers, MA, is exceedingly easy to use and has produced excellent results.

10. Trim the sample leads to the same length and carefully remove 2-3 mm of insulation. Solder these to a Microtech connector for electrical connection of the sample to cryostat leads. Shrink wrap each lead to ensure electrical isolation, and wrap the Microtech connector with low temperature vacuum tape for mechanical stability. Acrylic adhesive backed Kapton tape works well.

11. Apply GE varnish to any bare sample leads exiting the rear of the sample chip carrier to avoid unwanted electrical shorts.

Appendix B

Head Assembly and Room Temperature Alignment Procedure

This appendix is to serve as a manual for the installation of a sample and alignment of the tip. The process begins assuming the piezotube and cage are assembled, and that a sample of interest has been fabricated and awaits installation. Be sure to keep yourself and the sample grounded throughout this process in order to reduce the risk of shocking the device through static discharge.

1. Attach sample to the PCB sample chip carrier.

    a. If the sample has a backgate, attach a small piece of aluminum foil to the center of the sample chip carrier with silver paint. The size of this foil should be larger than the sample, but small enough to lie flat in the area between the bond pads of the sample chip carrier. Press the foil flat with tweezers or a wooden applicator as the silver paint sets.

    b. Attach the sample to the chip carrier with a small dab of silver paint. Press down on the sample edges with wooden applicator sticks to ensure it is flat against the carrier's surface.

    c. Wirebond the sample to the chip carrier bond pads. Wirebond powers between 200 and 350 mW and sonication times of 15 ms on the CNS Westbond wirebonder are usually sufficient. Excessive power can punch through the insulating layer of a sample, shorting the bond pad to the backgate.

2. Attach the sample chip carrier to the piezotube chip carrier plate.

    a. Insert two 0-80 screws in the aligned sample chip carrier and piezotube grounding plate.

b. Carefully secure the chip carrier to the piezotube taking care to not over-tighten the screws. Be as gentle as possible to avoid stressing the piezotube during attachment.

c. Adjust the position of sample leads so that they do not touch the ball end screws or xy feedthroughs that protrude from the cage.

3. Install the microscope head.

a. Ensure the three ball end screws are sufficiently far out of the cage so that the tip is not in danger of touching the sample.

b. Carefully place the head atop the ball end screws such that the tip faces forward towards the z coarse adjust screw. Begin by placing the grooves in the base of the head on the two screws toward the rear of the cage, then slowly lower the front of the head so that it comes into contact with the z coarse approach screw. Make sure all ball end screws are securely held in the grooves in the base of the head.

c. While holding the head on the ball end screws, attach the springs between the cage and head. A pair of strong, sharp tweezers is particularly helpful for this task.

4. Perform room temperature coarse alignment of the tip and sample in x, y, and z.

a. Adjust the three ball end screws to bring the tip to within 2 to 3 turns of the z coarse approach screw to the surface.

b. Use a long working distance binocular microscope to view the position of the sample and tip through the center of the head. Roughly align the tip to the sample in x and y. Excellent precision can be achieved by using a 1" 0-80 screw inserted into the cantilever chip carrier slider as a lever. Loosen (tighten) the cantilever carrier clamp before (after) alignment. Be sure to hold the head tightly during adjustment.

c. Lie the microscope in a cradle and use the binocular microscope to view the cantilever approach the sample from the side. Bring the cantilever one turn away from the sample surface.

d. Viewing down the axis of the microscope again, use the slider and xy coarse positioning mechanisms to move the cantilever as close to the desired location on the sample as possible. Alignment to within 5 μm is relatively easy. Hold the head tightly during adjustment.

5. Prepare microscope for insertion.

a. Place the microscope upside down in the microscope assembly stand.

b. Use dental floss to tie all sample and cantilever leads in place. Be sure to allow some slack in the top end of the sample leads to allow free movement of the piezotube.

Appendix C

Microscope Installation and Cryostat Evacuation

This appendix is to serve as a manual for the installation of the microscope into the cryostat for standard sample exchange.

C.1 Mircoscope Insertion

1. With the assembled microscope held upside down in the assembly stand, insert the z vertical feedthrough rod, collar, and attached feedthrough plate into the cage base and cage. Adjust the collar such that the feedthrough can drive the z coarse approach ball end screw. Note that the driver should not be inserted all the way into the screw as this inhibits the tip from approaching the sample. Remove the z feedthrough rod and feedthrough plate.

2. Insert the vertical xy feedthrough rods into the cage base and cage. Clamp the feedthrough collars onto the rods such that the xy drivers reach their respective screws. A gap of approximately 0.5 mm between xy drivers and their screws is sufficient to allow the tip to approach sample unimpeded if the tip is within two turns of the z coarse approach screw of the surface.

3. Reinstall the z feedthrough and feedthrough plate; secure in place with two 4-40 brass screws. Install the two mitre gears on the xy feedthrough rods such that they are almost flush against the feedthrough plate. Leave a gap small enough that the feedthroughs easily rotate. Remove the feedthrough plate and rods from the microscope.

4. Insert assembled microscope through the coldplate bores and clamp the microscope to the He-3 coldplate with three 4-40 brass screws.

5. Install the vertical feedthrough rods and feedthrough plate. Clamp into place with two 4-40 brass screws.

6. Connect the sample, cantilever, and piezotube driving leads.

7. Install the xy horizontal He-3 feedthrough rods and clamp them into place using phosphor bronze clamps on the He-3 stands.

8. Install the z horizontal He-3 feedthrough rod. Clamp into place.

9. Install the worm gear on the z vertical feedthrough rod.

10. Test xy and z feedthroughs are driving the vertical feedthrough rods as expected.

C.2 Top Hat Installation

1. Place the helium cooled top hat on top of the helium cooled collar. Make sure that the M markings on the top hat and collar are aligned.

2. Clamp the top hat to the collar using sixteen 8-32 stainless steel screws. The order of tightening does not matter.

3. Place the nitrogen cooled top hat on top of the nitrogen cooled collar. Make sure that the two M markings are aligned.

4. Clamp the top hat to the collar using sixteen 8-32 stainless steel screws. The order of tightening does not matter.

5. Clean the Viton O-ring, and the faces of the room temperature collar and top hat between which the O-ring is compressed. Be sure to remove all particles that could compromise the vacuum seal.

6. Apply vacuum grease to the O-ring and install it in the groove in the collar.

7. Carefully place the room temperature top hat on top of the room temperature collar. Make sure that the M markings on the top hat and collar are aligned.

8. Clamp the top hat and collar together with sixteen $\frac{1}{4}$"-20 bolts. Begin by screwing each finger tight, then tighten in the order marked on the cryostat to ensure a good vacuum seal. Tighten each bolt between a quarter and a half of a turn; repeat in order until sufficiently tight (approximately three times).

C.3 Sample Space Evacuation

1. Attach a large roughing pump, via a concrete vibration isolator, to a vacuum valve on the room temperature collar.

2. Turn on the roughing pump, evacuate the vacuum lines to the cryostat, and slowly open the valve into the cryostat vacuum space. Once fully open, continue pumping until the pressure reaches approximately 2×10^{-1} mbar. This usually takes between 15 and 30 minutes.

3. Without venting the sample and vacuum space, disconnect the roughing pump and connect in its place the Pfeiffer turbomolecular pump (turbocube). Pump the vacuum space with the turbocube overnight or until the pressure reaches 10^{-3} mbar.

4. Close the valves to the vacuum space and turbocube. Stop the turbocube, taking care not to power down the unit until it has come to a complete stop and has automatically vented itself to atmospheric pressure.

Appendix D

Cooling Procedures

This appendix is to serve as a manual for cooling the LT-SPM. The procedure outlined below assumes the cryostat has been evacuated by the procedure in Appendix C.

D.1 Nitrogen Pre-Cool

Prior to cooling to liquid helium temperature, the cryostat is pre-cooled to liquid nitrogen temperature. The large latent heat of vaporization and relative inexpensiveness of liquid nitrogen means that it is significantly advantageous over liquid helium for the thermal transition from room temperature to 77 K.

1. Move the tip off the sample surface by 100 turns of the external z coarse approach screw.
2. Use a roughing pump to evacuate the helium reservoir space to approximately 5×10^{-1} mbar to remove water condensed to the chamber walls.
3. Flush the helium space with nitrogen gas, taking care not to expose the space to the atmosphere. To do this, ensure the overpressure valve to the helium space is open, then apply a positive pressure of nitrogen to the space until the overpressure valve releases. Stop the nitrogen flow when this happens.
4. Repeat steps 1 and 2 two additional times. On the final flush, allow nitrogen gas to continue to flow out of the overpressure valve.
5. With the overpressure of nitrogen, open the fill port on the magnet support, insert a nitrogen transfer stick and begin to transfer liquid nitrogen into the space from a Lab50 or similar storage dewar. Insert the transfer stick into the helium space until it touches the backside of the He-4 coldplate, then pull it up approximately 1 mm so that liquid nitrogen can flow freely into the reservoir space.

6. As the transfer begins, halt the overpressure of nitrogen gas and remove the overpressure valve at the KF25 flange. Cold nitrogen gas should flow out of this port from the evaporation of liquid nitrogen as it cools the coldplate and helium space. Monitor the diagnostic resistors as the space fills with liquid nitrogen. Control the rate of transfer by applying additional pressure of nitrogen gas to the storage dewar.

7. Stop the transfer when the 15 liter helium reservoir is full, *i.e.* when the middle diagnostic resistor reaches liquid nitrogen temperature. This usually takes between 30 and 45 minutes and uses approximately 35 liters of liquid nitrogen. When the transfer is complete, do not remove the transfer stick, but instead crimp close the transfer tube so that water vapor cannot enter the helium space. Reinstall the overpressure valve onto the helium space and ensure it is open.

8. Fill the nitrogen reservoir with liquid nitrogen. This space does not need to be flushed.

9. Leave the cryostat to cool for at least 6 hours, preferably overnight.

D.2 Liquid Helium-4 Cooling

After the cryostat has equilibrated at liquid nitrogen temperature, the liquid nitrogen contained in the helium reservoir space is replaced with liquid helium to cool the cryostat down to 4.2 K. The following outlines the procedure for this cooling step.

1. Uncrimp the liquid nitrogen transfer line inserted into the helium reservoir space. The internal pressure of this space will be slightly higher than atmospheric, hence liquid nitrogen will be forced out of the reservoir and through the nitrogen transfer stick. Ensure the exiting liquid nitrogen is funneled into a liquid nitrogen storage vessel.

2. Close the helium reservoir overpressure valve and apply an overpressure of gaseous helium to the helium reservoir space to force liquid nitrogen out through the nitrogen transfer stick.

3. When all the liquid nitrogen has been removed, reduce the gaseous helium pressure and remove the liquid nitrogen transfer stick. Leave the liquid cryogen transfer port open, but make sure a slight overpressure of helium gas is exiting this port.

4. Using a vacuum insulated helium transfer line, begin to transfer of liquid helium out of a liquid helium storage dewar. Do not insert the transfer line into the cryostat until liquid helium begins exiting the transfer line.

5. Upon insertion of the transfer line into the cryostat, remove the helium reservoir space overpressure valve to allow cold helium gas to exit the helium space.

6. Monitor the diagnostic resistors and the liquid helium level meter. Increase the rate of transfer by applying additional pressure of helium gas to the helium storage dewar. Reduce the transfer rate by venting the storage dewar.

7. When the level meter reaches 100%, stop the transfer by venting the storage dewar and removing the helium transfer stick, first from the cryostat, then from the storage dewar. Total transfer time is typically 45 minutes and uses 35 liters of liquid helium.

8. Immediately replace the liquid transfer port plug. When defrosted, replace the overpressure valve.

9. Continue to monitor the liquid helium level meter, diagnostic resistors, and sample vacuum space pressure to ensure the cryostat is cooling as expected.

D.3 Liquid Helium-4 Refilling

The procedure to refill liquid helium is as follows:

1. Open the helium space liquid cryogen transfer port. An overpressure of helium gas due to boil off ensures water vapor does not enter the space.

2. Begin transfer of liquid helium from a storage dewar through a vacuum insulated transfer line. Do not insert the transfer line into the helium space until liquid helium begins to exit the transfer line.

3. Upon insertion of the transfer tube into the helium space, remove the helium reservoir overpressure valve. Increase the rate of transfer by applying additional pressure of helium gas to the helium storage dewar. Reduce the transfer rate by venting the storage dewar.

4. Stop the transfer when the helium level meter reaches 100 percent. Vent the storage dewar and remove the transfer line from the cryostat.

5. Immediately close the transfer port on the cryostat. Reattach the overpressure valve when its KF25 flange defrosts.